Inverse modelling of New Zealand's carbon dioxide balance estimates a larger than expected carbon sink

Beata Bukosa[1], Sara Mikaloff-Fletcher[1], Gordon Brailsford[1], Dan Smale[2], Elizabeth D. Keller[3,4], W. Troy Baisden[5], Miko U.F. Kirschbaum[6], Donna L. Giltrap[6], Lìyǐn Liáng[6], Stuart Moore[1], Rowena Moss[1], Sylvia Nichol[1], Jocelyn Turnbull[3], Alex Geddes[2], Daemon Kennett[1], Dóóra Hidy[7], Zoltán Barcza[8], Louis A. Schipper[9], Aaron M. Wall[9], Shin-Ichiro Nakaoka[10], Hitoshi Mukai[10], Andrea Brandon[11]

[1]National Institute of Water and Atmospheric Research, Wellington, New Zealand
[2]National Institute of Water and Atmospheric Research, Lauder, New Zealand
[3]GNS Science, National Isotope Centre, Lower Hutt, New Zealand
[4]Antarctic Research Centre, Victoria University of Wellington, Wellington, New Zealand
[5]Te Pūnaha Matatini Centre of Research Excellence and Motu Research, Wellington, New Zealand
[6]Manaaki Whenua - Landcare Research, Palmerston North, New Zealand
[7]Excellence Center, Faculty of Science, ELTE Eötvös Loránd University, Martonvásár, Hungary
[8]Department of Meteorology, ELTE Eötvös Loránd University, Budapest, Hungary
[9]School of Science and Environmental Research Institute, University of Waikato, Private Bag 3105, Hamilton, 3240, New Zealand
[10]National Institute for Environmental Studies, Tsukuba, Ibaraki, Japan
[11]New Zealand Ministry for the Environment, Wellington, New Zealand

Correspondence to: Beata Bukosa (Beata.Bukosa@niwa.co.nz)

Abstract. Accurate national scale greenhouse gas source and sink estimates are essential to track climate mitigation efforts. Inverse models can complement inventory-based approaches for emissions reporting by providing independent estimates underpinned by atmospheric measurements, yet few nations have developed this capability for carbon dioxide (CO_2). We present results from a decade-long (2011-2020) national inverse modelling study for New Zealand, which suggests a persistent carbon sink in New Zealand's terrestrial biosphere (-171 ± 29 Tg CO_2 yr^{-1}). This sink is larger than expected from either New Zealand's Greenhouse Gas Inventory (-24 Tg CO_2 yr^{-1}) or prior terrestrial biosphere model estimates (-118 ± 22 Tg CO_2 yr^{-1}, Biome-BGCMuSo and CenW). The largest differences are in New Zealand's South Island, in regions dominated by mature indigenous forests, generally considered to be near equilibrium, and certain grazed pasture regions.

Relative to prior estimates, the inversion points to a reduced net CO_2 flux to the atmosphere during the autumn/winter period. The overall findings of this study are robust with respect to extensive tests to assess the potential biases in the inverse model due to transport error, prior biosphere, ocean and fossil-fuel estimates, background CO_2 and diurnal cycles. We have identified CO_2 exchange processes that could contribute to the gap between the inverse, prior and inventory estimates, but the magnitude of the fluxes from these processes cannot entirely explain the differences. Further work to identify the cause for the gap is essential to understand the implications of this finding for New Zealand's inventory and climate mitigation strategies.

1 Introduction

Under the Paris Agreement, each nation is required to set, track and report progress against a nationally determined contribution towards meeting the goals of the agreement. Where nations set emissions related targets, they must follow agreed reporting guidelines (UNFCCC, 2018) and adhere to inventory methodologies set out by the Intergovernmental Panel on Climate Change (IPCC) (IPCC, 2006, 2019). Current greenhouse gas emissions reduction strategies rely on tracking greenhouse gas emissions and carbon uptake from local to global scal~~MOL~~es, with a special focus on national scale actions to limit emissions and, in doing so, limit increases in global average temperatures (UNFCCC, 2015). National greenhouse gas inventory reporting is typically based on bottom-up nationally representative data collection methods. The most recent IPCC guidelines refinement (IPCC, 2019) recommends using independent methods, such as atmospheric inverse models (i.e., top-down methods) as a complementary tool to estimate national scale carbon fluxes. Top-down methods rely on atmospheric measurements and relate atmospheric observations to fluxes from specific regions through atmospheric transport model simulations.

National scale inverse modelling has been successfully used for methane and other greenhouse gases in a number of countries (Manning et al., 2011; Miller et al., 2013; Ganesan et al., 2015; Henne et al., 2016; Maasakkers et al., 2021; Lu et al., 2022). Yet, to date, only three countries have successfully used this approach to estimate national scale carbon dioxide (CO_2) fluxes enabling comparisons with estimates reported in national greenhouse gas inventories: New Zealand (Steinkamp et al., 2017), United Kingdom (White et al., 2019) and Australia (Villalobos et al., 2023). While CO_2 inverse modelling studies have supported CO_2 flux estimation on larger scales (Gerbig et al., 2003; Matross et al., 2006; Schuh et al., 2010; Meesters et al., 2012; Deng et al., 2022; Byrne et al., 2023; Kou et al., 2023), their application on a national scale is still subject to limitations (Byrne et al., 2023). Top-down national scale CO_2 estimates are impacted by limited data coverage, transport model errors, inaccurate representation of the diurnal cycle, uncertainties in CO_2 background values (boundary conditions), as well as other factors, all of which contributes to the complexity of interpreting top-down CO_2 methods for improving carbon flux estimates. This complexity is further compounded by the fact that national greenhouse gas inventories are restricted to anthropogenic emissions, making it even more challenging to accurately compare the two methods.

New Zealand's unique geographical advantages (i.e., isolated landmass, far from other terrestrial sources or sinks) and current technical capabilities (i.e., high resolution modelling, high precision CO_2 observing sites) make it an excellent case study to develop, test and adapt national scale top-down methodologies. Steinkamp et al. (2017) developed the first top-down national scale inverse model for CO_2 focusing on New Zealand's carbon budget between 2011 and 2013. They estimated a national sink of -98 ± 37 Tg CO_2 yr^{-1} from the terrestrial biosphere, which is larger than that reported in New Zealand's Greenhouse Gas Inventory (1990-2022) (the 2024 Inventory, Ministry for the Environment (2024)) and prior bottom-up estimates. In particular, the inversion suggested that the south-west of New Zealand (referred to as the Fiordland region) was a large CO_2 sink. Fiordland is a region dominated by mature, indigenous forests, which are traditionally assumed to be carbon neutral (Kira & Shidei, 1967; Odum, 1969; Luyssaert et al., 2008; Holdaway et al., 2017; Paul et al., 2021). The study suggested that these environments might have a much greater potential to absorb carbon than thought previously. The authors recognised that top-down and bottom-up inventory methods are not directly comparable due to scope and methodological differences and sought to resolve discrepancies. However, after adjustments had been made for these differences between methods, the top-down results still pointed to a larger sink than inventory methods (Steinkamp et al., 2017).

The stronger than expected New Zealand CO_2 sink reported in Steinkamp et al. (2017) was intriguing. However, there were three key limitations to that study. The study only covered three years (2011-2013), which made it impossible to assess whether the sink was persistently larger than that reported in New Zealand's Greenhouse Gas Inventory or the result of variability. In addition, the study was based on a single model at ≈12 km spatial resolution, which may not be able to adequately represent the airflow in parts of New Zealand due to its complex topography (Landcare Research, 2010b). The inversion also relied on only one prior biospheric model (Biome-BGC) that was not calibrated for New Zealand's specific forest biomes.

Here, we present the results of a decade long (2011-2020) national scale CO_2 inverse model. We improved the transport model resolution used in Steinkamp et al. (2017) by a factor of ten and tested the sensitivity of our results to the choice of model. In addition, we used two prior terrestrial biosphere models, which have been tuned using country specific data. We discuss the temporal and spatial change of the CO_2 fluxes, explore the underlying processes leading to the resulting sink and highlight differences between our top-down results and bottom-up estimates from both the biosphere models and 2024 Inventory. We performed a series of sensitivity tests to ensure the robustness of our results. Our work highlights the importance of the continuous advancement and the contribution that top-down methods provide when improving how we estimate and report national scale CO_2 fluxes, providing independent assurance of the environmental and scientific integrity of our climate mitigation efforts.

2. Methods

We used a Bayesian approach (Gurney et al. (2004); Steinkamp et al. (2017) and Section 2.1) to estimate net CO_2 fluxes from atmospheric surface CO_2 measurements (Sect. 2.2). A Lagrangian dispersion transport model (Sect. 2.3) was used to simulate the pathway of the air before it reached the measurement sites. We used prior terrestrial, oceanic and anthropogenic fluxes (Sect. 2.4) and their uncertainty estimates (Sect. 2.5) to optimise the fluxes. Here, we provide an overview of the system and focus in greater detail on key advances undertaken for this work, namely a major advance to the atmospheric transport modelling and a priori estimates, particularly the terrestrial biosphere model.

~~We used atmospheric surface CO_2 measurements (Sect. 2.1) to estimate net air-sea and air-land CO_2 exchanges with a Bayesian approach based on an inversion system described in Steinkamp et al. (2017) and detailed in Sect. S1. Here, we provide a brief overview of the system and focus in greater detail on key advances undertaken for this work, namely a major advance to the atmospheric transport modelling and a priori estimates, particularly the terrestrial biosphere model.~~

~~In brief, the fluxes were estimated for 25 geographic regions (Fig. S1) on a weekly scale. We used a Lagrangian dispersion transport model (Sect. 2.2) to simulate the pathway of the air before it reached the measurement sites. We used prior terrestrial, oceanic and anthropogenic fluxes (Sect. 2.3) and their uncertainty estimates (Sect. 2.4) to optimise the fluxes.~~

2.1 Inversion system

Our inversion system estimated absolute net sea-to-air and land-to-air CO_2 fluxes, rather than scaling factors, for 25 geographic regions (Fig. 1). The fluxes were estimated on a weekly scale, with negative land-to-air fluxes suggesting a net CO_2 sink and positive values pointing to a net source. Since we estimated regional fluxes, the spatial flux pattern within regions was maintained. The inversion was based on the Bayesian cost function J, calculated as (Tarantola, 2005):

$$J = \frac{1}{2}(Tx - d)^T C_d^{-1}(Tx - d) + \frac{1}{2}(x - x_0)^T C_0^{-1}(x - x_0) \quad (1)$$

where T is the transport (jacobian) matrix, d is the data time series, x_0 is the prior flux, while C_d and C_0 are the data and prior covariance matrix, respectively. The function was minimized analytically to yield the posterior fluxes (x) and associated posterior error covariance matrix (C) (Enting, 2002):

$$x = C(T^T C_d^{-1} d + C_0^{-1} x_0) \quad (2)$$

$$C = (T^T C_d^{-1} T + C_0^{-1})^{-1} \quad (3)$$

Equation 1 represents the sum of the modelled versus measured CO_2 differences (Tx - d) and the optimized posterior versus prior flux differences (x - x_0). Each data and flux point is weighted by their uncertainty defined through the data and prior covariance matrix C_d and C_0. The main diagonal of the covariance matrices represents data and prior flux variance while off-diagonal elements contain information about the temporal and spatial correlations of the uncertainties.

The first term in Eq. 1 also includes a Gaussian smoother focusing on week-to-week flux changes as described by Steinkamp et al. (2017). We used a reduced chi test (2*J* divided by the number of observations) (Kountouris et al., 2018) to assess the fit of the inverse model to the observations. The ideal chi-squared value equals 1, with values < 1 indicating that the uncertainties in C_d and C_0 are too large while values > 1 suggest that the uncertainties are underestimated (Nickless et al., 2018). Results from the reduced chi test were used as a scaling factor to weight the data uncertainties in the inversion.

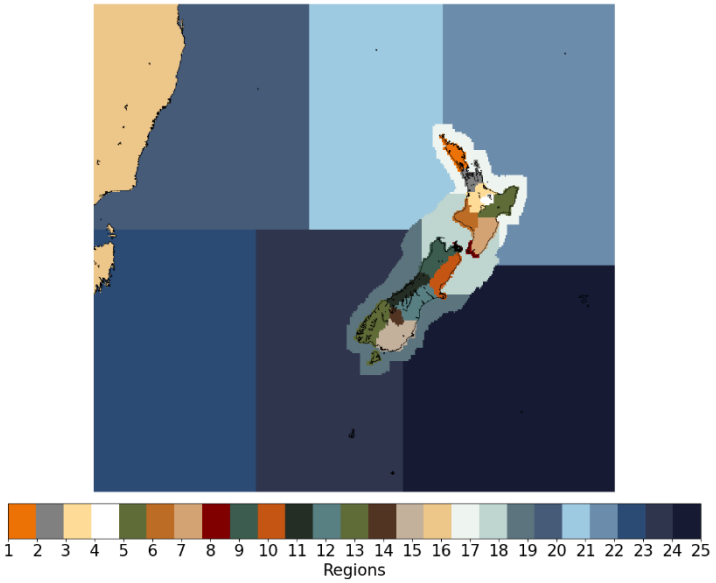

Figure 1. Domain boundaries for the 25 inversion regions, New Zealand South Island (regions 1-8), New Zealand North Island (regions 9-15), Australia (region 16), coastal ocean (regions 17-19), open ocean (regions 20-25).

2.~~1~~ 2 Sites, measurements and background

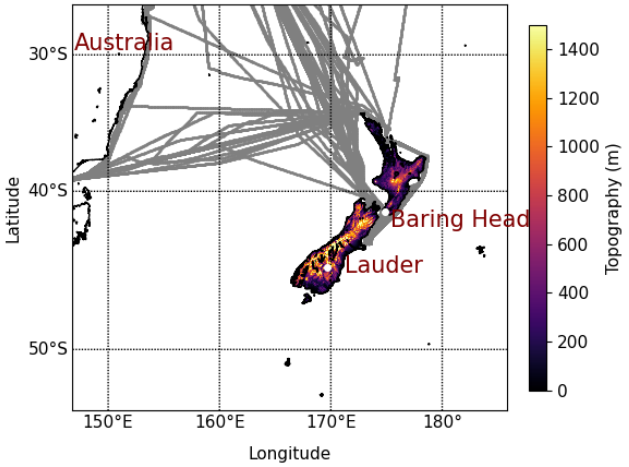

Figure 2. New Zealand's topography (zoomed in version Fig. ~~S5~~S4) with location of New Zealand long running *in situ* measurement sites, Baring Head and Lauder. Ship based measurements collected onboard the Trans Future 5 ship were used to help characterise the CO_2 in the background air (grey lines).

The posterior fluxes in the inversion were estimated from atmospheric surface measurements at two sites in New Zealand, Baring Head (Fig. ~~1~~ 2 and Fig. ~~2~~3, North Island, 41.408◦ S 174.871◦ E) and Lauder (South Island, 45.038◦ S, 169.684◦ E) (Lowe et al., 1979; Stephens et al., 2011; Brailsford et al., 2012; Stephens et al., 2013; Steinkamp et al., 2017; Smale et al., 2019). Baring Head is a coastal site, fully exposed to winds from the South and near the relatively narrow Cook Strait, while Lauder is an elevated inland location in the lee of the Southern Alps on an expansive plain (Brailsford et al., 2012; Steinkamp et al., 2017). We used hourly mean measurements averaged over 13:00 to 14:00 and 15:00 to 16:00 local time (Fig. ~~2a~~ 3a and ~~2b~~3b) when the air is well-mixed so that the CO_2 signal is representative of regional processes. The characteristics of the Baring Head and Lauder CO_2 instruments and meteorological conditions are described in detail in Sect. ~~S2~~ S1 and 2.~~2~~3.1.

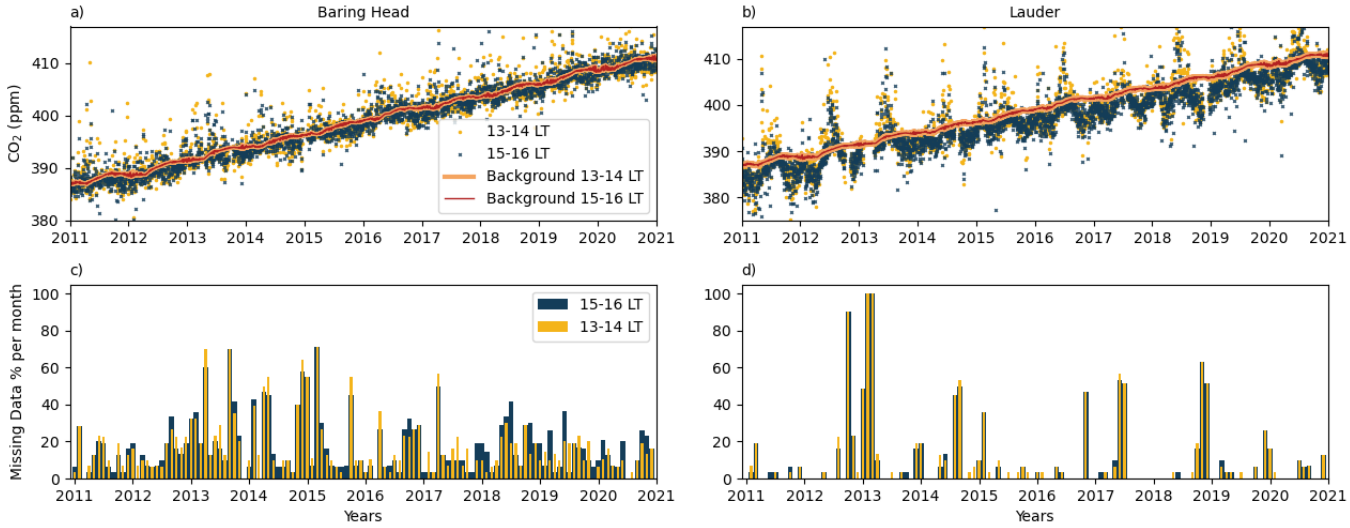

Figure 3. CO_2 measurements at Baring Head (a) and Lauder (b), yellow and blue dots represent measurements at 13:00-14:00 and 15:00-16:00 local time, the orange and red line represents the weighted southern-northern background based on Baring Head and TF5 measurements (13:00-14:00 and 15:00-16:00 local time). Data gaps are shown in c) at Baring Head and d) at Lauder.

New Zealand is located far away from other land masses and surrounded by approximately 2000 km of ocean in all directions which simplifies the construction of accurate CO_2 background. Background CO_2 represent the CO_2 mole fractions reaching New Zealand before perturbation by local influences while any deviations from those background CO_2 mole fractions are representative of processes occurring in New Zealand. We constructed the background values based on measurements collected at Baring Head to represent southerly background conditions (Manning & Pohl, 1986) and measurements on board the Trans Future 5 ship (TF5, cruising between Japan-Australia-New Zealand, held by National Institute for Environmental Studies (NIES) as the Volunteer Observing Ship (VOS) program (Terao et al., 2011; Yamagishi et al., 2012; Müller et al., 2021)~~)~~ to represent northerly background conditions (Fig. ~~1~~2). The data time series used for the inversion was constructed by subtracting background measurements from the afternoon measurements at the two sites (Fig. ~~S2~~S1).

2.~~2~~ 3 Atmospheric transport model

A Lagrangian dispersion model, NAME III (Numerical Atmospheric dispersion Modelling Environment, Jones et al. (2007)), was used to back-calculate the pathway of the air before it arrived at Baring Head and Lauder between 13:00-14:00 and 15:00-16:00 local time. We used the atmospheric transport model to link the regional total fluxes with the data time series (Steinkamp et al., 2017).

NAME III is driven by meteorological inputs from the National Institute of Water and Atmospheric Research (NIWA) operational numerical weather prediction (NWP) models. These are the New Zealand Limited Area Model

(NZLAM, ≈12 km spatial resolution) covering the 2011-2013 inversion period (Steinkamp et al., 2017) and the New Zealand Convective Scale Model (NZCSM, ≈1.5 km spatial resolution) used for the period mid 2016-2020 (Webster et al., 2008). Both models are specific configurations of the UK Met Office Unified Model (UM) (Davies et al., 2005). To fill a gap in the archived data, a custom NZCSM was configured and run in hindcast mode to generate the required NAME III input data for the period 2014-mid 2016 at ≈1.5 km (hereinafter referred to as NZCSM-like, Sect. ~~S3~~S2).

NZCSM provides approximately ten times higher horizontal spatial resolution compared with the previous work using NZLAM, which allowed us to more accurately resolve the air flows over and around New Zealand's complex terrain, especially around the South Island Southern Alps (Fig. S~~4~~5). Furthermore, at the resolution used by NZCSM, we started to be able to resolve some of the convective processes. This made it possible to run the model without a convection parameterisation scheme and, instead allowed the model dynamics to explicitly deal with convective initiation. The importance of model resolution in inversion methods has been highlighted previously (Bergamaschi et al., 2005; Baker et al., 2006; Prather et al., 2008), so the mid-term switch from NZLAM at ≈12 km to NZCSM-generated input data at ≈1.5 km was considered worthwhile to obtain the best possible wind climatology for this study.

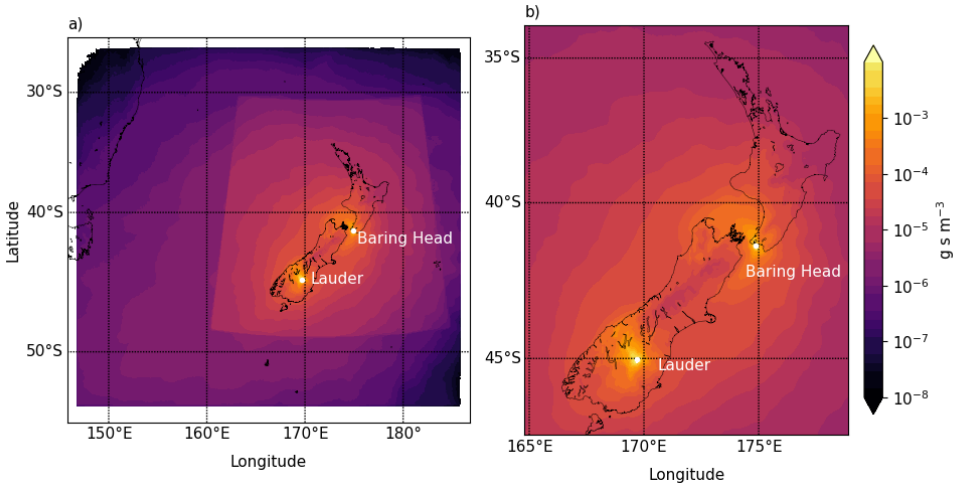

Figure 4. Combined NAME III air concentration (i.e., footprints) based on Baring Head and Lauder for 2011-2020 at 13:00-14:00 and 15:00-16:00 local release time. 2011-2013 footprints are based on NZLAM while 2014-2020 is based on NZCSM meteorology input. NZCSM covers a smaller domain relative to NZLAM. The full domain is shown on plot a) and a zoomed version on plot b).

Previous greenhouse gas inversion studies have used both time integrated (Manning et al., 2011; Steinkamp et al., 2017) and time-disaggregated modelled footprints (Gerbig et al., 2003; White et al., 2019). Our inversion used 4-day integrated air concentration (i.e., footprints, units g s m^{-3}, Fig. 4~~3~~), averaged throughout the Planetary Boundary Layer (PBL). Forced by the NWP data described above, we performed 4-day backward simulations with the NAME III model by releasing 10,000 CO_2 particles during a 1-hour period from Baring Head and Lauder each calendar day for 13:00-14:00 and 15:00-16:00 local time. Based on the pathway of the particles (air concentration) the inversion linked each measurement

point with the regions and land types that influenced the measured CO_2 signal, resulting in higher (CO_2 source regions) or lower (CO_2 sink regions) values. By the end of the 4 days, most of the particles had left the model domain (Steinkamp et al., 2017).

The modelled footprints highlight the sensitivity of the inversion to different parts of New Zealand. Based on the average 2011-2020 footprints (Fig. 43 and S34), the two sites are sensitive to most of the South Island and southern part of the North Island; however, our current network does not fully cover the northern parts of the North Island and central part of the South Island. The inversion in the years 2014-2020 used the NZCSM model with a smaller footprint domain (Fig. 43a), hence Australia and certain ocean regions were masked out. The earlier 2011-2013 inversions were based on the NZLAM model with its larger footprint domain that included the east coast of Australia. Later in Sect. 4.1 we will show that the smaller domain did not impact our inversion results.

2.23.1 Atmospheric transport model validation

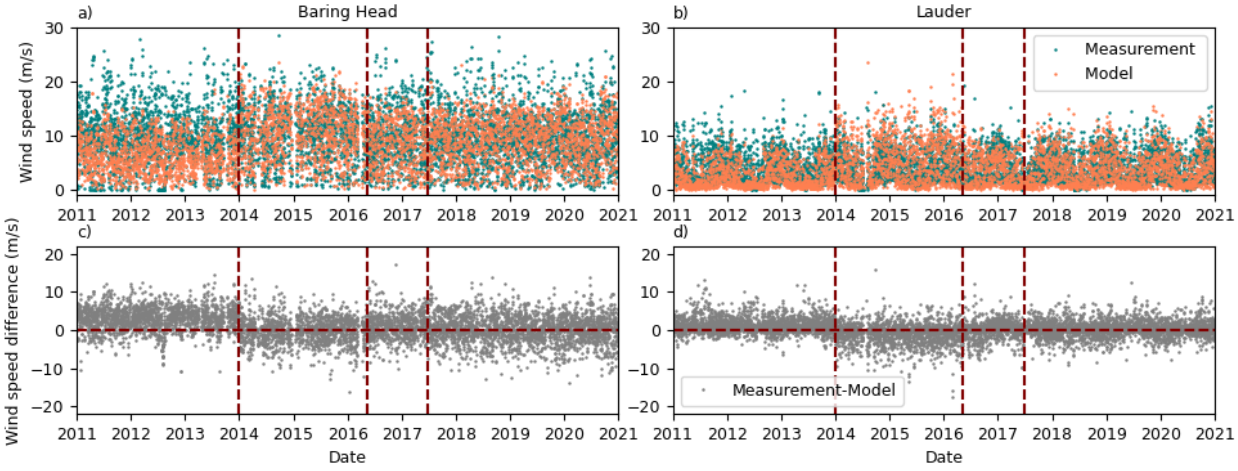

Figure 5. Hourly measured and modelled wind speed at Baring Head (a) and Lauder (b) and their difference (c and d, measurement-model) at 13:00-14:00 and 15:00-16:00 local time (as on Fig.ure 23). The horizontal lines highlight the change between different models or model version (NZLAM: 2011-2014, NZMCS-like: 2014- mid 2016, NZCSM "pre-ENDGAME": mid 2016-mid 2017 and NZCSM "ENDGame": mid 2017-2020).

We used four different models (NZLAM, NZCSM-like, NZCSM "pre-ENDGame" and NZCSM "ENDGame", see Sect. 2.23. and S3S2) as meteorological input in the NAME III atmospheric transport model. The change between different models was driven by model improvements and updates. Here, we analyse the performance of the meteorological input data by comparing the modelled data with measured meteorological variables at the two CO_2 measurement sites. Note, the geographical characteristics of the two sites are quite different (Sect. 2.1, and Steinkamp et al. (2017)).

NZLAM (used until 2014) consistently underestimated the wind speed at both sites (Fig. ~~4~~5). The performance of both the NZCSM-like and operational NZCSM model led to better agreement with the measured wind speed; except, the NZCSM-like modelled wind speeds (used from 2014-2016) were overestimated at Lauder. The accuracy of the modelled wind conditions is a critical factor in the accurate estimation of CO_2 fluxes. Moreover, precise modelled wind directions are crucial to accurately link the measured CO_2 signal with the regions that impacted the atmospheric CO_2 levels. Figure ~~5~~ 6 shows the measured and modelled wind speed and direction with both NZLAM and NZCSM for year 2018, when both model outputs were available. Other years follow a similar pattern (Fig. ~~S7~~S6). NZLAM showed a consistent bias in the wind direction for both sites, that could lead to the misattribution of CO_2 source and sink regions when NZLAM was used (years 2011-2013). As discussed in Sect. 2.~~2~~ 3 this bias was impacted by the coarser model resolution of NZLAM. For Baring Head, NZLAM suggested a dominant wind direction from the Northwest (instead of North), while for Lauder NZLAM suggested a dominant wind direction from the North ~~and Northwest~~ (instead of Northeast). Updating the model to NZCSM significantly improved the modelled wind direction and speed, reducing the model uncertainties for the post-2013 inversion years. Comparison of radiosonde PBL measurements at Lauder showed that all models underestimated the measured PBL (Sect. ~~S3~~S2.1 and Fig. ~~S6~~S5). In Sect. 4 we will further analyse the impact of the transport model on the estimated fluxes.

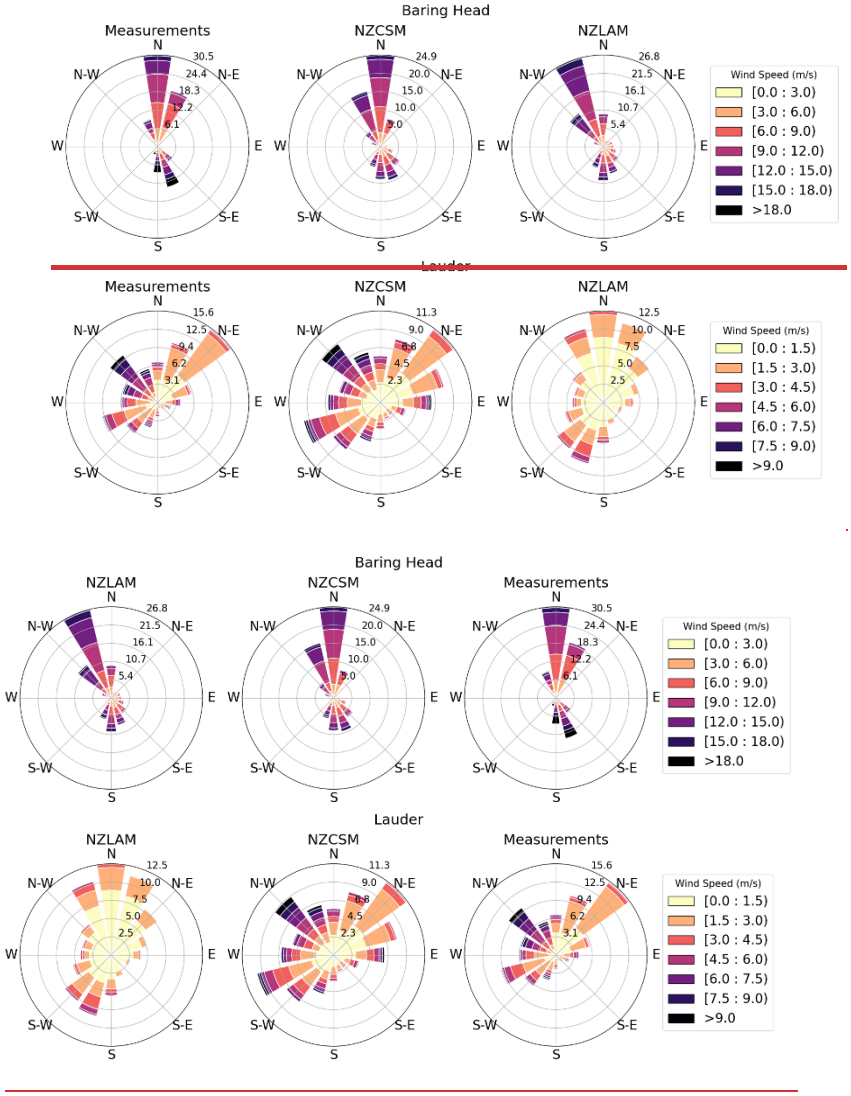

Figure 6. 2018 mean ~~measured and~~ modelled (NZLAM and NZCSM) and measured wind roses at Baring Head (top) and Lauder (bottom) when both modelled data was available.

2.~~3~~ 4 Prior information

~~We used~~The CO_2 observations were combined with prior oceanic, anthropogenic and biospheric fluxes (Table 1, Fig. ~~6~~ 7 and Fig. ~~7~~8) to estimate the weekly total posterior fluxes. CO_2 emissions from other processes, such as biomass burning and CO_2 chemical production (Bukosa et al., 2023) at the surface were presumed to be minor in New Zealand, and we excluded them from our inversion system.

2.~~3~~4.1 Prior oceanic and anthropogenic fluxes

Oceanic fluxes (Fig. ~~6a~~ 7a and ~~6c~~7c) were obtained from Landschützer et al. (2017); Landschützer et al. (2020) based on monthly open-ocean ~~air-sea~~sea-to-air CO_2 fluxes. They were further merged with calculated coastal fluxes based on the climatology of surface coastal pCO_2. The open-ocean fluxes were compiled at a resolution of 1◦ x1◦, while coastal pCO_2 values were available at a finer 0.25◦ x 0.25◦ resolution. Open-ocean flux estimates were only available up to 2019. The calculations of the 2020 open-ocean and 2011-2020 coastal CO_2 fluxes are described in Sect. ~~S4~~S3.

We used annual mean fossil fuel CO_2 emissions from the Emission Database for Global Atmospheric Research (EDGAR) v7.0 (Crippa et al., 2022). EDGAR data were available on a 0.1◦ x 0.1◦ horizontal resolution with year specific emissions for the whole inversion period. The annual EDGAR emissions over mainland New Zealand were additionally scaled to the annual gross emissions (energy, industrial process and product use, agriculture, waste) reported in the Inventory (Ministry for the Environment, 2023) (Fig. ~~6d~~7d). Note, we did not optimise fossil fuel emissions as the estimated CO_2 signal from these emissions was subtracted from the measurements at the two sites beforehand.

Table 1. Priors used for the inversion with base years, temporal and spatial resolutions.

Prior	Base Year	Native Temporal resolution	Native Spatial resolution
Ocean			
Open-ocean Landschützer et al. (2017)	2011-2019	Monthly	1◦ x 1◦
Coastal-ocean Landschützer et al. (2020)	1998-2015*	Monthly	0.25◦ x 0.25◦
Fossil Fuel			
EDGAR v7.0**	2011-2020	Annual	0.1◦ x 0.1◦
Biosphere			
Biome-BGCMuSo v6.1	2011-2020	Daily	0.05◦ x 0.05◦
CenW v6.0	2011-2020	Daily	0.05◦ x 0.05◦

*Climatology, **Scaled to 2023 Inventory

2.34.2 Prior biospheric fluxes

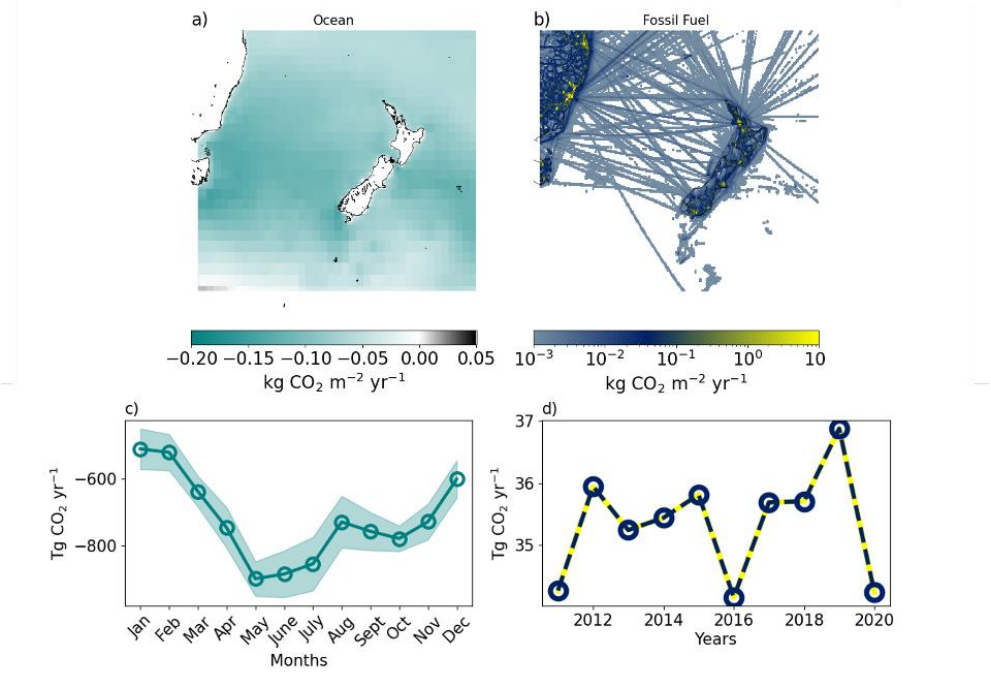

Figure 7. 2011-2020 mean spatial distribution and time series of the CO_2 oceanic fluxes based on Landschützer et al. (2017); Landschützer et al. (2020) (a, c) and fossil fuel fluxes from EDGARv7.0 (b, d). The shaded areas on c) are 1 standard deviation of the 2011-2020 mean ocean fluxes. The fossil fuel flux time series (d) is based on annual emissions as reported in the 2023 Inventory that were used to scale the EDGAR emissions over mainland New Zealand. Note, negative numbers indicate CO_2 uptake.

We have developed new prior biospheric (terrestrial) fluxes from two different models, the Biome-BGCMuSo v6.1 and CenW v6.0 (Carbon, Energy, Nutrients and Water), both optimised with country specific data.

Biome-BGCMuSo (http://nimbus.elte.hu/bbgc/) (Hidy et al., 2016; Hidy et al., 2022) is a biogeochemical terrestrial ecosystem model that simulates biological and physical processes controlling the carbon, nitrogen, and water cycles and fluxes between the atmosphere, plants and the soil. It is a branch of the Biome-BGC model developed by Numerical Terradynamic Simulation Group (NTSG) at the University of Montana (http://www.ntsg.umt.edu/project/biome-bgc.php) (Running & Coughlan, 1988; Thornton et al., 2002; Thornton & Rosenbloom, 2005; Thornton et al., 2005), which has been widely used to simulate the growth and carbon exchange of forests and grasslands in Europe and North America (Running & Coughlan, 1988; Running & Gower, 1991). Biome-BGCMuSo v6.1 represents a significant advance on previous versions of the model (Sect. 2.43.3). The model takes climate inputs of daily minimum and maximum air temperature, average daylight air temperature, precipitation, daylight vapour pressure deficit, and daylight solar radiation. Fore New Zealand implementations (Keller et al., 2014; Keller et al., 2021; Villalobos et al., 2023) these variables were obtained from NIWA's

New Zealand's Virtual Climate Station Network (VCSN), a 0.05◦ x 0.05◦ gridded data product that covers all of New Zealand from 1972-present (Tait et al., 2006; Cichota et al., 2008; Tait, 2008; Tait & Liley, 2009; Tait et al., 2012). Site specific soil information (texture, pH, and rooting depth) was obtained from the Fundamental Soil Layers database (Landcare Research, 2010a), which was re-gridded to match the VCSN. The Biome-BGCMuSo model provided fluxes for five biomes across New Zealand: dairy pasture, sheep and beef pasture, ungrazed grassland, shrub, and evergreen broadleaf forest. Fluxes for the dairy and sheep and beef biomes were calibrated and validated for New Zealand based on eddy covariance (EC) data (Sect. S4~~5~~ and Villalobos et al. (2023)). The remaining biome parameters were not optimized due to the lack of suitable EC data, and default parameters were used.

The CenW v6.0 model (Kirschbaum, 1999; Kirschbaum & Watt, 2011) is a generic forest growth model that provided CO_2 fluxes for radiata pine (*Pinus radiata*) that represents 90% of New Zealand's plantation forests (Ministry for the Environment, 2024). The CenW model also uses climate inputs from NIWA's VCSN. Like Biome-BGCMuSo, CenW also uses daily records of minimum and maximum air temperatures, precipitation, solar radiation and atmospheric humidity as well as other input data about water-holding capacity, soil texture and soil nitrogen concentration (Kirschbaum and Watt, 2011). Pine forests were parameterised in CenW based on 1309 individual observations from 101 sample plots situated across New Zealand (Kirschbaum & Watt, 2011). These observations covered the growth of stands under various stand conditions, especially climatic conditions, and plantation ages.

Both Biome-BGCMuSo and CenW produced daily estimates of Gross Primary Production (GPP), Ecosystem Respiration (ER) and Net Ecosystem Exchange (NEE = - (GPP - ER)) for each 0.05◦ pixel of their biomes covering the whole country for 2011-2020. We used a land-cover map to quantify the contribution by the modelled biomes to the combined flux from each 0.05◦ pixel across the whole of New Zealand (Sect. S4~~5~~, Table S1 and S2). Land-cover types were derived from the New Zealand Land Cover Database (LCDB) v5.0 (Landcare Research, 2020) and the LUCAS Land Use Map 2016 (Ministry for the Environment, 2016). The land cover categories were mapped into a final 10 category map (Fig. ~~8a~~9a, Steinkamp et al. (2017)) and matched with five Biome-BGCMuSo biomes (dairy pasture, sheep and beef pasture, ungrazed grassland, shrub and evergreen broadleaf forest) and *P. radiata* from the CenW model. The CenW *P. radiata* modelled by CenW was assumed to be representative of New Zealand's plantation forests, the Biome-BGCMuSo evergreen broadleaf forest category was used to model the ~~'~~other forests' category (i.e., mostly indigenous forests) and we have used ungrazed grassland fluxes for the 'other grassland' category. We assumed zero flux for non-modelled artificial surfaces, bare and lightly vegetated surface, water bodies and croplands, which together represent only a small portion of the total land area (Fig. ~~8a~~9a). Table S3 shows the proportion of each category in all regions. The resulting spatial distribution, monthly and annual contribution of the biomes is shown in Fig. ~~7~~8.

2.34.3 Prior terrestrial model improvements

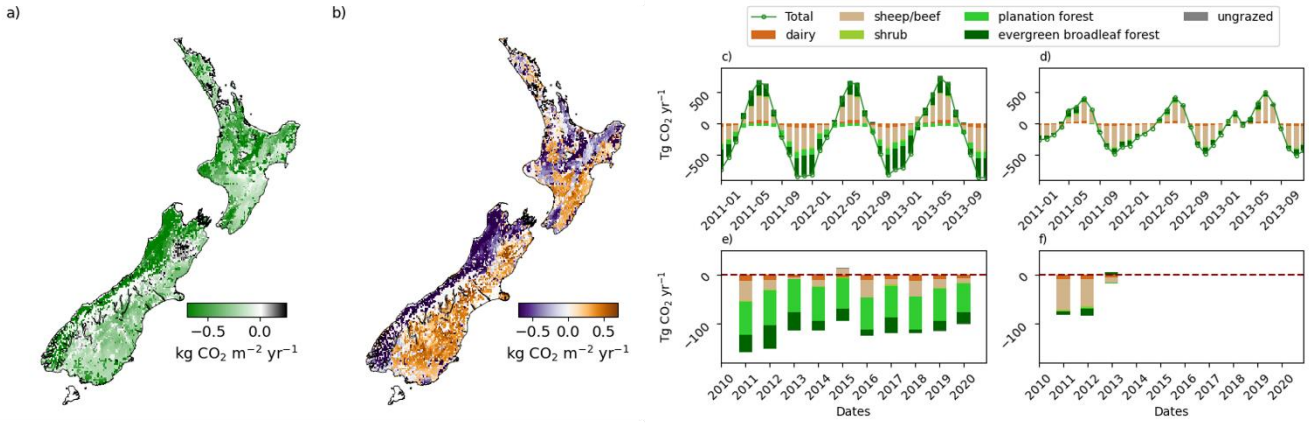

Figure 8. 2011-2013 average spatial distribution of the prior bottom-up models: Biome-BGCMuSo merged with CenW fluxes (a), the difference between Biome-BGCMuSo merged with CenW fluxes and the original Biome-BGC model (b). The right-hand side ~~middle~~ plots (c: Biome-BGCMuSo merged with CenW and d: Biome-BGC) show the monthly contribution of the fluxes for 2011-2013 when all three models were available, while the bottom plots (e, f) show the 2011-2020 annual contribution of the fluxes based on the Biome-BGCMuSo and CenW combined biomes (e) and Biome-BGC only (f).

For the previous inversion study of Steinkamp et al. (2017), all biomes were modelled with a single model, Biome-BGC v4.2 (Thornton et al., 2005; Keller et al., 2014). Here, we use additional fluxes that are representative of plantation forest fluxes from an independent model (CenW) that had been parameterised for *P. radiata* stands in New Zealand based on a comprehensive data set of available observations (Kirschbaum & Watt, 2011). Additionally, we use Biome-BGCMuSo fluxes representative of ungrazed grassland, that were not available in Biome-BGC. Biome-BGCMuSo improvements over the original Biome-BGC model include the explicit representation of management practices (such as harvesting, mowing, grazing, irrigation, etc), a 10-layer soil module (as opposed to just a single layer), more detailed nitrogen dynamics (including nitrification/denitrification processes), separate carbon and nitrogen pools for soft-stem plant tissue in addition to the existing pools for roots, leaves, leaf litter and woody stem, and implementation of plant drought stress and senescence (Hidy et al., 2016; Hidy et al., 2022). Soil hydrology has also been significantly improved (Hidy et al., 2022).

Updating Biome-BGC to Biome-BGCMuSo and CenW had a significant impact on the spatial distribution of the fluxes (Fig. ~~7a~~8a,b), leading to stronger CO_2 uptake in forested regions and weaker uptake in regions covered by sheep/beef grasslands. We found that the amplitude of the seasonal cycle in the original Biome-BGC model (Fig. ~~7d~~8d) was significantly smaller than the updated models, which has a strong impact on the seasonal cycle of the posterior fluxes in regions with low sensitivity to the measurement network. Using the CenW *P. radiata* fluxes instead of the Biome-BGCMuSo evergreen needleleaf forest fluxes led to a stronger CO_2 uptake in all regions covered by plantation forests. Merging the CenW pine forest fluxes with Biome-BGCMuSo led to a year-round net uptake by plantation forests (Fig. ~~7c~~8c,

Fig ~~S8~~S7) and stronger total annual uptake (Fig. ~~7e~~8e). The impact of CenW is limited to a small part of the country covered by the plantation forest category (Fig. ~~8a~~9a), albeit with very large per-unit consequences.

For 2011-2013, the original Biome-BGC prior estimates used in Steinkamp et al. (2017) suggested a -59 ± 34 Tg CO_2 yr^{-1} national scale uptake. Using the Biome-BGCMuSo and CenW fluxes led to a -140 ± 22 Tg CO_2 yr^{-1} net uptake, more than double of the Biome-BGC estimates. The prior Biome-BGCMuSo and CenW fluxes also suggest an overall stronger annual national sink than estimated by the inversion in Steinkamp et al. (2017) (-98 ± 37 Tg CO_2 yr^{-1}). However, in Steinkamp et al. (2017), the additional CO_2 uptake was located in regions covered by mature forests, while in this study the increased uptake in the prior flux estimates originate from regions covered by plantation forests. These model changes can influence the posterior flux estimates, and we will further discuss their impact on the inversion results in Sect. 4.

2.~~4~~ 5 Prior and posterior uncertainties

The inversion used prior uncertainty estimates to weight and balance the information between the atmospheric measurements and prior fluxes. We used the square root of the diagonal elements of the posterior covariance matrix (i.e., standard deviation, Sect. ~~S1~~2.1) as the posterior flux uncertainty for each model region. When aggregating the individual regional posterior uncertainties into larger regions (i.e., North Island), we fixed (i.e., summed) 50% of the uncertainty term.

The measurement uncertainty at Baring Head and Lauder was calculated as 1 standard deviation of the hourly measurement interval that incorporates both atmospheric and measurement variability within the hour. The background uncertainty estimates were based on the monthly standard deviations of the *in situ* data as well as differences between the measurements and the seasonal time series decomposition by the Loess algorithm smoothed curve. In addition, these uncertainties were weighted in the same way as the background data described in Sect. S1~~2~~. The data and background uncertainties were combined to give the total uncertainty applied to each data point as the root mean square (quadrature) of the two uncertainties. For uncertainties in the transport model as well as possible errors in the fossil fuel emission estimates, we assumed a minimum data uncertainty of 0.4 ppm. Lastly, we multiplied the final uncertainty by 3.9 based on the reduced chi-squared statistic (fit of the inverse model to the observations, Gurney et al. (2004)). We populated the main diagonal of the data covariance matrix with the square of the final uncertainty while off-diagonal elements of the data covariance matrix were set to zero, hence we assumed no correlation between pairs of data points.

We used the individual flux components (GPP and ER), instead of only NEE to define the prior terrestrial uncertainties. This approach mitigates low uncertainties at times, especially in spring and autumn, when fluxes were very small and could switch between negative and positive. It also provided a better representation of the CO_2 seasonal cycle in the uncertainty term (i.e., leading to lower uncertainties in winter when both GPP and ER were small). The Biome-BGCMuSo CO_2 flux uncertainties from dairy, sheep and beef and ungrazed grasslands were assumed to be 25% of their flux magnitude for NEE, GPP and ER. We assigned 30% for shrub and 50% to evergreen broadleaf forest. A higher uncertainty

was assigned to these biomes because they were not parameterised with data from New Zealand. The uncertainty for pine fluxes from CenW were assumed to be 30%, 30% and 60% of the NEE, GPP and ER flux magnitudes, respectively. The uncertainties from the individual GPP and ER components were then merged as the quadrature sum and scaled to the uncertainty magnitude of the NEE fluxes, to get an uncertainty of the net fluxes for each biome and mapped based on the land-cover map (Sect. 2.43). We have applied an additional 10% for each biome to account for uncertainties in the spatial pattern of the prior fluxes and land use map. The ocean prior uncertainty was estimated to be 50% of the flux magnitude for the coastal regions and 20% for all other regions (Roobaert et al., 2018). For the Australian, region, we assumed zero prior fluxes with a high uncertainty of 1000 Tg CO_2 yr^{-1} as in Steinkamp et al. (2017). This meant that the posterior fluxes were entirely dependent on fluxes inferred from the inversion analysis without constraint by prior assumptions. We obtained the final prior uncertainties for each of the 25 regions by aggregating the grid-scale uncertainty estimates assuming full spatial correlation. The diagonal prior covariance matrix contains the regional uncertainty estimates and off-diagonal elements were set to zero.

3 Regional CO_2 fluxes

On average, both the prior and posterior North Island fluxes showed a similar net CO_2 sink (Fig. 8b9b,c,d, Fig. 109, Figs. S89-S101, Table S4-S7). The strongest CO_2 uptake originates from the central-eastern part of the North Island (region 4 and 5, Fig. 109), which is dominated by a mixture of planted exotic and indigenous forests (Fig. 98a). However, the northern parts of the country are only weakly constrained by the measurements network (Sect 4.4) and therefore fluxes from these regions remain close to the prior estimates. The majority of exotic forests in New Zealand grow in this area, and the strong uptake in the exotic forest regions is largely driven by the prior CenW pine fluxes, which are characterised by a strong net annual CO_2 uptake.

In contrast to the North Island, there were large differences between the prior and posterior estimates for the South Island. The posterior fluxes suggested strong CO_2 uptake along the west coast of the South Island, especially in the southern part (Fig. 8c9c). Large sinks were estimated in regions covered by forests, while other regions such as the north-eastern (region 10, Canterbury) and the central-eastern region (region 12) did not show a strong sink activity. These regions are mostly dominated by grasslands. Although our prior fluxes suggest that they are weak sinks, our posterior fluxes point to a mixed carbon exchange scenario. Regions 14 (Lauder) and 15 (Otago and Southland region) are also dominated by grassland (mostly sheep and beef pasture) but showed a relatively large sink. ~10% of region 15 is also covered by a mixture of plantation and mature forests. Note, region 14 was only designed as a region around the CO_2 measurement site to capture the local CO_2 processes.

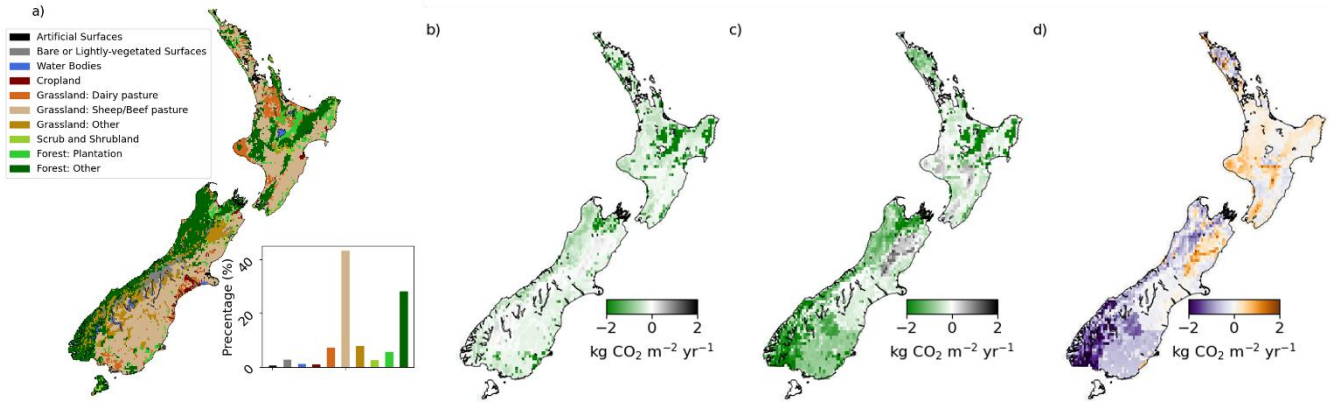

Figure 9. Land type classifications used to map the Biome-BGCMuSo and CenW biomes across New Zealand, with the total land surface area contribution of each biome (a), 2011-2020 average prior (b), posterior (c) fluxes and their difference (d, posterior-prior). The spatial distribution of the posterior fluxes was constructed based on the prior flux maps.

The north-western and central-western regions in the South Island (regions 9 and 11) are characterised by a net sink for all years, impacted by the forest activity in this area (mixture of mainly indigenous and some exotic forests). We observe a strong sink signal in New Zealand's southernmost regions as well (region 13). A large part of this region is covered by mature, indigenous forests (Fig. ~~8~~9a). Region 13 is the largest region in our model (Table S3), leading to the strongest region-based sink signal. However, the area-based estimates are within uncertainties in comparison with region 9 (Table S4-S7). Hereinafter, as in Steinkamp et al. (2017) we will also refer to region 13 as Fiordland, although it includes regions that are not part of the Fiordland National Park (i.e., western Southland, Stewart Island and western Otago).

Overall, the location of the stronger posterior CO_2 sink follows a similar pattern as found in Steinkamp et al. (2017). A large portion of the sink in the posterior estimates are in the South Island. However, where Steinkamp et al. (2017) found a strong sink localised in the southwest of the South Island (region 13), we find a much more spatially distributed sink. Although the sink is largest in region 13, other regions in the southern half of the South Island also show larger carbon uptake than the prior (regions 9, 11, 15). Averaged over the 2011-2020 period, the posterior fluxes suggest a total uptake of -111 ± 26 Tg CO_2 yr^{-1} in the South Island (69 Tg CO_2 yr^{-1} stronger uptake from the prior) and -60 ± 16 Tg CO_2 yr^{-1} in the North Island (17 Tg CO_2 yr^{-1} weaker uptake from the prior). The area-based posterior flux estimates suggest a -0.64 ± 0.15 kg CO_2 m^{-2} yr^{-1} sink activity for the South Island and -0.42 ± 0.11 kg CO_2 m^{-2} yr^{-1} for the North Island, a stronger sink activity from the prior South Island estimates (-0.24 ± 0.09 kg CO_2 m^{-2} yr^{-1}) and weaker for the North Island (-0.54 ± 0.08 kg CO_2 m^{-2} yr^{-1}). However, we note that our measurement network has lower sensitivity to the northern part of the North Island (Steinkamp et al., 2017), hence additional and stronger sink or source regions can appear when adding measurements from additional sites into our inversion system (in case of a biased prior flux assumption).

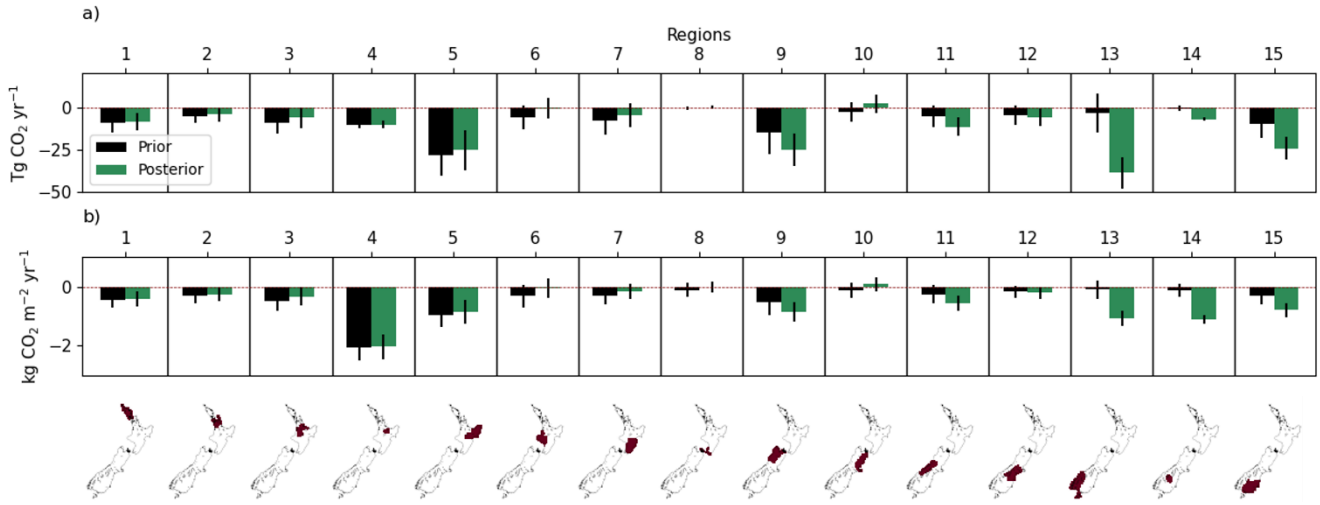

Figure 10. 2011-2020 average CO_2 prior (black) and posterior (green) net ~~air-land~~land-to-air flux estimates for the 15 inversion land regions in units of Tg CO_2 yr^{-1} (a) and area-based flux estimates in kg CO_2 m^{-2} yr^{-1} (b). The error bars represent the standard deviation. The inversion land regions are designed to also include small local regions around the measurement sites (i.e., Baring Head: region 8; Lauder: region 14). The purpose of these regions is to capture the local CO_2 exchange signal (Steinkamp et al., 2017).

3.1 Seasonal variability

The posterior fluxes are characterised by stronger springtime uptake and weaker winter emissions compared to the prior (Fig ~~10~~11, Fig. ~~11~~ 12 and Fig. ~~12~~13). The stronger posterior uptake in spring suggest that the peak of the growing season is potentially occurring earlier relative to prior estimates. However, in Sect. 4.3 we discuss a potential impact of the CO_2 diurnal cycle bias on the spring/summer estimates. Conversely, the posterior fluxes in winter and autumn show robust discrepancies relative to the prior estimates. On average winter periods in the posterior fluxes suggest a weaker net source, while during autumn we find a neutral CO_2 exchange, suggesting suppressed or offset respiration by additional CO_2 uptake due to plant activity during these periods.

The regions in the South Island that showed larger CO_2 uptake than the prior estimates (regions 9 and 13, Fig. ~~11~~ 12 and ~~S12~~S11), all show reduced net CO_2 flux into the atmosphere (e.g., suppressed respiration) during autumn/winter, suggesting CO_2 uptake throughout the year. The weak autumn/winter CO_2 net source is most pronounced in region 9, which is dominated by indigenous forests. Similar to region 9, the Fiordland area (region 13) also shows only weak source activity during autumn/winter periods. Although traditionally it has been assumed that mature forests are almost carbon neutral (Kira & Shidei, 1967; Odum, 1969; Luyssaert et al., 2008), our results suggest that these environments can potentially have significant carbon uptake. The low autumn/winter CO_2 release was not evident in Steinkamp et al. (2017), possibly due to

the shorter inversion time period (2011-2013), measurement gaps, and strong drought conditions during 2012 and 2013 that released larger amounts of CO_2 to the atmosphere.

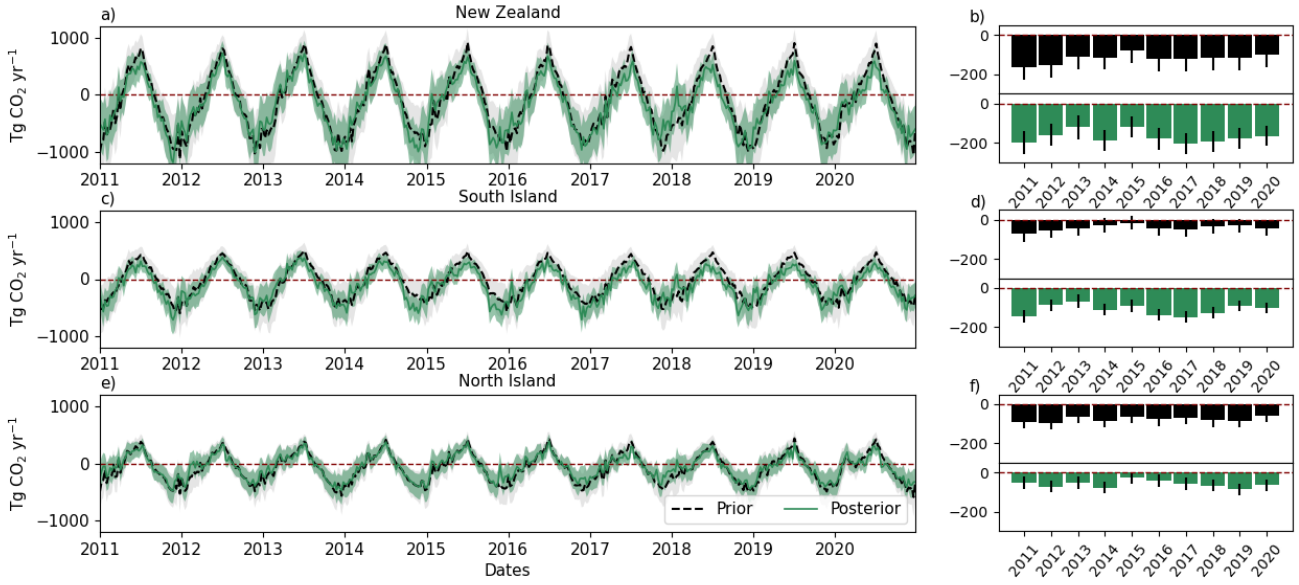

Figure 11. Weekly time series (a, c, e) and annual (b, d, f) CO_2 prior (black) and posterior (green) net ~~air-land~~land-to-air flux estimates for New Zealand (a,b), the South Island (c,d) and North Island (e,f).

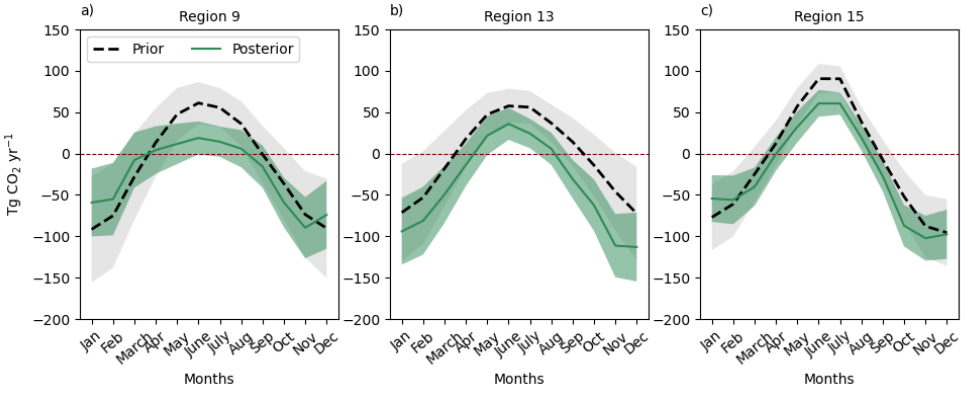

Figure 12. 2011-2020 average monthly CO_2 prior (black) and posterior (green) net ~~air-land~~land-to-air flux estimates for selected regions.

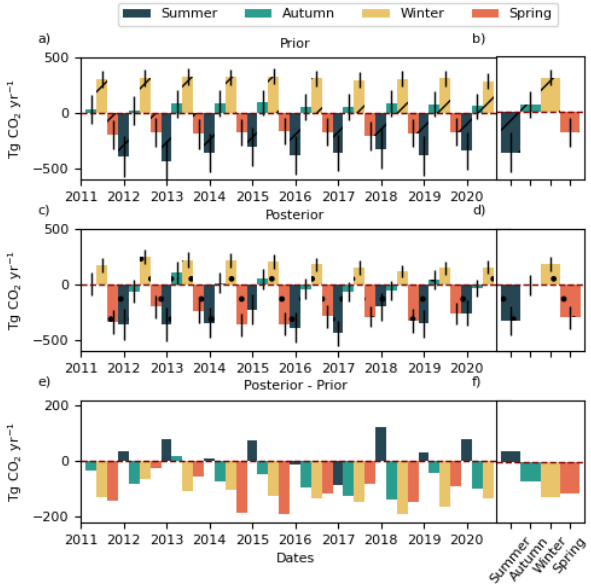

Figure 13. Mean South Island annual seasonal (summer – December to February, autumn – March to May, winter – June to August, spring – September to November) CO_2 prior (a), posterior (c) net ~~air-land~~land-to-air flux estimates and their difference (e). Subplots b), d) and f) show the 2011-2020 average values for each season. The first and last season (summer) is removed from the plot and calculation due to insufficient number of months to calculate the seasonal average. All the regions can be found in Figs. ~~S13~~S12-~~S14~~S13.

3.2 Interannual variability

Steinkamp et al. (2017) found stronger CO_2 uptake during 2011-2013 than that reported in the Inventory (Ministry for the Environment, 2015) and the prior bottom-up model estimates (Biome-BGC). However, the posterior CO_2 fluxes over the three years showed a decreasing trend, potentially pointing to a transient sink. The decreasing trend was heavily influenced by measurement gaps and drought conditions, and a longer inversion period was needed to ascertain whether the inferred stronger posterior CO_2 sink was real and sustained over a longer observation period.

Based on our decade-long inversion, we found that the sink observed between 2011-2013 did not diminish in subsequent years, thus confirming that the atmospheric CO_2 signal supports the existence of an overall stronger national scale CO_2 uptake than reported in the 2024 Inventory and the prior fluxes. We find differences in the year-to-year changes of the prior and posterior fluxes in both the South and North Island (Fig. ~~10b~~11b,d,f). The most pronounced interannual variability in the posterior fluxes are in regions 13 and 15 (Fig. ~~S12~~S11); however, we are cautious in interpreting the interannual variability due to additional uncertainties that impact the flux estimates. These include the impact of

measurement data gaps (Fig. ~~2e~~3c,d), that will tend to keep the posterior fluxes closer to the prior flux estimates, as well as the impact of changes in the transport model that will be discussed in Sect. 4.

4 Sensitivity and validation

Uncertainties in top-down flux estimates on a regional to national scale are caused by a number of factors including 1) data availability in the country-wide measurement network (Berchet et al., 2013; Kountouris et al., 2018); 2) challenges in defining an appropriate background (Göckede et al., 2010); 3) biases in the prior fluxes (Peylin et al., 2011; Saeki & Patra, 2017; Philip et al., 2019); 4) atmospheric transport model and mixing errors (Baker et al., 2006; Prather et al., 2008); 5) aggregation errors (Kaminski et al., 2001; Turner & Jacob, 2015); and 6) the specific technical setup and assumptions in the inversion such as Gaussian assumptions (Miller et al., 2014) or representation of the CO_2 diurnal cycle (Gerbig et al., 2003; White et al., 2019). We conducted a suite of tests to assess the sensitivity of our results to specific setups and assumptions in our inversion system and used different diagnostics (i.e., residuals, Degrees of Freedom, Averaging) to quantify and better understand the uncertainty and possible biases in the performance of the inversion.

4.1 Transport model

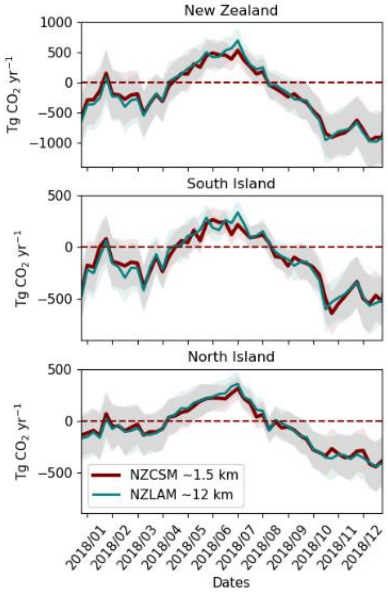

Figure 14. Weekly posterior flux estimates using NZLAM (≈12 km) and NZCSM (≈1.5 km) meteorological input for year 2018.

We compared our inversion results using NZCSM (≈1.5 km) and NZLAM (≈12 km) inputs for the NAME III model to identify the impact of the resolution of the transport model on the posterior CO_2 fluxes. We ran the inversion for 2018 when both model outputs were available.

The differences in the posterior flux estimates were more pronounced for the individual inversion regions (Fig ~~S15~~S14), but these differences averaged out when aggregated to larger regions (Fig. ~~13~~14). On average, using the updated ≈1.5 km NZCSM input led to a slight additional 2.3 Tg CO_2 yr^{-1} increase of the sink for New Zealand as a whole (South Island: 0.5 Tg CO_2 yr^{-1}, North Island: 1.8 Tg CO_2 yr^{-1}). The Fiordland region showed a 10 Tg CO_2 yr^{-1} difference in the posterior fluxes when using different meteorological input, a reduced sink when using NZCSM (Fig. S14). In Sect. 4.3 we identify additional changes in the posterior fluxes, driven by the changeover between transport models that was not captured in the 2018 data.

4.2 Prior and background estimates

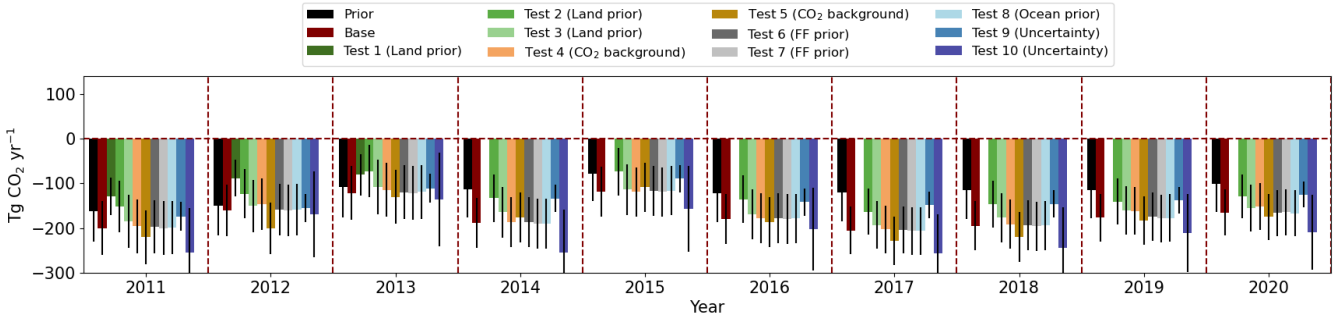

Figure 15. Annual posterior flux estimates from the sensitivity tests, as well as the prior (black) and posterior (red) estimates from our base inversion. A detailed description of the setup for each test can be found in Table 2.

The estimated posterior fluxes are strongly dependent on the choice of the prior land fluxes as well as their estimated uncertainties. We compared our base inversion (using combined Biome-BGCMuSo and CenW fluxes) with the Biome-BGC fluxes and land cover-map from Steinkamp et al. (2017) (Test 1, Fig. ~~14~~15, Fig. ~~S16~~S15). Updating the prior land fluxes and land cover-map resulted in a 61 ± 14 Tg CO_2 yr^{-1} increase in the national CO_2 sink, representing a 73% change in the posterior fluxes. These results are additionally impacted by the weaker measurement constraint in the North Island (i.e., the posterior estimates will be strongly impacted by the prior). Next, we tested an inversion setup where we retained the Biome-BGCMuSo evergreen needleleaf forest biome category for the plantation forest category instead of the CenW pine fluxes (Test 2). Using the Biome-BGCMuSo evergreen needleleaf forest fluxes instead of CenW pine fluxes led to a 44 ± 6 Tg CO_2 yr^{-1} sink reduction in the posterior fluxes. As shown in Fig. ~~7~~8, this is expected due to the all-year-round CO_2 uptake in the CenW pine fluxes, which is not present in the Biome-BGCMuSo evergreen needleleaf forest fluxes. We also tested the land cover-map introduced in Steinkamp et al. (2017) with the updated prior fluxes in our base inversion (Test 3). Using the older

land cover-map described in Steinkamp et al. (2017) led to a 13 ± 5 Tg CO_2 yr^{-1} sink reduction in the posterior fluxes. Reducing the prior land uncertainties in our base inversion by a half (Test 9) reduced the posterior CO_2 sink due to a tighter constraint on the prior fluxes, while doubling the uncertainties (Test 10) further increased the CO_2 sink in regions that were well observed by the measurement network.

Table 2. Inversion sensitivity tests*. ~~**Test 9 and 10 (not shown in the table) are the same as the base setup but with half and double the prior land uncertainty.**~~ **All simulations used NZLAM input for 2011-2013 and NZCSM for 2014-2020.**

	Land cover	Land prior (uncertainty)	Ocean prior	Fossil fuel prior	Background CO_2
Base	LCDB v5.0	Biome-BGCMuSo + CenW	Landschützer	EDGAR v7, scaled**	BHD + TF5***
Test 1	LCDB v5.0	Biome-BGC	Landschützer	EDGAR v7, scaled**	BHD + TF5***
Test 2	LCDB v5.0	Biome-BGCMuSo	Landschützer	EDGAR v7, scaled**	BHD + TF5***
Test 3	LCDB v3.0	Biome-BGCMuSo + CenW	Landschützer	EDGAR v7, scaled**	BHD + TF5***
Test 4	LCDB v5.0	Biome-BGCMuSo + CenW	Landschützer	EDGAR v7, scaled**	BHD***
Test 5	LCDB v5.0	Biome-BGCMuSo + CenW	Landschützer	EDGAR v7, scaled**	CarbonTracker
Test 6	LCDB v5.0	Biome-BGCMuSo + CenW	Landschützer	EDGAR v4.2	BHD + TF5***
Test 7	LCDB v5.0	Biome-BGCMuSo + CenW	Landschützer	EDGAR v7	BHD + TF5***
Test 8	LCDB v5.0	Biome-BGCMuSo + CenW	Takahashi	EDGAR v7, scaled**	BHD + TF5***
Test 9	LCDB v5.0	Biome-BGCMuSo + CenW (1/2 prior uncertainty)	Landschützer	EDGAR v7, scaled**	BHD + TF5***
Test 10	LCDB v5.0	Biome-BGCMuSo + CenW (2x prior uncertainty)	Landschützer	EDGAR v7, scaled**	BHD + TF5***

*~~NZLAM for years 2011-2013 and NZCSM for years 2014-2020.~~ Not all tests were performed for the whole inversion period (2011-2020) due to the lack of year specific data for certain sensitivity tests.

** scaled refers to scaling the values to the 2023 Inventory estimates

***BHD: Baring Head, TF5: Trans Future 5

Our sensitivity tests suggest the choice of background has little impact on the inverse estimates for New Zealand, which is likely due to its location far removed from most terrestrial sources and sinks. We trialled three different choices of background: our base inversion based on steady interval data at Baring Head combined with ship-based observations, CO_2 from Baring Head only (Test 4), and CarbonTracker CO_2 estimates (version CT2022, Jacobson et al. (2023)) (Test 5). Using Baring Head only decreased the posterior sink (6 ± 5 Tg CO_2 yr^{-1}), while using CarbonTracker increased the sink (12 ± 15 Tg CO_2 yr^{-1}). The differences in the posterior fluxes from all other sensitivity tests were also small. We found low sensitivity to the choice of the anthropogenic prior flux fields (Tests 6 and 7). We have tested different ocean prior fluxes (Test 8) to

highlight potential CO_2 transfer from the land to the coastal regions and ocean but found low sensitivity to the choice of ocean priors as well. In summary, using updated priors resulted in an increase of the posterior sink, and increasing the prior uncertainties further increased the posterior sink.

4.3 Diurnal variability

We performed an additional sensitivity test to assess the implications of the lack of the CO_2 diurnal cycle in our prior land fluxes. Due to the use of weekly prior land fluxes, time integrated footprints and afternoon CO_2 measurements, the modelled terrestrial diurnal cycle could not be fully resolved. Omitting night-time measurements and hourly prior land CO_2 fluxes could potentially result in overestimated negative posterior fluxes (i.e., sink) due to the exclusion of the CO_2 diurnal cycle. We excluded night-time measurements due to conditions such as lower wind speeds, weak vertical mixing and a shallow PBL. Measurements collected during these conditions primarily reflect local CO_2 exchange processes and are not representative of processes at larger regional scales. Further, both Biome-BGCMuSo and CenW simulate biospheric fluxes at a daily native temporal resolution.

We performed an Observing System Simulation Experiment (OSSE) to investigate the impact of using afternoon measurements with weekly prior land prior fluxes in our base inversion system. Our experiment used a synthetic CO_2 dataset from Baring Head and Lauder at 13:00-14:00 and 15:00-16:00 local time that had been created with dis-aggregated hourly footprints and hourly prior land fluxes. Since the prior models do not simulate the CO_2 diurnal cycle, we used highly idealised hourly fluxes as described in Steinkamp et al. (2017). We assigned the same prior flux and measurement uncertainties to the synthetic dataset as in our base inversion. The experiment used the same land prior fluxes as the ones used for the synthetic data creation but was averaged to weekly values (i.e., excluding the diurnal cycle). The difference between the prior (i.e., true) and posterior estimates (and the ability of the posterior to recover the "true" diurnal cycle) was expected to highlight the impact of the temporal resolution in the land prior (i.e., lack of a diurnal cycle) on our inversion results. However, this test does not reflect the impact of the inclusion of night-time measurements in the inversion system ~~(Sect. 7)~~.

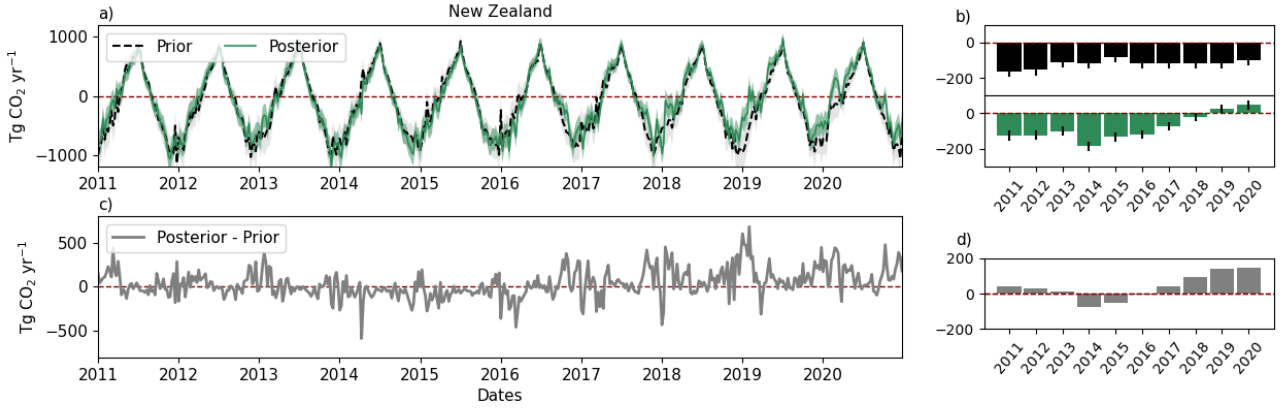

Figure 16. Weekly (a) and annual (b) CO_2 prior (black) and posterior (green) net ~~air-land~~land-to-air flux estimates for New Zealand from the diurnal cycle test. The difference between the posterior and prior estimates is shown on c) and d) Tg CO_2 yr^{-1}.

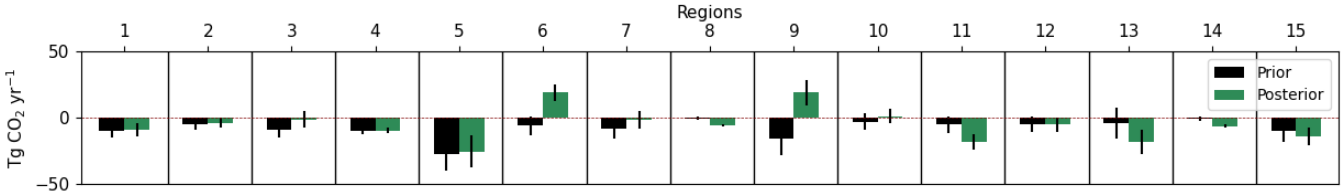

Figure 17. 2011-2020 average CO_2 prior (black) and posterior (green) net ~~air-land~~land-to-air flux estimates for the 15 inversion land regions from the diurnal cycle test.

Identical prior and posterior fluxes would suggest that there is no bias in our inversion system, while any difference between the two values points to a potentially over- or underestimated CO_2 sink or source. Averaged over all of New Zealand, we did not see a consistent offset between the prior and posterior fluxes (Fig. ~~15~~16); instead, the results suggest both over- and under-estimated CO_2 fluxes during certain time periods. The summer/spring periods point to a potential diurnal cycle bias; however, this bias is not present during autumn/winter periods when our results suggest suppressed respiration (Fig. ~~15~~ 16 and ~~S19~~S18).

We find a strong interannual variability of the diurnal cycle bias which is impacted by the transition between different meteorology input fields in our transport model, described in Sect. 2.3~~2~~. The impact of the transport model on the posterior fluxes is highlighted in the regional plots shown in Fig. ~~S17~~S16. The diurnal cycle test suggests that, on average, the strong sink observed in the Fiordland (region 13) and Southland region (region 15) is overestimated (Fig. ~~16~~17) and underestimated along the West Coast (region 9). However, the results for Fiordland and Southland suggest a mixture of both over- and under-estimated CO_2 fluxes, with an overestimated sink during 2011-2013, when NZLAM was used, while for later years the overestimated sink due to the diurnal cycle bias is less pronounced, and the results even suggest and underestimated sink (Fig. ~~S17~~S16). We note that these results are based on highly idealized hourly prior fluxes that can

introduce additional uncertainties in the estimated bias. In the North Island, our inversion system tends to underestimate the sink and points to reduced uptake during spring/summer periods (Fig. ~~S18~~S17). A 37 ± 26 Tg CO_2 yr^{-1} difference exists between the prior and posterior fluxes. Biases in the South Island, on average suggest on underestimated sink of 1 ± 48 Tg CO_2 yr^{-1}. Similar to the South Island regions the bias towards an overestimated sink is more pronounced for the earlier record of the inversion and this bias was mitigated after transport model improvements were made. Overall, in the context of an overestimated sink, the sensitivity to the diurnal cycle were less pronounced for later years as the NZCSM model improved (Sect. 2.3~~2~~).

4.4 Inversion performance

Analysis of the residuals (model - observation) (Fig. 1~~8~~7) contains information about potential biases impacting the posterior fluxes. Residuals represent the differences between the modelled and measured CO_2 mole fractions, with the modelled values being the optimized CO_2 mole fractions by propagating the posterior flux estimates through the inversion. A positive mean bias would suggest that the modelled CO_2 values are higher relative to the measurements and that the inversion struggles to reproduce the low CO_2 observations, while a negative bias would suggest the opposite, i.e., lower modelled CO_2 values relative to measurements.

We find a positive bias in our base inversion for both sites and measurement times. Baring Head shows similar residual values between the 13:00-14:00 and 15:00-16:00 local time with a bias of 0.19 ppm. The residuals at Lauder show a higher mean bias, 0.59 ppm at 13:00-14:00 and 1.39 ppm at 15:00-16:00. We also find a small temporal/seasonal pattern of the residuals, with higher values during winter and lower values during summer periods. As discussed in Steinkamp et al. (2017) there is a strong indication that the biases in the residuals are a product of biases between measured and modelled PBL depth or biases from excluding the diurnal variability of CO_2 in the data (by using afternoon data only) and prior fluxes.

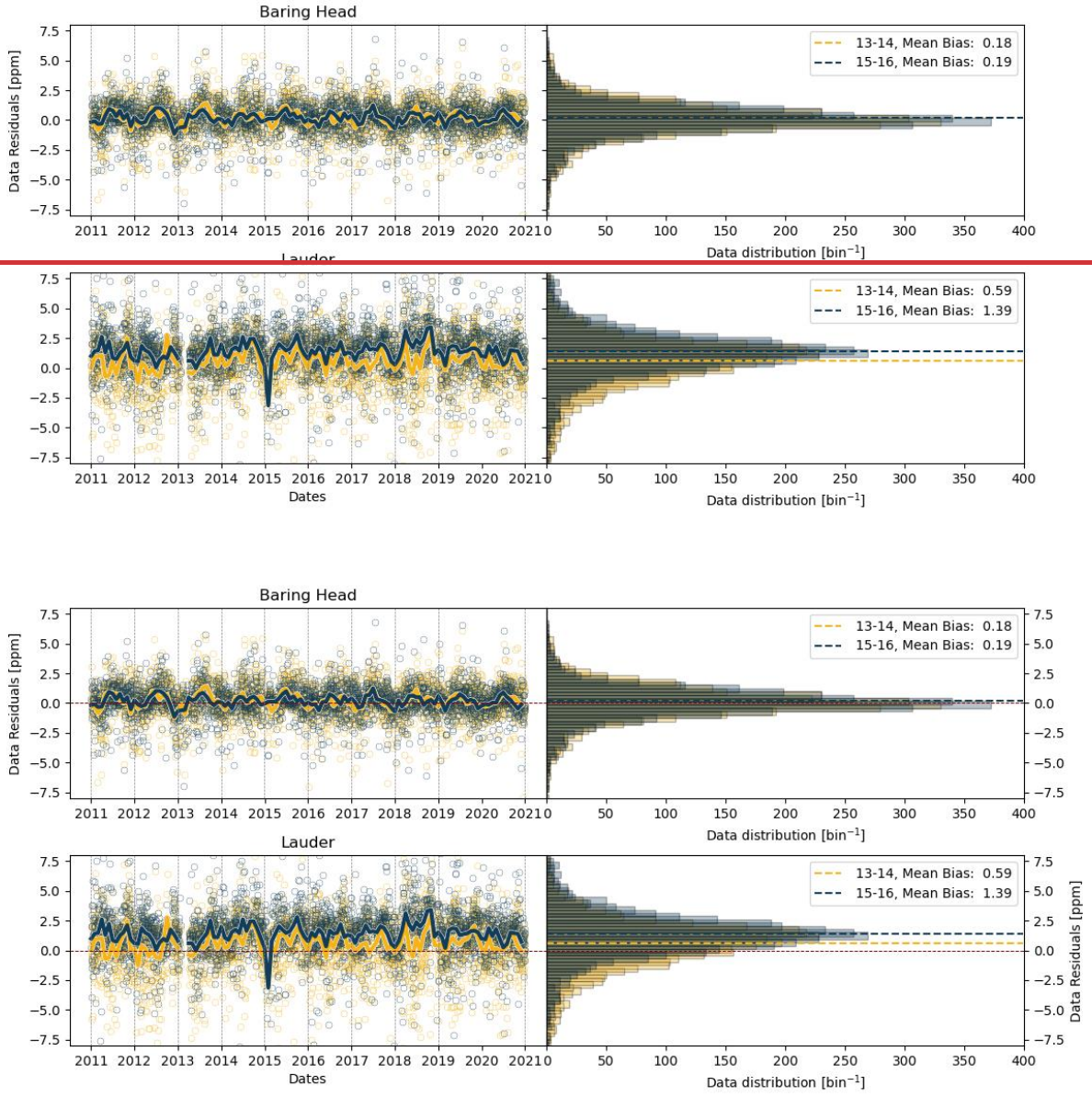

Figure 18. Modelled ~~and~~ - measured CO_2 ~~differences~~ (residuals) at 13:00-14:00 and 15:00-16:00 local time at Baring Head (top) and Lauder (bottom) for 2011-2020. The left plots show the residuals for each day (circles) and seasonal cycle of the residuals (solid lines). The right plots show the residual distribution with the mean bias (dashed line). The red dashed line represents the zero line.

Regional Degrees of Freedom (DOFs, Fig. ~~18a~~19a,b) and Averaging Kernel (AK, Fig. ~~18c~~ 19c and S19) (Rodgers) provide information about the ability of our measurement system to constrain the fluxes. The DOFs are the trace of AK and they provide a quantitative measure of the number of independent pieces of information in the constrained fluxes, provided

by the measurements. Based on the monthly covariance matrices, each region can have a maximum of 120 DOFs for the whole inversion period (i.e., 12 per year, 10 inversion years). Regions with higher DOFs suggest stronger flux constraints. Our results suggest that the South Island regions have greater measurement sensitivity than the North Island regions, and are better constrained by the current observational network, as indicated by higher DOF values, which signify stronger observational influence on the inversion results. The DOFs exhibit seasonal variation, with certain regions, particularly in the South Island, generally showing higher DOFs during austral summer periods. Winter periods and regions in the North Island, especially in central and northern areas, have lower DOFs, indicating a greater reliance on prior emissions estimates due to weaker observational constraints. The mean DOF map further supports this, showing higher sensitivity in the South Island (Fig. ~~18c~~19c).

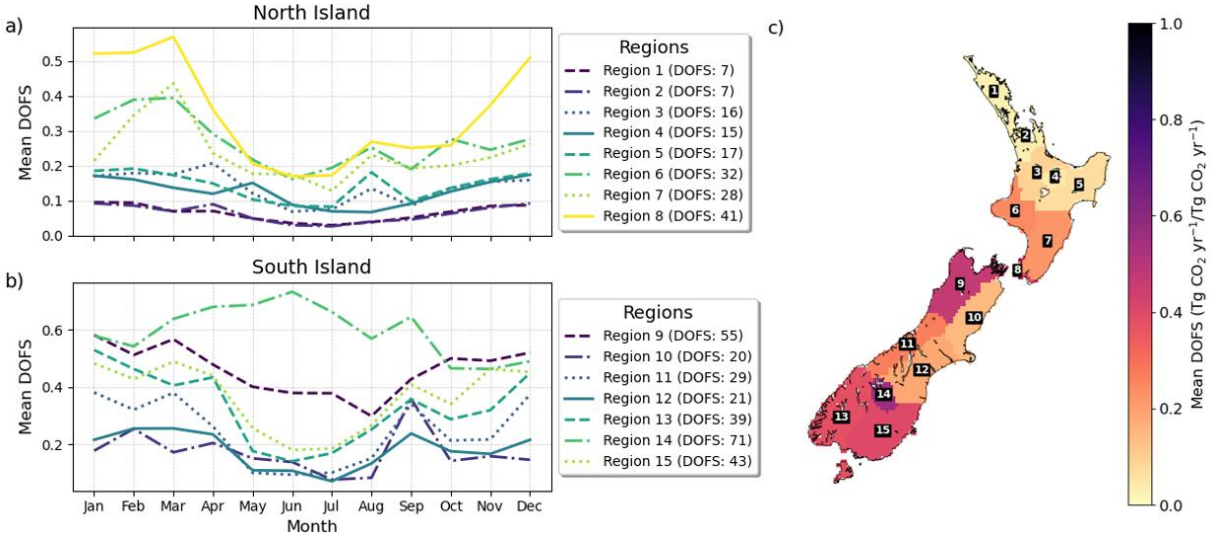

Figure 19. Monthly mean Degrees of Freedom (DOFs) for each inversion region (a, b), with total DOFs for each region shown in the legend. The full timeseries for each region is shown in Fig. ~~S20~~S19. Subplot c) shows the average 2011-2020 DOFs for each inversion region, with labelled region numbers.

The low off-diagonal elements of the covariance matrix (Fig. ~~S21~~S20) suggest that the different regional posterior fluxes can be individually constrained. The Fiordland inversion region on average (region 13) showed a stronger correlation with region 15, suggesting that the larger posterior sink in region 15 is potentially influenced by region 13.

5 CO_2 exchange processes

5.1 Understanding differences between the prior and posterior

The main difference between our posterior and prior estimates is the suppressed autumn/winter respiration in the posterior (Fig. ~~10~~11). ~~Both features are~~This feature is the strongest in regions that are dominated by forests and well constrained by our observational network (i.e., South Island). The strongest sink occurs in regions dominated by mature indigenous forests, which suggests that these forests may be a more efficient carbon sink than suggested by the terrestrial biosphere model. Common assumptions in bottom-up terrestrial biosphere models may play a role in the resulting differences between the posterior and prior estimates. These include the response of the model to erosion and landslide disturbance, impact of drought and freezing, modelling of animal respiration, biases in forest model parameters, representation of harvest and replanting cycle.

Most models, such as Biome-BGCMuSo, do not accurately represent rapid accumulation of organic matter in vegetation and soils nor burial and preservation following erosion and/or landslide disturbance (Stallard, 1998; Dymond, 2010; Berhe et al., 2018). Further, seasonal patterns of respiration could be overemphasised in Biome-BGCMuSo simulations because the model parameters have been developed for highly seasonal temperate environments with regular freezing and/or drought. This could result in overestimates of respiration in the physiologic responses of decomposer organisms to drought or freezing (Schnecker et al., 2023); however, these are expected to be infrequent events in the New Zealand regions where significant sinks relative to the priors have been found.

Further, a possible explanation for the discrepancy between the prior and posterior values in grassland regions is animal respiration (i.e., dairy cows respire about 50 % of the carbon they eat, Sect. 5.2.2), which is not included in the Biome-BGCMuSo model, used to create the prior estimates. This would impact the main agricultural regions, leading to a reduced net sink or a small source in the prior. We observe this correction of the prior in major agricultural/animal regions in the North Island (region 3, 6, 7), as well as region 10 in the South Island. Regions 12 and 15 are also strong agricultural regions; however, we do not observe this correction, presumably due to biases in other carbon exchange processes.

In the Biome-BGCMuSo model, the evergreen needleleaf and broadleaf forest categories (planted and indigenous forests) are not optimised for New Zealand. The model uses the default parameters that were tuned to Northern Hemisphere forests (White et al., 2000; Pietsch et al., 2005; Hidy et al., 2022). The CenW model provides pine flux estimates (representative of plantation forests) that were optimised for New Zealand conditions (Kirschbaum & Watt, 2011). Figure ~~19~~20 shows the average 2011-2020 NEE, GPP and ER seasonal cycle, as well the mean 2011-2020 contribution from the evergreen broadleaf forest, evergreen needleleaf forest and CenW pine categories, mapped based on the landcover map shown in Fig. ~~8a~~9a.

There are notable differences between the exotic forest flux estimates in the two models. The CenW pine fluxes show year-round net uptake while the Biome-BGCMuSo evergreen needleleaf forest fluxes suggest a seasonal cycle with uptake during summer periods and respiration during winter (Fig. ~~19a~~20a). The Biome-BGCMuSo evergreen needleleaf forest category shows a similar annual flux magnitude between GPP and ER (Fig. ~~19e~~20e) but with a stronger production, resulting in an overall net -12 Tg CO_2 yr^{-1} sink (Fig. ~~19d~~20d). Note, however, that the evergreen needleleaf forest fluxes modelled with Biome-BGCMuSo do not include the effects of the harvest and replanting cycle typical of managed plantation forests (due to computational limitations the harvest module in Biome-BGCMuSo was not activated). Plantation forests tend to have greater GPP relative to ER, as harvested material is generally transported elsewhere before it starts decomposing and releasing CO_2, and young replanted forests grow and accumulate carbon rapidly. A significant portion of New Zealand's raw wood products are exported (12.1 ± 3.7 Tg CO_2 yr^{-1}; Villalobos et al. (2023)), so if the harvested carbon is eventually released to the atmosphere, it would not be detected in measurements over New Zealand. The Biome-BGCMuSo evergreen needleleaf forest fluxes are more representative of mature, unmanaged pine forest. The CenW model suggests larger differences between GPP and ER, with stronger GPP, resulting in an annual net sink of -61 Tg CO_2 yr^{-1} (2011-2020 average, Fig. ~~19d~~20d) for the pine forested areas, and year-round net uptake. Winter temperatures in New Zealand are generally mild, hence allowing year-round plant activity. Moreover, other studies have also shown that winter conditions in New Zealand can lead to year-round productivity under other vegetation covers (Campbell et al., 2014), and the high productivity of pine forests in New Zealand is consistent with extensive forest-inventory data in the country (Kirschbaum & Watt, 2011).

The Biome-BGCMuSo evergreen broadleaf forest category shows an NEE seasonal cycle that is similar to the evergreen needleleaf forest category, but with a weaker amplitude (Fig. ~~19a~~20a). Averaged for 2011-2020, it results in a -26 Tg CO_2 yr^{-1} net uptake (Fig. ~~19d~~20d). Note, this uptake is not directly comparable to the evergreen needleleaf forest fluxes since native forests cover a larger area across New Zealand (Fig. ~~8~~9). Mature indigenous forests (i.e., pre-1990 natural forests) cover 29% of New Zealand, while planted exotic forests cover about 8% of the country (Ministry for the Environment, 2024). The area-based estimates of each forest flux suggest a net uptake of -0.9 kg CO_2 m^{-2} yr^{-1} for evergreen needleleaf forests, -0.3 kg CO_2 m^{-2} yr^{-1} for evergreen broadleaf forests and a significantly stronger uptake of -4 kg CO_2 m^{-2} yr^{-1} from the CenW pine fluxes (averaged for 2011-2020). Assuming that mature, indigenous forests can also take up CO_2 all year round, the large posterior sink in the South Island can be linked to high year-round productivity of these forests.

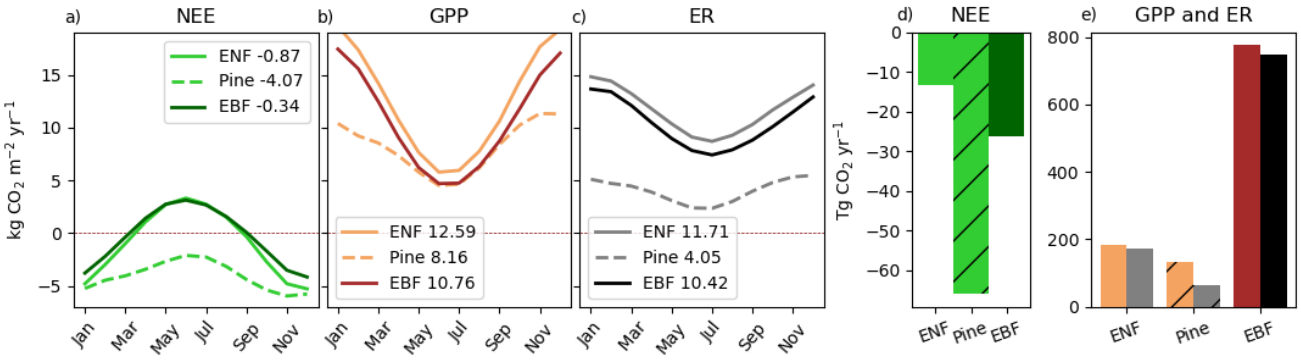

Figure 20. Net ecosystem exchange (NEE, a), gross primary production (GPP, b) and ecosystem respiration (ER, c) seasonal cycle (2011- 2020 average, annual net estimates are shown in the legend), as well mean 2011-2020 contribution (d and e) from the Biome-BGCMuSo evergreen broadleaf forest (EBF) and evergreen needleleaf forest (ENF) categories and CenW pine category. All values are based on the contributions of each forest type for the forested regions shown in Fig. ~~8a~~9a.

5.2 Bottom-up CO_2 flux estimates

We compare our CO_2 inversion posterior estimates with the current understanding derived from bottom-up estimates. This comparison is crucial as we recognize that there are significant discrepancies between the two approaches that require careful resolution. To address these differences, we compare our inversion estimates with published data on forests, grasslands, along with CO_2 lateral transport, with particular attention to the dynamics of fjord environments. By doing so, we aim to better reconcile the two methodologies and enhance the accuracy of both top-down and bottom-up CO_2 flux assessments.

Reconciling atmospheric observations with bottom-up flux estimates can be divided into two broad categories. The first is an imbalance of photosynthesis and respiration driving a net uptake into the land, in either forests or grasslands. The second is lateral transport of carbon through rivers, soil erosion and landslides. While the carbon export itself cannot be observed by the atmospheric inversion system, such carbon export can allow additional CO_2 uptake into soils, "renewing" the carbon pool within the soils. In the case of landslides, exposure of new surfaces results in development of new soils that can sequester carbon. Thus, carbon export should result in apparent net uptake or sink in the regional atmospheric inversion.

5.2.1 Forests

Forests can store and sequester large amounts of carbon; hence their management can play a crucial role in climate change mitigation (UNFCCC, 1997; Griscom et al., 2017; Kirschbaum et al., 2024). In contrast to younger forests, mature forests are generally considered to be carbon neutral and stop accumulating carbon once the trees reach a certain (species-dependent) age (Kira & Shidei, 1967; Odum, 1969; Sousa, 1984; Binkley et al., 2002; Holdaway et al., 2017). If mature

forests are perturbed, however, tree growth can be stimulated again and lead to renewed carbon accumulation (Van Tuyl et al., 2005; Luyssaert et al., 2008; Stephenson et al., 2014; Brienen et al., 2015; Schimel et al., 2015; Holdaway et al., 2017). Pest control can further allow forest recovery and increased growth in native forest; however, the impact of these practices on the carbon balance are not well quantified. It was shown that the CO_2 fertilisation effect can lead to carbon accumulation in young forests (Walker et al., 2019); however, its impact on mature forests is still being questioned (Jiang et al., 2020). Widely used models produce results which vary widely and depend on how models implement the relationship between photosynthesis and nitrogen limitation (Arora et al., 2020). Specific meteorological and growing conditions can further impact the CO_2 exchange from different ecosystems leading to changes in their photosynthetic or respiratory activity (Campbell et al., 2014; Duffy et al., 2021).

Current studies are still subject to uncertainties and debates with contradictory and complex conclusions in terms of the nature and magnitude of CO_2 exchange from different forest types (Carey et al., 2001; Pregitzer & Euskirchen, 2004; Bonan, 2008; Erb et al., 2013; Pugh et al., 2019). Carbon capture of newly-planted stands of native species suggest an upper limit of -0.95 to -1.5 kg CO_2 m^{-2} yr^{-1} (Kimberley et al., 2014; Holdaway et al., 2017) depending on the species of the trees (i.e., Red Beach, Puriri, Kauri, Totara) and as high as -3 kg CO_2 m^{-2} yr^{-1} in short-term for mixed shrubs. For secondary and mature forests, Holdaway et al. (2017) estimated gains of less than -0.5 kg CO_2 m^{-2} yr^{-1} for the first 40 years and subsequently at steady state. Paul et al. (2021) found that New Zealand's natural forests are in balance with sequestration rate of 0.2 kg CO_2 m^{-2} yr^{-1} for regenerating forests and close to zero for tall forest. The carbon gain from production forests (e.g., pine) can vary across the country from about -1.1 kg CO_2 m^{-2} yr^{-1} at the South Island West Coast to -3.5 kg CO_2 m^{-2} yr^{-1} in the Taranaki region (nationally average number of -1.9 kg CO_2 m^{-2} yr^{-1}) over about 30 years before felling. Our top-down estimates for the Fiordland inversion region (region 13), with 42% (Table S3) of the region being predominantly covered by mature native forests suggest an average flux of -1 ± 0.3 kg CO_2 m^{-2} yr^{-1}.

5.2.2 Grasslands

Grasslands contribute to carbon uptake through plant growth, which is mostly balanced by carbon loss through either plant decomposition or animal respiration. There is a slight surplus of carbon fixation to be balanced by methane flux and export of animal products as milk, meat or wool. There can be an additional gain or loss corresponding to changes in soil organic carbon (SOC). The carbon balance in forests is mainly driven by changes in woody biomass, for grasslands; however, the balance is primarily driven by changes in SOC or leaf biomass carbon (Kirschbaum et al., 2020). Previous studies have estimated dairy grasslands to be near carbon neutral, with net uptake during springtime, dependent on different management regimes (Kirschbaum et al., 2020; Wall et al., 2024). For a small set of sites, Schipper et al. (2014) found preliminary evidence for SOC gains in New Zealand pasture hill country of -0.26 kg CO_2 m^{-2} yr^{-1}, while flat land and tussocks (Schipper et al., 2017) were near to carbon neutral; however, they noted that these estimates are highly uncertain

due to poor data coverage. Pasture on drained peats acts as a source of 1.8 kg CO_2 m^{-2} yr^{-1} (mainly Waikato and Southland region, Campbell et al. (2021)) neither of which are evident in the inversion. Some land management practices also lead to losses of carbon, e.g., irrigation contributes to the source by 0.18 kg CO_2 m^{-2} yr^{-1} but only for the first ~10 years after irrigation commenced (Mudge et al., 2021). Further, dissolved organic carbon leaching in grasslands was estimated as a sink of -0.018 kg CO_2 m^{-2} yr^{-1} (Sparling et al., 2016); however, this leached carbon is likely partially mineralised to CO_2 during transport through vadose zone and in groundwater. It is assumed that 0.3 kg CO_2 m^{-2} yr^{-1} of the pasture milk solids in New Zealand is exported (estimated from milk production and carbon content of milk) while export of pasture meat and wool is estimated at 0.07 kg CO_2 m^{-2} yr^{-1}. Furthermore, assuming that New Zealand has ~4.8 million cows (DairyNZ, 2022) and that 50% of the carbon intake is being respired as CO_2 by dairy cows, we estimate the CO_2 emission from animal respiration to be ~17 Tg CO_2 yr^{-1} (~0.054 kg CO_2 m^{-2} yr^{-1}), and an additional ~12 Tg CO_2 yr^{-1} (~0.037 kg CO_2 m^{-2} yr^{-1}) from sheep and beef cattle. Top-down sink estimates of regions with predominantly grazed grassland were as high as -1.3 kg CO_2 m^{-2} y^{-1} using Southland as an example (Table S7).

5.2.3 Lateral transport and fjords

Lateral transport, erosion and deposition of organic material can be very important in montane regions and other steeplands when accompanied by rapid re-establishment of productive vegetation on the disturbed landscape (Stallard, 1998; Berhe et al., 2018). While the carbon export itself cannot be observed by the atmospheric inversion system, such carbon export can allow additional CO_2 uptake, "renewing" the long-lived carbon pools in soils and wood. In the case of landslides, exposure of new surfaces results in development of new soils that can sequester carbon. Thus, carbon export should result in apparent net uptake or sink in the regional atmospheric inversion.

Globally, about 8 Pg CO_2 yr^{-1} of carbon is exported through lateral transport, with about half of this being returned to the atmosphere from inland waters (Regnier et al., 2022; Tian et al., 2023). This return of carbon from inland waters will be included in the atmospheric inversion as a source within the same regions as the export occurs, and therefore can be ignored in this reconciliation. The remaining roughly 4 Pg CO_2 yr^{-1} is exported into coastal margins, as dissolved inorganic carbon (DIC, ~50%), dissolved organic carbon (DOC, ~30%) and particulate organic carbon (POC, ~ 20%). It is thought that about half of this carbon is sequestered into sediment over the long-term, with the remainder being returned to the atmosphere in the coastal margins or open ocean (Regnier et al., 2022; Tian et al., 2023); this return to the atmosphere will occur outside of the regional inversion footprint, and thus will appear as a sink and is not further considered here.

New Zealand's long coastline relative to land area, dramatic topography, high rainfall, tectonic activity and changing land uses all contribute to proportionately large sediment export, contributing about 1.7% of global sediment export (Hicks et al., 2011). Three studies have estimated New Zealand's carbon export at 15-19 Tg CO_2 yr^{-1}, each with different partitioning of the carbon between POC, DOC and DIC (Scott et al., 2006; Dymond, 2010; Villalobos et al., 2023),

with more details in Sect. S5~~6~~. The South Island West Coast and Fiordland contribute about 65% of this carbon export (Scott et al., 2006). These studies all rely on modelling and scaling up of a modest number of observations, and do not always consider all three carbon pools, indicating that more research is needed to better constrain the magnitude of carbon export from New Zealand.

We have identified a range of carbon exchange processes in mature and production forests, grasslands, fjord environments, as well as the role of lateral transport that could contribute to the differences. Lateral transport of carbon could explain about half of the observed atmospheric inversion sink. Forest and grassland carbon imbalances could plausibly explain the remainder of the difference between top-down and bottom-up, especially when forest disturbance and pest control are considered.

6. New Zealand's Greenhouse Gas Inventory

Estimates of greenhouse gas emissions and uptake from both the Inventory and top-down methods are subject to discrepancies and uncertainties (Baker et al., 2006; Göckede et al., 2010; Peylin et al., 2011; Saeki & Patra, 2017; Kountouris et al., 2018; Philip et al., 2019; Bastos et al., 2020). Closing the gap between inventory and top-down methods, and the need for the inclusion and improvement of top-down approaches for estimating carbon fluxes is recognised globally as a pivotal task for future development (IPCC, 2019).

In New Zealand's 2024 Inventory, compiled by the Ministry for the Environment (MfE), the net carbon uptake estimates from the land-use and forestry sector are based on land-use maps, providing activity data to which emission factors are applied to estimate carbon fluxes. Forest carbon fluxes are modelled, based on measurements from a representative network of forest plots that are scaled up to the national scale (Ministry for the Environment, 2024). National greenhouse gas inventories are focussed on anthropogenic change, rather than capturing all carbon fluxes as is the case for inverse modelling. However, in New Zealand, all land and forests meet the IPCC definition of managed land (Ministry for the Environment, 2024), leading to an easier comparison between methods.

The 2024 Inventory estimated New Zealand's gross CO_2 emissions from all sectors excluding land use, land-use change and forestry for 2011-2020 to be 34 - 37 Tg CO_2 yr^{-1} (Ministry for the Environment, 2024). The land use, land-use change and forestry (LULUCF, includes forest land, harvested wood products, cropland, grassland, wetlands, settlements and other land) sector was reported as an overall sink over this period, removing about 21 ± 14 - 29 ± 19 Tg CO_2 yr^{-1} from the atmosphere. The largest fluxes were observed in forests (pre-1990 natural and planted forests, post-1989 natural and planted forests), estimated to be a net sink of around 18 ± 12 Tg CO_2 yr^{-1} in 2022, made up of 64 Tg CO_2 yr^{-1} in removals offset by 46 Tg CO_2 yr^{-1} in emissions (99% of which is from harvest), followed by a net gain in harvested wood products (of 7 Tg CO_2 yr^{-1}). Grasslands, croplands and other land areas were estimated as a net source adding around 5 Tg CO_2 yr^{-1}.

Our results have diverged further from the Inventory estimates than the earlier findings reported in Steinkamp et al. (2017). The inversion suggests a net -171 ± 29 Tg CO_2 yr^{-1} uptake from New Zealand's terrestrial biosphere; however, these results are not directly comparable with the Inventory (-24 Tg CO_2 yr^{-1}) due to differences between what the inventory reports and what is captured by atmospheric measurements used in the inverse model~~the atmospheric measurements that underpin the inverse model detect~~. From the 46 Tg CO_2 yr^{-1} forestry emissions, 30% is debris that decays away on site which is transferred to the deadwood pool while 70% exported off site and processed. Assuming that 70% of emissions occur outside of New Zealand, the net sink of forests would be estimated to be 55 Tg CO_2 yr^{-1}, instead of 18 Tg CO_2 yr^{-1}, which would partially close the gap. Further differences can be explained by the regional variation in age class profiles that impact sequestration rates in production forestry, export of harvested wood from the site and the decay of harvested wood products, variance in the timing of the decay of harvest residues on site following tree harvest and natural mortality, agricultural exports, animal respiration, and assumptions that the above or below-ground grassland biomass is in steady state when in a grazing regime and that mineral soil carbon stocks are in steady state 20 years following a land use change as only the land use change impact on soil carbon is estimated in the inventory.

These differences may contribute further towards explaining the divergent results observed in this study. If a sink of this magnitude is occurring in mature natural forests, it should be reflected in the biomass and detected in the national forest plot monitoring programme, hence the results from the third tranche (Paul et al., 2021) of measurements in natural forests will provide a further useful step towards understanding where the observed sink is occurring.

7 Conclusion

Top-down regional and national scale estimates can provide crucial information to improve inventory and bottom-up methods and can help in identifying measurement limitations. We use inverse modelling to estimate New Zealand's carbon uptake and emissions using atmospheric measurements and model. This effort is part of the CarbonWatch-NZ research programme, which aims to develop a complete top-down picture of New Zealand's carbon balance using national inverse modelling and targeted studies of New Zealand's forest, grassland and urban environments to support climate mitigation. Our work here focuses on significant updates of a previously published atmospheric inverse modelling framework (Steinkamp et al., 2017) to constrain surface-atmosphere net CO_2 fluxes on a national scale.

Our decade-long (2011-2020) inverse modelling results point to a persistent national scale CO_2 net uptake across all New Zealand of -171 ± 29 Tg CO_2 yr^{-1}. Our estimates suggest a stronger national scale sink relative to both prior bottom-up and the independent Inventory estimates. We also find a stronger national scale uptake relative to Steinkamp et al. (2017), primarily driven by an increased uptake in the prior flux estimates from regions covered by plantation forests in the North Island. However, we observe that our measurement network is less sensitive to the northern region of the North Island, than

to the other regions across New Zealand. As a result, incorporating measurements from additional sites into our inversion system could reveal stronger sink or source regions, particularly if there are biases in the prior flux assumptions.

We observe larger differences relative to prior bottom-up estimates in the South Island, with additional carbon uptake in regions along the north-west and southern parts of the South Island, including the West Coast region, Fiordland and Southland (~53% of the national sink). Relative to Steinkamp et al. (2017) the sink in the South Island is more spread out between different regions. Southland is a grazed pasture region (~70% sheep and beef pasture) while large part of the West Coast and Fiordland regions is covered by mature indigenous forests (~50%), suggesting that these environments can potentially take up more carbon than thought before; however, the inversion estimates cannot be explained by current understanding of these mature forests. We conducted sensitivity tests and inversion diagnostics to evaluate potential biases in our top-down estimates. The magnitude of the estimated CO_2 sink is moderately sensitive to modelling assumptions, specifically the choice of the prior terrestrial fluxes and modelling of the CO_2 diurnal cycle; however, across a wide range of sensitivity tests we still find a stronger sink relative to bottom-up estimates.

Our inversion system can estimate the net air–sea and air–land fluxes; however, it cannot identify the specific processes driving the posterior fluxes. Relative to the prior bottom-up estimates, our results suggest that the stronger annual net CO_2 sink is impacted by suppressed autumn/winter respiration. The year-round CO_2 uptake by indigenous forests could explain a portion of the stronger sink in our posterior estimates. Further differences between the prior and posterior estimates can be driven by a combination of other carbon exchange processes such as: native forest regeneration after forest disturbance or pest control, changes in soil carbon and soil carbon recovery, lateral transport and carbon sequestration due to erosion, deposition, burial due to strong tectonic activity and frequent landslides in some regions, marine productivity in the fjords and discharge of freshwater out of the fjords that export carbon from the Fiordland region to the open ocean and other regions.

While we have identified a number of CO_2 exchange processes that could be at play, we cannot explain the difference between top-down, bottom-up and inventory estimates. The best estimate of any individual process is not enough to explain the sink we see in our inversion; however, we acknowledge that uncertainties for some estimates can be large. Region specific studies are required to identify if the observed CO_2 uptake is a permanent sink, as carbon transported laterally may be returned to the atmosphere, and additional work is needed to resolve the remaining differences between atmospheric measurements, terrestrial biosphere models, and the Inventory.

Data availability. The model code, input and output data has been made publicly available on Zenodo (https://doi.org/10.5281/zenodo.14306816).

Supplement. The supplement related to this article is available online.

Author contributions. BB ran the inversion code, performed the analysis, and led the writing of the paper under the supervision and guidance of SMF. The observational data set was prepared by GB, DS, RM and SN. The TF5 ship measurements were provided by HM and SN. The prior Biome-BGCMuSo fluxes were provided by EDK, with support from DH and ZB. CenW fluxes were provided by DLG, MUFK and LL. NAME III simulations were performed with guidance from SM. WTB and JT contributed to the comparison of the inversion results to bottom-up estimates, while AB contributed to the comparison with the Inventory. AG and DK provided input on the analysis of the inversion results. All authors contributed to editing and revising the paper.

Competing interests. The authors declare that they have no conflict of interest.

Acknowledgements. The work presented here is part of the CarbonWatch-NZ project focusing on New Zealand's carbon balance and carbon exchange processes. The authors are grateful to the CarbonWatch-NZ and NIWA Tropac and Lauder research teams. We would like to acknowledge the funding schemes for supporting this research including MBIE and the NIWA core funding through the Greenhouse Gases, Emissions and Carbon Cycle Science Programme. ZB and DH were funded by the ~~Hungary~~ National Multidisciplinary Laboratory for Climate Change~~,~~ (RRF-2.3.1-21-2022-00014) project within the framework of Hungary's National Recovery and Resilience Plan supported by the Recovery and Resilience Facility of the European Union. We acknowledge NIWA and Raghav Srinivasan for providing the VCSN data for the Biome-BGCMuSo and CenW model. The author(s) wish to acknowledge the use of New Zealand eScience Infrastructure (NeSI) high performance computing facilities, consulting support and/or training services as part of this research. New Zealand's national facilities are provided by NeSI and funded jointly by NeSI's collaborator institutions and through the Ministry of Business, Innovation & Employment's Research Infrastructure programme. URL https://www.nesi.org.nz. We deeply appreciate the generous cooperation of Toyofuji Shipping Co., and Kagoshima Senpaku Co. with the NIES VOS program and would like to thank the captain and crew of Trans Future 5. The atmospheric CO_2 data measured onboard Trans Future 5 are available on the website https://soop.jp. We thank Scott Graham from Manaaki Whenua - Landcare Research for contributing with eddy covariance data and John Hunt from Manaaki Whenua - Landcare Research for helpful discussions and contribution about bottom-up CO_2 estimates and processes. We thank Peter Landschützer for consulting about the prior ocean fluxes. CarbonTracker CT2022 results were provided by NOAA GML, Boulder, Colorado, USA from the website at http://carbontracker.noaa.gov. EDGARv7.0 was obtained from https://edgar.jrc.ec.europa.eu/dataset_ghg70. The New Zealand Material was also produced using Met Office Software. Lauder radiosonde data was provided by Ben Liley. We thank colleagues from New Zealand's Ministry for the Environment (MfE), for their input about the National Inventory.

References

Arora, V. K., Katavouta, A., Williams, R. G., Jones, C. D., Brovkin, V., Friedlingstein, P., Schwinger, J., Bopp, L., Boucher, O., Cadule, P., Chamberlain, M. A., Christian, J. R., Delire, C., Fisher, R. A., Hajima, T., Ilyina, T., Joetzjer, E., Kawamiya, M., Koven, C. D., Krasting, J. P., Law, R. M., Lawrence, D. M., Lenton, A., Lindsay, K., Pongratz, J., Raddatz, T., Séférian, R., Tachiiri, K., Tjiputra, J. F., Wiltshire, A., Wu, T., & Ziehn, T. (2020). Carbon–concentration and carbon–climate feedbacks in CMIP6 models and their comparison to CMIP5 models. *Biogeosciences*, *17*(16), 4173-4222. https://doi.org/10.5194/bg-17-4173-2020

Baker, D. F., Law, R. M., Gurney, K. R., Rayner, P., Peylin, P., Denning, A. S., Bousquet, P., Bruhwiler, L., Chen, Y.-H., Ciais, P., Fung, I. Y., Heimann, M., John, J., Maki, T., Maksyutov, S., Masarie, K., Prather, M., Pak, B., Taguchi, S., & Zhu, Z. (2006). TransCom 3 inversion intercomparison: Impact of transport model errors on the interannual variability of regional CO2 fluxes, 1988–2003. *Global Biogeochemical Cycles*, *20*(1). https://doi.org/10.1029/2004GB002439

Bastos, A., O'Sullivan, M., Ciais, P., Makowski, D., Sitch, S., Friedlingstein, P., Chevallier, F., Rödenbeck, C., Pongratz, J., Luijkx, I. T., Patra, P. K., Peylin, P., Canadell, J. G., Lauerwald, R., Li, W., Smith, N. E., Peters, W., Goll, D. S., Jain, A. K., Kato, E., Lienert, S., Lombardozzi, D. L., Haverd, V., Nabel, J. E. M. S., Poulter, B., Tian, H., Walker, A. P., & Zaehle, S. (2020). Sources of Uncertainty in Regional and Global Terrestrial CO2 Exchange Estimates. *Global Biogeochemical Cycles*, *34*(2), e2019GB006393. https://doi.org/10.1029/2019GB006393

Berchet, A., Pison, I., Chevallier, F., Bousquet, P., Conil, S., Geever, M., Laurila, T., Lavrič, J., Lopez, M., Moncrieff, J., Necki, J., Ramonet, M., Schmidt, M., Steinbacher, M., & Tarniewicz, J. (2013). Towards better error statistics for atmospheric inversions of methane surface fluxes. *Atmos. Chem. Phys.*, *13*(14), 7115-7132. https://doi.org/10.5194/acp-13-7115-2013

Bergamaschi, P., Krol, M., Dentener, F., Vermeulen, A., Meinhardt, F., Graul, R., Ramonet, M., Peters, W., & Dlugokencky, E. J. (2005). Inverse modelling of national and European CH4 emissions using the atmospheric zoom model TM5. *Atmos. Chem. Phys.*, *5*(9), 2431-2460. https://doi.org/10.5194/acp-5-2431-2005

Berhe, A. A., Barnes, R. T., Six, J., & Marín-Spiotta, E. (2018). Role of Soil Erosion in Biogeochemical Cycling of Essential Elements: Carbon, Nitrogen, and Phosphorus. *Annual Review of Earth and Planetary Sciences*, *46*(Volume 46, 2018), 521-548. https://doi.org/10.1146/annurev-earth-082517-010018

Binkley, D., Stape, J. L., Ryan, M. G., Barnard, H. R., & Fownes, J. (2002). Age-related Decline in Forest Ecosystem Growth: An Individual-Tree, Stand-Structure Hypothesis. *Ecosystems*, *5*(1), 58-67. https://doi.org/10.1007/s10021-001-0055-7

Bonan, G. B. (2008). Forests and Climate Change: Forcings, Feedbacks, and the Climate Benefits of Forests. *Science*, *320*(5882), 1444-1449. https://doi.org/doi:10.1126/science.1155121

Brailsford, G. W., Stephens, B. B., Gomez, A. J., Riedel, K., Mikaloff Fletcher, S. E., Nichol, S. E., & Manning, M. R. (2012). Long-term continuous atmospheric CO2 measurements at Baring Head, New Zealand. *Atmos. Meas. Tech.*, *5*(12), 3109-3117. https://doi.org/10.5194/amt-5-3109-2012

Brienen, R. J. W., Phillips, O. L., Feldpausch, T. R., Gloor, E., Baker, T. R., Lloyd, J., Lopez-Gonzalez, G., Monteagudo-Mendoza, A., Malhi, Y., Lewis, S. L., Vásquez Martinez, R., Alexiades, M., Álvarez Dávila, E., Alvarez-Loayza, P., Andrade, A., Aragão, L. E. O. C., Araujo-Murakami, A., Arets, E. J. M. M., Arroyo, L., Aymard C, G. A., Bánki, O. S., Baraloto, C., Barroso, J., Bonal, D., Boot, R. G. A., Camargo, J. L. C., Castilho, C. V., Chama, V., Chao, K. J., Chave, J., Comiskey, J. A., Cornejo Valverde, F., da Costa, L., de Oliveira, E. A., Di Fiore, A., Erwin, T. L., Fauset, S., Forsthofer, M., Galbraith, D. R., Grahame, E. S., Groot, N., Hérault, B., Higuchi, N., Honorio Coronado, E. N., Keeling, H., Killeen, T. J., Laurance, W. F., Laurance, S., Licona, J., Magnussen, W. E., Marimon, B. S., Marimon-Junior, B. H., Mendoza, C., Neill, D. A., Nogueira, E. M., Núñez, P., Pallqui Camacho, N. C., Parada, A., Pardo-Molina, G., Peacock, J., Peña-Claros, M., Pickavance, G. C., Pitman, N. C. A., Poorter, L., Prieto, A., Quesada, C. A., Ramírez, F., Ramírez-Angulo, H., Restrepo, Z., Roopsind, A., Rudas, A., Salomão, R. P., Schwarz, M., Silva, N., Silva-Espejo, J. E., Silveira, M., Stropp, J., Talbot, J., ter Steege, H., Teran-Aguilar, J., Terborgh, J., Thomas-Caesar, R., Toledo, M., Torello-Raventos, M., Umetsu, R. K., van der Heijden, G. M. F., van der Hout, P., Guimarães Vieira, I. C., Vieira, S. A., Vilanova, E., Vos, V. A., & Zagt, R. J. (2015). Long-term decline of the Amazon carbon sink. *Nature*, *519*(7543), 344-348. https://doi.org/10.1038/nature14283

Bukosa, B., Fisher, J. A., Deutscher, N. M., & Jones, D. B. A. (2023). A Coupled CH4, CO and CO2 Simulation for Improved Chemical Source Modeling. *Atmosphere*, *14*(5), 764. https://www.mdpi.com/2073-4433/14/5/764

Byrne, B., Baker, D. F., Basu, S., Bertolacci, M., Bowman, K. W., Carroll, D., Chatterjee, A., Chevallier, F., Ciais, P., Cressie, N., Crisp, D., Crowell, S., Deng, F., Deng, Z., Deutscher, N. M., Dubey, M. K., Feng, S., García, O. E., Griffith, D. W. T., Herkommer, B., Hu, L., Jacobson, A. R., Janardanan, R., Jeong, S., Johnson, M. S., Jones, D. B. A., Kivi, R., Liu, J., Liu, Z., Maksyutov, S., Miller, J. B., Miller, S. M., Morino, I., Notholt, J., Oda, T., O'Dell, C. W., Oh, Y. S., Ohyama, H., Patra, P. K., Peiro, H., Petri, C., Philip, S., Pollard, D. F., Poulter, B., Remaud, M., Schuh, A., Sha, M. K., Shiomi, K., Strong, K., Sweeney, C., Té, Y., Tian, H., Velazco, V. A., Vrekoussis, M., Warneke, T., Worden, J. R., Wunch, D., Yao, Y., Yun, J., Zammit-Mangion, A., & Zeng, N. (2023). National CO2 budgets (2015–2020) inferred from atmospheric CO2 observations in support of the global stocktake. *Earth Syst. Sci. Data*, *15*(2), 963-1004. https://doi.org/10.5194/essd-15-963-2023

Campbell, D. I., Glover-Clark, G. L., Goodrich, J. P., Morcom, C. P., Schipper, L. A., & Wall, A. M. (2021). Large differences in CO2 emissions from two dairy farms on a drained peatland driven by contrasting respiration rates during seasonal dry conditions. *Science of the Total Environment*, *760*, 143410. https://doi.org/10.1016/j.scitotenv.2020.143410

Campbell, D. I., Smith, J., Goodrich, J. P., Wall, A. M., & Schipper, L. A. (2014). Year-round growing conditions explains large CO2 sink strength in a New Zealand raised peat bog. *Agricultural and Forest Meteorology*, *192-193*, 59-68. https://doi.org/10.1016/j.agrformet.2014.03.003

Carey, E. V., Sala, A., Keane, R., & Callaway, R. M. (2001). Are old forests underestimated as global carbon sinks? *Global Change Biology*, *7*(4), 339-344. https://doi.org/10.1046/j.1365-2486.2001.00418.x

Cichota, R., O., S. V., & and Tait, A. B. (2008). A functional evaluation of virtual climate station rainfall data. *New Zealand Journal of Agricultural Research*, *51*(3), 317-329. https://doi.org/10.1080/00288230809510463

Crippa, M., Guizzardi, D., Banja, M., Solazzo, E., Muntean, M., Schaaf, E., Pagani, F., Monforti-Ferrario, F., Olivier, J., Quadrelli, R., Risquez Martin, A., Taghavi-Moharamli, P., Grassi, G., Rossi, S., Jacome Felix Oom, D., Branco, A., San-Miguel-Ayanz, J., & Vignati, E. (2022). CO2 emissions of all world countries. *EUR 31182 EN, Publications Office of the European Union, Luxembourg*, *ISBN: 978-92-76-55802-6, JRC130363*. https://doi.org/10.2760/07904

DairyNZ. (2022). New Zealand Dairy Statistics 2021-22. In.

Davies, T., Cullen, M. J. P., Malcolm, A. J., Mawson, M. H., Staniforth, A., White, A. A., & Wood, N. (2005). A new dynamical core for the Met Office's global and regional modelling of the atmosphere. *Quarterly Journal of the Royal Meteorological Society*, *131*(608), 1759-1782. https://doi.org/10.1256/qj.04.101

Deng, Z., Ciais, P., Tzompa-Sosa, Z. A., Saunois, M., Qiu, C., Tan, C., Sun, T., Ke, P., Cui, Y., Tanaka, K., Lin, X., Thompson, R. L., Tian, H., Yao, Y., Huang, Y., Lauerwald, R., Jain, A. K., Xu, X., Bastos, A., Sitch, S., Palmer, P. I., Lauvaux, T., d'Aspremont, A., Giron, C., Benoit, A., Poulter, B., Chang, J., Petrescu, A. M. R., Davis, S. J., Liu, Z., Grassi, G., Albergel, C., Tubiello, F. N., Perugini, L., Peters, W., & Chevallier, F. (2022). Comparing national greenhouse gas budgets reported in UNFCCC inventories against atmospheric inversions. *Earth Syst. Sci. Data*, *14*(4), 1639-1675. https://doi.org/10.5194/essd-14-1639-2022

Duffy, K. A., Schwalm, C. R., Arcus, V. L., Koch, G. W., Liang, L. L., & Schipper, L. A. (2021). How close are we to the temperature tipping point of the terrestrial biosphere? *Science Advances*, *7*(3), eaay1052. https://doi.org/doi:10.1126/sciadv.aay1052

Dymond, J. R. (2010). Soil erosion in New Zealand is a net sink of CO2. *Earth Surface Processes and Landforms*, *35*(15), 1763-1772. https://doi.org/10.1002/esp.2014

Enting, I. G. (2002). *Inverse Problems in Atmospheric Constituent Transport*. Cambridge University Press. https://doi.org/DOI: 10.1017/CBO9780511535741

Erb, K.-H., Kastner, T., Luyssaert, S., Houghton, R. A., Kuemmerle, T., Olofsson, P., & Haberl, H. (2013). Bias in the attribution of forest carbon sinks. *Nature Climate Change*, *3*(10), 854-856. https://doi.org/10.1038/nclimate2004

Ganesan, A. L., Manning, A. J., Grant, A., Young, D., Oram, D. E., Sturges, W. T., Moncrieff, J. B., & O'Doherty, S. (2015). Quantifying methane and nitrous oxide emissions from the UK and Ireland using a national-scale monitoring network. *Atmos. Chem. Phys.*, *15*(11), 6393-6406. https://doi.org/10.5194/acp-15-6393-2015

Gerbig, C., Lin, J. C., Wofsy, S. C., Daube, B. C., Andrews, A. E., Stephens, B. B., Bakwin, P. S., & Grainger, C. A. (2003). Toward constraining regional-scale fluxes of CO2 with atmospheric observations over a continent: 2. Analysis of COBRA data using a receptor-oriented framework. *Journal of Geophysical Research: Atmospheres*, *108*(D24). https://doi.org/10.1029/2003JD003770

Göckede, M., Turner, D. P., Michalak, A. M., Vickers, D., & Law, B. E. (2010). Sensitivity of a subregional scale atmospheric inverse CO2 modeling framework to boundary conditions. *Journal of Geophysical Research: Atmospheres*, *115*(D24). https://doi.org/10.1029/2010JD014443

Griscom, B. W., Adams, J., Ellis, P. W., Houghton, R. A., Lomax, G., Miteva, D. A., Schlesinger, W. H., Shoch, D., Siikamäki, J. V., Smith, P., Woodbury, P., Zganjar, C., Blackman, A., Campari, J., Conant, R. T., Delgado, C., Elias, P., Gopalakrishna, T., Hamsik, M. R., Herrero, M., Kiesecker, J., Landis, E., Laestadius, L., Leavitt, S. M., Minnemeyer, S., Polasky, S., Potapov, P., Putz, F. E., Sanderman, J., Silvius, M., Wollenberg, E., & Fargione, J. (2017). Natural climate solutions. *Proceedings of the National Academy of Sciences*, *114*(44), 11645-11650. https://doi.org/doi:10.1073/pnas.1710465114

Gurney, K. R., Law, R. M., Denning, A. S., Rayner, P. J., Pak, B. C., Baker, D., Bousquet, P., Bruhwiler, L., Chen, Y.-H., Ciais, P., Fung, I. Y., Heimann, M., John, J., Maki, T., Maksyutov, S., Peylin, P., Prather, M., & Taguchi, S. (2004). Transcom 3 inversion intercomparison: Model mean results for the estimation of seasonal carbon sources and sinks. *Global Biogeochemical Cycles*, *18*(1). https://doi.org/10.1029/2003GB002111

Henne, S., Brunner, D., Oney, B., Leuenberger, M., Eugster, W., Bamberger, I., Meinhardt, F., Steinbacher, M., & Emmenegger, L. (2016). Validation of the Swiss methane emission inventory by atmospheric observations and inverse modelling. *Atmos. Chem. Phys.*, *16*(6), 3683-3710. https://doi.org/10.5194/acp-16-3683-2016

Hicks, D. M., Shankar, U., McKerchar, A. I., Basher, L., Lynn, I., Page, M., & Jessen, M. (2011). Suspended sediment yields from New Zealand rivers. *Journal of Hydrology (New Zealand)*, *50*(1), 81-142.

Hidy, D., Barcza, Z., Hollós, R., Dobor, L., Ács, T., Zacháry, D., Filep, T., Pásztor, L., Incze, D., Dencső, M., Tóth, E., Merganičová, K., Thornton, P., Running, S., & Fodor, N. (2022). Soil-related developments of the Biome-BGCMuSo v6.2 terrestrial ecosystem model. *Geosci. Model Dev.*, *15*(5), 2157-2181. https://doi.org/10.5194/gmd-15-2157-2022

Hidy, D., Barcza, Z., Marjanović, H., Ostrogović Sever, M. Z., Dobor, L., Gelybó, G., Fodor, N., Pintér, K., Churkina, G., Running, S., Thornton, P., Bellocchi, G., Haszpra, L., Horváth, F., Suyker, A., & Nagy, Z. (2016). Terrestrial ecosystem process model Biome-BGCMuSo v4.0: summary of improvements and new modeling possibilities. *Geosci. Model Dev.*, *9*(12), 4405-4437. https://doi.org/10.5194/gmd-9-4405-2016

Holdaway, R. J., Easdale, T. A., Carswell, F. E., Richardson, S. J., Peltzer, D. A., Mason, N. W. H., Brandon, A. M., & Coomes, D. A. (2017). Nationally Representative Plot Network Reveals Contrasting Drivers of Net Biomass Change in Secondary and Old-Growth Forests. *Ecosystems*, *20*(5), 944-959. https://doi.org/10.1007/s10021-016-0084-x

IPCC. (2006). 2006 IPCC Guidelines for National Greenhouse Gas Inventories. In: Prepared by the National Greenhouse Gas Inventories Programme, Eggleston H.S., Buendia L., Miwa K., Ngara T. and Tanabe K. (eds). Published: IGES, Japan

IPCC. (2019). 2019 Refinement to the 2006 IPCC Guidelines for National Greenhouse Gas Inventories. In: Calvo Buendia, E., Tanabe, K., Kranjc, A., Baasansuren, J., Fukuda, M., Ngarize, S., Osako, A., Pyrozhenko, Y., Shermanau, P. and Federici, S. (eds). Published: IPCC, Switzerland.

Jacobson, A. R., Schuldt, K. N., Tans, P., Arlyn, A., Miller, J. B., Oda, T., Mund, J., Weir, B., Ott, L., Aalto, T., Abshire, J. B., Aikin, K., Aoki, S., Apadula, F., Arnold, S., Baier, B., Bartyzel, J., Beyersdorf, A., Biermann, T., Biraud, S. C., Boenisch, H., Brailsford, G., Brand, W. A., Chen, G., Huilin, C., Lukasz, C., Clark, S., Colomb, A., Commane, R., Conil, S., Couret, C., Cox, A., Cristofanelli, P., Cuevas, E., Curcoll, R., Daube, B., Davis, K. J., De Wekker, S., Coletta, J. D., Delmotte, M., DiGangi, E., DiGangi, J. P., Di Sarra, A. G., Dlugokencky, E., Elkins, J. W., Emmenegger, L., Shuangxi, F., Fischer, M. L., Forster, G., Frumau, A., Galkowski, M., Gatti, L. V., Gehrlein, T., Gerbig, C., Francois, G., Gloor, E., Gomez-Trueba, V., Goto, D., Griffis, T., Hammer, S., Hanson, C., Haszpra, L., Hatakka, J., Heimann, M., Heliasz, M., Hensen, A., Hermansen, O., Hintsa, E., Holst, J., Ivakhov, V., Jaffe, D. A., Jordan, A., Joubert, W., Karion, A., Kawa, S. R., Kazan, V., Keeling, R. F., Keronen, P., Kneuer, T., Kolari, P., Kateřina, K., Kort, E., Kozlova, E., Krummel, P., Kubistin, D., Labuschagne, C., Lam, D. H. Y., Lan, X., Langenfelds, R. L., Laurent, O., Laurila, T., Lauvaux, T., Lavric, J., Law, B. E., Lee, J., Lee, O. S. M., Lehner, I., Lehtinen, K., Leppert, R., Leskinen, A., Leuenberger, M., Levin, I., Levula, J., Lin, J., Lindauer, M., Loh, Z., Lopez, M., Luijkx, I. T., Lunder, C. R., Machida, T., Mammarella, I., Manca, G., Manning, A., Manning, A., Marek, M. V., Martin, M. Y., Matsueda, H., McKain, K., Meijer, H., Meinhardt, F., Merchant, L., Mihalopoulos, N., Miles, N. L.,

Miller, C. E., Mitchell, L., Mölder, M., Montzka, S., Moore, F., Moossen, H., Morgan, E., Josep-Anton, M., Morimoto, S., Müller-Williams, J., Munger, J. W., Munro, D., Myhre, C. L., Shin-Ichiro, N., Jaroslaw, N., Newman, S., Nichol, S., Niwa, Y., Obersteiner, F., O'Doherty, S., Paplawsky, B., Peischl, J., Peltola, O., Piacentino, S., Jean-Marc, P., Pickers, P., Piper, S., Pitt, J., Plass-Dülmer, C., Platt, S. M., Prinzivalli, S., Ramonet, M., Ramos, R., Reyes-Sanchez, E., Richardson, S. J., Riris, H., Rivas, P. P., Ryerson, T., Saito, K., Sargent, M., Sasakawa, M., Scheeren, B., Schuck, T., Schumacher, M., Seifert, T., Sha, M. K., Shepson, P., Shook, M., Sloop, C. D., Smith, P., Stanley, K., Steinbacher, M., Stephens, B., Sweeney, C., Thoning, K., Timas, H., Torn, M., Tørseth, K., Trisolino, P., Turnbull, J., Van Den Bulk, P., Van Dinther, D., Vermeulen, A., Viner, B., Vitkova, G., Walker, S., Watson, A., Wofsy, S. C., Worsey, J., Worthy, D., Dickon, Y., Zaehle, S., Zahn, A., & Miroslaw, Z. (2023). CarbonTracker CT2022. In: NOAA Global Monitoring Laboratory.

Jiang, M., Medlyn, B. E., Drake, J. E., Duursma, R. A., Anderson, I. C., Barton, C. V. M., Boer, M. M., Carrillo, Y., Castañeda-Gómez, L., Collins, L., Crous, K. Y., De Kauwe, M. G., dos Santos, B. M., Emmerson, K. M., Facey, S. L., Gherlenda, A. N., Gimeno, T. E., Hasegawa, S., Johnson, S. N., Kännaste, A., Macdonald, C. A., Mahmud, K., Moore, B. D., Nazaries, L., Neilson, E. H. J., Nielsen, U. N., Niinemets, Ü., Noh, N. J., Ochoa-Hueso, R., Pathare, V. S., Pendall, E., Pihlblad, J., Piñeiro, J., Powell, J. R., Power, S. A., Reich, P. B., Renchon, A. A., Riegler, M., Rinnan, R., Rymer, P. D., Salomón, R. L., Singh, B. K., Smith, B., Tjoelker, M. G., Walker, J. K. M., Wujeska-Klause, A., Yang, J., Zaehle, S., & Ellsworth, D. S. (2020). The fate of carbon in a mature forest under carbon dioxide enrichment. *Nature*, *580*(7802), 227-231. https://doi.org/10.1038/s41586-020-2128-9

Jones, A. R., Thomson, D. J., Hort, M., & Devenish, B. (2007). The U.K. Met Office's next-generation atmospheric dispersion model, NAME III. *Borrego C. and Norman A.-L. (Eds) Air Pollution Modeling and its Application XVII (Proceedings of the 27th NATO/CCMS International Technical Meeting on Air Pollution Modelling and its Application), Boston, MA*, 580-589. https://doi.org/10.1007/978-0-387-68854-1_62

Kaminski, T., Rayner, P. J., Heimann, M., & Enting, I. G. (2001). On aggregation errors in atmospheric transport inversions. *Journal of Geophysical Research: Atmospheres*, *106*(D5), 4703-4715. https://doi.org/10.1029/2000JD900581

Keller, E., Lieffering, M., Guo, J., Baisden, W. T., & Ausseil, A.-G. (2021). Climatic factors influencing New Zealand pasture resilience under scenarios of future climate change. *NZGA: Research and Practice Series*, *17*, 105-122. https://doi.org/10.33584/rps.17.2021.3458

Keller, E. D., Baisden, W. T., Timar, L., Mullan, B., & Clark, A. (2014). Grassland production under global change scenarios for New Zealand pastoral agriculture. *Geosci. Model Dev.*, *7*(5), 2359-2391. https://doi.org/10.5194/gmd-7-2359-2014

Kimberley, M., Bergin, D., & Beets, P. (2014). Carbon sequestration by planted native trees and shrubs. *Planting and managing native trees: Technical handbook*, *10.5*.

Kira, T., & Shidei, T. (1967). Primary production and turnover of organic matter in different forest ecosystems of the western Pacific. *Japanese Journal of Ecology*, *17*(2), 70–87.

Kirschbaum, M. U. F. (1999). CenW, a forest growth model with linked carbon, energy, nutrient and water cycles. *Ecological Modelling*, *118*(1), 17-59. https://doi.org/10.1016/S0304-3800(99)00020-4

Kirschbaum, M. U. F., Cowie, A. L., Peñuelas, J., Smith, P., Conant, R. T., Sage, R. F., Brandão, M., Cotrufo, M. F., Luo, Y., Way, D. A., & Robinson, S. A. (2024). Is tree planting an effective strategy for climate change mitigation? *Science of the Total Environment*, *909*, 168479. https://doi.org/10.1016/j.scitotenv.2023.168479

Kirschbaum, M. U. F., Puche, N. J. B., Giltrap, D. L., Liáng, L. L., & Chabbi, A. (2020). Combining eddy covariance measurements with process-based modelling to enhance understanding of carbon exchange rates of dairy pastures. *Science of the Total Environment*, *745*, 140917. https://doi.org/10.1016/j.scitotenv.2020.140917

Kirschbaum, M. U. F., & Watt, M. S. (2011). Use of a process-based model to describe spatial variation in Pinus radiata productivity in New Zealand. *Forest Ecology and Management*, *262*(6), 1008-1019. https://doi.org/10.1016/j.foreco.2011.05.036

Kou, X., Peng, Z., Zhang, M., Hu, F., Han, X., Li, Z., & Lei, L. (2023). The carbon sink in China as seen from GOSAT with a regional inversion system based on the Community Multi-scale Air Quality (CMAQ) and ensemble Kalman smoother (EnKS). *Atmos. Chem. Phys.*, *23*(12), 6719-6741. https://doi.org/10.5194/acp-23-6719-2023

Kountouris, P., Gerbig, C., Rödenbeck, C., Karstens, U., Koch, T. F., & Heimann, M. (2018). Technical Note: Atmospheric CO2 inversions on the mesoscale using data-driven prior uncertainties: methodology and system evaluation. *Atmos. Chem. Phys.*, *18*(4), 3027-3045. https://doi.org/10.5194/acp-18-3027-2018

Landcare Research. (2010a). *Fundamental Soil Layer - New Zealand Soil Classification [dataset]*.

Landcare Research. (2010b). *LENZ - Slope [dataset]*. https://doi.org/10.26060/TBMR-RE43

Landcare Research. (2020). *LCDB v5.0 - Land Cover Database version 5.0, Mainland, New Zealand (5.0)*. https://doi.org/10.26060/W5B4-WK93

Landschützer, P., Gruber, N., & Bakker, D. C. E. (2017). *An observation-based global monthly gridded sea surface pCO2 product from 1982 onward and its monthly climatology. (NCEI Accession 0160558). Version 5.5* NOAA National Centers for Environmental Information. Accessed 2021-05-21. https://doi.org/10.7289/v5z899n6

Landschützer, P., Laruelle, G. G., Roobaert, A., & Regnier, P. (2020). A uniform pCO2 climatology combining open and coastal oceans. *Earth Syst. Sci. Data*, *12*(4), 2537-2553. https://doi.org/10.5194/essd-12-2537-2020

Lowe, D. C., Guenther, P. R., & Keeling, C. D. (1979). The concentration of atmospheric carbon dioxide at Baring Head, New Zealand. *Tellus A: Dynamic Meteorology and Oceanography*. https://doi.org/10.3402/tellusa.v31i1.10410

Lu, X., Jacob, D. J., Wang, H., Maasakkers, J. D., Zhang, Y., Scarpelli, T. R., Shen, L., Qu, Z., Sulprizio, M. P., Nesser, H., Bloom, A. A., Ma, S., Worden, J. R., Fan, S., Parker, R. J., Boesch, H., Gautam, R., Gordon, D., Moran, M. D., Reuland, F., Villasana, C. A. O., & Andrews, A. (2022). Methane emissions in the United States, Canada, and Mexico: evaluation of national methane emission inventories and 2010–2017 sectoral trends by inverse analysis of in situ (GLOBALVIEWplus CH4 ObsPack) and satellite (GOSAT) atmospheric observations. *Atmos. Chem. Phys.*, *22*(1), 395-418. https://doi.org/10.5194/acp-22-395-2022

Luyssaert, S., Schulze, E. D., Börner, A., Knohl, A., Hessenmöller, D., Law, B. E., Ciais, P., & Grace, J. (2008). Old-growth forests as global carbon sinks. *Nature*, *455*(7210), 213-215. https://doi.org/10.1038/nature07276

Maasakkers, J. D., Jacob, D. J., Sulprizio, M. P., Scarpelli, T. R., Nesser, H., Sheng, J., Zhang, Y., Lu, X., Bloom, A. A., Bowman, K. W., Worden, J. R., & Parker, R. J. (2021). 2010–2015 North American methane emissions, sectoral contributions, and trends: a high-resolution inversion of GOSAT observations of atmospheric methane. *Atmos. Chem. Phys.*, *21*(6), 4339-4356. https://doi.org/10.5194/acp-21-4339-2021

Manning, A. J., O'Doherty, S., Jones, A. R., Simmonds, P. G., & Derwent, R. G. (2011). Estimating UK methane and nitrous oxide emissions from 1990 to 2007 using an inversion modeling approach. *Journal of Geophysical Research: Atmospheres*, *116*(D2). https://doi.org/10.1029/2010JD014763

Manning, M. R., & Pohl, K. P. (1986). Atmospheric carbon dioxide monitoring in New Zealand, 1971–1985. *DSIR, Institute of Nuclear Sciences, Lower Hutt, New Zealand*. http://webcat.niwa.co.nz/documents/INS-R-350.pdf

Matross, D. M., Andrews, A., Pathmathevan, M., Gerbig, C., Lin, J. C., Wofsy, S. C., Daube, B. C., Gottlieb, E. W., Chow, V. Y., Lee, J. T., Zhao, C., Bakwin, P. S., Munger, J. W., & Hollinger, D. Y. (2006). Estimating regional carbon exchange in New England and Quebec by combining atmospheric, ground-based and satellite data. *Tellus B: Chemical and Physical Meteorology*. https://doi.org/10.1111/j.1600-0889.2006.00206.x

Meesters, A. G. C. A., Tolk, L. F., Peters, W., Hutjes, R. W. A., Vellinga, O. S., Elbers, J. A., Vermeulen, A. T., van der Laan, S., Neubert, R. E. M., Meijer, H. A. J., & Dolman, A. J. (2012). Inverse carbon dioxide flux estimates for the Netherlands. *Journal of Geophysical Research: Atmospheres*, *117*(D20). https://doi.org/10.1029/2012JD017797

Miller, S. M., Michalak, A. M., & Levi, P. J. (2014). Atmospheric inverse modeling with known physical bounds: an example from trace gas emissions. *Geosci. Model Dev.*, *7*(1), 303-315. https://doi.org/10.5194/gmd-7-303-2014

Miller, S. M., Wofsy, S. C., Michalak, A. M., Kort, E. A., Andrews, A. E., Biraud, S. C., Dlugokencky, E. J., Eluszkiewicz, J., Fischer, M. L., Janssens-Maenhout, G., Miller, B. R., Miller, J. B., Montzka, S. A., Nehrkorn, T., & Sweeney, C. (2013). Anthropogenic emissions of methane in the United States. *Proceedings of the National Academy of Sciences*, *110*(50), 20018-20022. https://doi.org/doi:10.1073/pnas.1314392110

Ministry for the Environment. (2015). New Zealand's Greenhouse Gas Inventory 1990–2013. In. Wellington: Ministry for the Environment.

Ministry for the Environment. (2016). *LUCAS NZ Land Use Map (v008) [dataset]*.

Ministry for the Environment. (2023). New Zealand's Greenhouse Gas Inventory 1990–2021. In. Wellington: Ministry for the Environment.

Ministry for the Environment. (2024). New Zealand's Greenhouse Gas Inventory 1990–2022. In. Wellington: Ministry for the Environment.

Mudge, P. L., Millar, J., Pronger, J., Roulston, A., Penny, V., Fraser, S., Eger, A., Caspari, T., Robertson, B., Mason, N. W. H., & Schipper, L. A. (2021). Impacts of irrigation on soil C and N stocks in grazed grasslands depends on aridity and irrigation duration. *Geoderma*, *399*, 115109. https://doi.org/10.1016/j.geoderma.2021.115109

Müller, A., Tanimoto, H., Sugita, T., Machida, T., Nakaoka, S., Patra, P. K., Laughner, J., & Crisp, D. (2021). New approach to evaluate satellite-derived XCO2 over oceans by integrating ship and aircraft observations. *Atmos. Chem. Phys.*, *21*(10), 8255-8271. https://doi.org/10.5194/acp-21-8255-2021

Nickless, A., Rayner, P. J., Engelbrecht, F., Brunke, E. G., Erni, B., & Scholes, R. J. (2018). Estimates of CO2 fluxes over the city of Cape Town, South Africa, through Bayesian inverse modelling. *Atmos. Chem. Phys.*, *18*(7), 4765-4801. https://doi.org/10.5194/acp-18-4765-2018

Odum, E. P. (1969). The Strategy of Ecosystem Development. *Science*, *164*(3877), 262-270. https://doi.org/doi:10.1126/science.164.3877.262

Paul, T., Kimberley, M. O., & Beets, P. N. (2021). Natural forests in New Zealand – a large terrestrial carbon pool in a national state of equilibrium. *Forest Ecosystems*, *8*(1), 34. https://doi.org/10.1186/s40663-021-00312-0

Peylin, P., Houweling, S., Krol, M. C., Karstens, U., Rödenbeck, C., Geels, C., Vermeulen, A., Badawy, B., Aulagnier, C., Pregger, T., Delage, F., Pieterse, G., Ciais, P., & Heimann, M. (2011). Importance of fossil fuel emission uncertainties over Europe for CO2 modeling: model intercomparison. *Atmos. Chem. Phys.*, *11*(13), 6607-6622. https://doi.org/10.5194/acp-11-6607-2011

Philip, S., Johnson, M. S., Potter, C., Genovesse, V., Baker, D. F., Haynes, K. D., Henze, D. K., Liu, J., & Poulter, B. (2019). Prior biosphere model impact on global terrestrial CO2 fluxes estimated from OCO-2 retrievals. *Atmos. Chem. Phys.*, *19*(20), 13267-13287. https://doi.org/10.5194/acp-19-13267-2019

Pietsch, S. A., Hasenauer, H., & Thornton, P. E. (2005). BGC-model parameters for tree species growing in central European forests. *Forest Ecology and Management*, *211*(3), 264-295. https://doi.org/10.1016/j.foreco.2005.02.046

Prather, M. J., Zhu, X., Strahan, S. E., Steenrod, S. D., & Rodriguez, J. M. (2008). Quantifying errors in trace species transport modeling. *Proceedings of the National Academy of Sciences*, *105*(50), 19617-19621. https://doi.org/doi:10.1073/pnas.0806541106

Pregitzer, K. S., & Euskirchen, E. S. (2004). Carbon cycling and storage in world forests: biome patterns related to forest age. *Global Change Biology*, *10*(12), 2052-2077. https://doi.org/10.1111/j.1365-2486.2004.00866.x

Pugh, T. A. M., Lindeskog, M., Smith, B., Poulter, B., Arneth, A., Haverd, V., & Calle, L. (2019). Role of forest regrowth in global carbon sink dynamics. *Proceedings of the National Academy of Sciences*, *116*(10), 4382-4387. https://doi.org/doi:10.1073/pnas.1810512116

Regnier, P., Resplandy, L., Najjar, R. G., & Ciais, P. (2022). The land-to-ocean loops of the global carbon cycle. *Nature*, *603*(7901), 401-410. https://doi.org/10.1038/s41586-021-04339-9

Rodgers, C. D. *Inverse Methods for Atmospheric Sounding*. https://doi.org/10.1142/3171

Roobaert, A., Laruelle, G. G., Landschützer, P., & Regnier, P. (2018). Uncertainty in the global oceanic CO2 uptake induced by wind forcing: quantification and spatial analysis. *Biogeosciences*, *15*(6), 1701-1720. https://doi.org/10.5194/bg-15-1701-2018

Running, S. W., & Coughlan, J. C. (1988). A general model of forest ecosystem processes for regional applications I. Hydrologic balance, canopy gas exchange and primary production processes. *Ecological Modelling*, *42*(2), 125-154. https://doi.org/https://doi.org/10.1016/0304-3800(88)90112-3

Running, S. W., & Gower, S. T. (1991). FOREST-BGC, A general model of forest ecosystem processes for regional applications. II. Dynamic carbon allocation and nitrogen budgets1. *Tree Physiology*, *9*(1-2), 147-160. https://doi.org/10.1093/treephys/9.1-2.147

Saeki, T., & Patra, P. K. (2017). Implications of overestimated anthropogenic CO2 emissions on East Asian and global land CO2 flux inversion. *Geoscience Letters*, *4*(1), 9. https://doi.org/10.1186/s40562-017-0074-7

Schimel, D., Stephens, B. B., & Fisher, J. B. (2015). Effect of increasing CO2 on the terrestrial carbon cycle. *Proceedings of the National Academy of Sciences*, *112*(2), 436-441. https://doi.org/doi:10.1073/pnas.1407302112

Schipper, L. A., L., M. P., F., K. M. U., B., H. C., E., G. N., J., S. S., & and Kelliher, F. M. (2017). A review of soil carbon change in New Zealand's grazed grasslands. *New Zealand Journal of Agricultural Research*, *60*(2), 93-118. https://doi.org/10.1080/00288233.2017.1284134

Schipper, L. A., Parfitt, R. L., Fraser, S., Littler, R. A., Baisden, W. T., & Ross, C. (2014). Soil order and grazing management effects on changes in soil C and N in New Zealand pastures. *Agriculture, Ecosystems & Environment*, *184*, 67-75. https://doi.org/10.1016/j.agee.2013.11.012

Schnecker, J., Baldaszti, L., Gündler, P., Pleitner, M., Sandén, T., Simon, E., Spiegel, F., Spiegel, H., Urbina Malo, C., Zechmeister-Boltenstern, S., & Richter, A. (2023). Seasonal dynamics of soil microbial growth, respiration, biomass, and carbon use efficiency in temperate soils. *Geoderma*, *440*, 116693. https://doi.org/10.1016/j.geoderma.2023.116693

Schuh, A. E., Denning, A. S., Corbin, K. D., Baker, I. T., Uliasz, M., Parazoo, N., Andrews, A. E., & Worthy, D. E. J. (2010). A regional high-resolution carbon flux inversion of North America for 2004. *Biogeosciences*, *7*(5), 1625-1644. https://doi.org/10.5194/bg-7-1625-2010

Scott, D. T., Baisden, W. T., Davies-Colley, R., Gomez, B., Hicks, D. M., Page, M. J., Preston, N. J., Trustrum, N. A., Tate, K. R., & Woods, R. A. (2006). Localized erosion affects national carbon budget. *Geophysical Research Letters*, *33*(1). https://doi.org/10.1029/2005GL024644

Smale, D., Sherlock, V., Griffith, D. W. T., Moss, R., Brailsford, G., Nichol, S., & Kotkamp, M. (2019). A decade of CH4, CO and N2O in situ measurements at Lauder, New Zealand: assessing the long-term performance of a Fourier transform infrared trace gas and isotope analyser. *Atmos. Meas. Tech.*, *12*(1), 637-673. https://doi.org/10.5194/amt-12-637-2019

Sousa, W. P. (1984). The Role of Disturbance in Natural Communities. *Annual Review of Ecology, Evolution, and Systematics*, *15*(Volume 15), 353-391. https://doi.org/10.1146/annurev.es.15.110184.002033

Sparling, G. P., Chibnall, E. J., Pronger, J., Rutledge, S., Wall, A. M., Campbell, D. I., & and Schipper, L. A. (2016). Estimates of annual leaching losses of dissolved organic carbon from pastures on Allophanic Soils grazed by dairy cattle, Waikato, New Zealand. *New Zealand Journal of Agricultural Research*, *59*(1), 32-49. https://doi.org/10.1080/00288233.2015.1120222

Stallard, R. F. (1998). Terrestrial sedimentation and the carbon cycle: Coupling weathering and erosion to carbon burial. *Global Biogeochemical Cycles*, *12*(2), 231-257. https://doi.org/10.1029/98GB00741

Steinkamp, K., Mikaloff Fletcher, S. E., Brailsford, G., Smale, D., Moore, S., Keller, E. D., Baisden, W. T., Mukai, H., & Stephens, B. B. (2017). Atmospheric CO2 observations and models suggest strong carbon uptake by forests in New Zealand. *Atmos. Chem. Phys.*, *17*(1), 47-76. https://doi.org/10.5194/acp-17-47-2017

Stephens, B. B., Brailsford, G. W., Gomez, A. J., Riedel, K., Mikaloff Fletcher, S. E., Nichol, S., & Manning, M. (2013). Analysis of a 39-year continuous atmospheric CO2 record from Baring Head, New Zealand. *Biogeosciences*, *10*(4), 2683-2697. https://doi.org/10.5194/bg-10-2683-2013

Stephens, B. B., Miles, N. L., Richardson, S. J., Watt, A. S., & Davis, K. J. (2011). Atmospheric CO2 monitoring with single-cell NDIR-based analyzers. *Atmos. Meas. Tech.*, *4*(12), 2737-2748. https://doi.org/10.5194/amt-4-2737-2011

Stephenson, N. L., Das, A. J., Condit, R., Russo, S. E., Baker, P. J., Beckman, N. G., Coomes, D. A., Lines, E. R., Morris, W. K., Rüger, N., Álvarez, E., Blundo, C., Bunyavejchewin, S., Chuyong, G., Davies, S. J., Duque, Á., Ewango, C. N., Flores, O., Franklin, J. F., Grau, H. R., Hao, Z., Harmon, M. E., Hubbell, S. P., Kenfack, D., Lin, Y., Makana, J. R., Malizia, A., Malizia, L. R., Pabst, R. J., Pongpattananurak, N., Su, S. H., Sun, I. F., Tan, S., Thomas, D., van Mantgem, P. J., Wang, X., Wiser, S. K., & Zavala, M. A. (2014). Rate of tree carbon accumulation increases continuously with tree size. *Nature*, *507*(7490), 90-93. https://doi.org/10.1038/nature12914

Tait, A., Henderson, R., Turner, R., & Zheng, X. (2006). Thin plate smoothing spline interpolation of daily rainfall for New Zealand using a climatological rainfall surface. *International Journal of Climatology*, *26*(14), 2097-2115. https://doi.org/10.1002/joc.1350

Tait, A., & Liley, B. (2009). Interpolation of daily solar radiation for New Zealand using a satellite data-derived cloud cover surface. *Weather and Climate*, *29*, 70-88. https://doi.org/10.2307/26169706

Tait, A., Sturman, J., & Clark, M. (2012). An assessment of the accuracy of interpolated daily rainfall for New Zealand. *Journal of Hydrology (New Zealand)*, *51(1)*, 25-44.

Tait, A. B. (2008). Future projections of growing degree days and frost in New Zealand and some implications for grape growing. *Weather and Climate*, *28*, 17-36. https://doi.org/10.2307/26169696

Tarantola, A. (2005). *Inverse Problem Theory and Methods for Model Parameter Estimation*. SIAM. https://doi.org/10.1137/1.9780898717921

Terao, Y., Mukai, H., Nojiri, Y., Machida, T., Tohjima, Y., Saeki, T., & Maksyutov, S. (2011). Interannual variability and trends in atmospheric methane over the western Pacific from 1994 to 2010. *Journal of Geophysical Research: Atmospheres*, *116*(D14). https://doi.org/10.1029/2010JD015467

Thornton, P. E., Law, B. E., Gholz, H. L., Clark, K. L., Falge, E., Ellsworth, D. S., Goldstein, A. H., Monson, R. K., Hollinger, D., Falk, M., Chen, J., & Sparks, J. P. (2002). Modeling and measuring the effects of disturbance history and climate on carbon and water budgets in evergreen needleleaf forests. *Agricultural and Forest Meteorology*, *113*(1), 185-222. https://doi.org/10.1016/S0168-1923(02)00108-9

Thornton, P. E., & Rosenbloom, N. A. (2005). Ecosystem model spin-up: Estimating steady state conditions in a coupled terrestrial carbon and nitrogen cycle model. *Ecological Modelling*, *189*(1), 25-48. https://doi.org/10.1016/j.ecolmodel.2005.04.008

Thornton, P. E., Running, S. W., & Hunt, E. R. (2005). *Biome-BGC: Terrestrial Ecosystem Process Model*. In (Version Version 4.2 Final Release, Accessed on 12-11-2023) http://www.ntsg.umt.edu/project/biome-bgc

Tian, H., Yao, Y., Li, Y., Shi, H., Pan, S., Najjar, R. G., Pan, N., Bian, Z., Ciais, P., Cai, W.-J., Dai, M., Friedrichs, M. A. M., Li, H.-Y., Lohrenz, S., & Leung, L. R. (2023). Increased Terrestrial Carbon Export and CO2 Evasion From Global Inland Waters Since the Preindustrial Era. *Global Biogeochemical Cycles*, *37*(10), e2023GB007776. https://doi.org/10.1029/2023GB007776

Turner, A. J., & Jacob, D. J. (2015). Balancing aggregation and smoothing errors in inverse models. *Atmos. Chem. Phys.*, *15*(12), 7039-7048. https://doi.org/10.5194/acp-15-7039-2015

UNFCCC. (1997). Kyoto Protocol to the United Nations Framework Convention on Climate Change. In.

UNFCCC. (2015). Adoption of the Paris Agreement. In.

UNFCCC. (2018). Modalities, procedures and guidelines for the transparency framework for action and support referred to in Article 13 of the Paris Agreement. In.

Van Tuyl, S., Law, B. E., Turner, D. P., & Gitelman, A. I. (2005). Variability in net primary production and carbon storage in biomass across Oregon forests—an assessment integrating data from forest inventories, intensive sites, and remote sensing. *Forest Ecology and Management*, *209*(3), 273-291. https://doi.org/10.1016/j.foreco.2005.02.002

Villalobos, Y., Canadell, J. G., Keller, E. D., Briggs, P. R., Bukosa, B., Giltrap, D. L., Harman, I., Hilton, T. W., Kirschbaum, M. U. F., Lauerwald, R., Liang, L. L., Maavara, T., Mikaloff-Fletcher, S. E., Rayner, P. J., Resplandy, L., Rosentreter, J., Metz, E.-M., Serrano, O., & Smith, B. (2023). A Comprehensive Assessment of Anthropogenic and Natural Sources and Sinks of Australasia's Carbon Budget. *Global Biogeochemical Cycles*, *37*(12), e2023GB007845. https://doi.org/10.1029/2023GB007845

Walker, A. P., De Kauwe, M. G., Medlyn, B. E., Zaehle, S., Iversen, C. M., Asao, S., Guenet, B., Harper, A., Hickler, T., Hungate, B. A., Jain, A. K., Luo, Y., Lu, X., Lu, M., Luus, K., Megonigal, J. P., Oren, R., Ryan, E., Shu, S., Talhelm, A., Wang, Y.-P., Warren, J. M., Werner, C., Xia, J., Yang, B., Zak, D. R., & Norby, R. J. (2019). Decadal biomass increment in early secondary succession woody ecosystems is increased by CO2 enrichment. *Nature Communications*, *10*(1), 454. https://doi.org/10.1038/s41467-019-08348-1

Wall, A. M., Laubach, J., Campbell, D. I., Goodrich, J. P., Graham, S. L., Hunt, J. E., Mudge, P. L., Whitehead, D., & Schipper, L. A. (2024). Effects of dairy farming management practices on carbon balances in New Zealand's grazed grasslands: Synthesis from 68 site-years. *Agriculture, Ecosystems & Environment*, *367*, 108962. https://doi.org/10.1016/j.agee.2024.108962

Webster, S., Uddstrom, M., Oliver, H., & Vosper, S. (2008). A high-resolution modelling case study of a severe weather event over New Zealand. *Atmospheric Science Letters*, *9*(3), 119-128. https://doi.org/10.1002/asl.172

White, E. D., Rigby, M., Lunt, M. F., Smallman, T. L., Comyn-Platt, E., Manning, A. J., Ganesan, A. L., O'Doherty, S., Stavert, A. R., Stanley, K., Williams, M., Levy, P., Ramonet, M., Forster, G. L., Manning, A. C., & Palmer, P. I. (2019). Quantifying the UK's carbon dioxide flux: an atmospheric inverse modelling approach using a regional measurement network. *Atmos. Chem. Phys.*, *19*(7), 4345-4365. https://doi.org/10.5194/acp-19-4345-2019

White, M. A., Thornton, P. E., Running, S. W., & Nemani, R. R. (2000). Parameterization and Sensitivity Analysis of the BIOME–BGC Terrestrial Ecosystem Model: Net Primary Production Controls. *Earth interactions*, *4*(3), 1-85. https://doi.org/10.1175/1087-3562(2000)004<0003:PASAOT>2.0.CO;2

Yamagishi, H., Tohjima, Y., Mukai, H., Nojiri, Y., Miyazaki, C., & Katsumata, K. (2012). Observation of atmospheric oxygen/nitrogen ratio aboard a cargo ship using gas chromatography/thermal conductivity detector. *Journal of Geophysical Research: Atmospheres*, *117*(D4). https://doi.org/10.1029/2011JD016939

Inverse modelling of New Zealand's carbon dioxide balance shows a larger than expected carbon sink

Beata Bukosa

Correspondence: Beata Bukosa (Beata.Bukosa@niwa.co.nz)

S1 ~~Inversion system~~

~~We used a Bayesian approach to estimate net air-sea and air-land CO_2 fluxes (Steinkamp et al., 2017; Gurney et al., 2004) for 25 geographic regions (Figure **??**). The inversion was based on the Bayesian cost function J, calculated as (Tarantola, 2005):~~

$$J = \frac{1}{2}(Tx - d)^T C_d^{-1}(Tx - d) + \frac{1}{2}(x - x_0)^T C_0^{-1}(x - x_0)$$

~~where T is the transport (jacobian) matrix, d is the data time series, x_0 is the prior flux, while C_d and C_0 are the data and prior covariance matrix, respectively. The function was minimized analytically to yield the posterior fluxes (x) and associated posterior error covariance matrix (C) (Enting, 2002) :~~

$$x = C(T^T C_d^{-1} d + C_0^{-1} x_0)$$

$$C = (T^T C_d^{-1} T + C_0^{-1})^{-1}$$

~~Equation **??** represents the sum of the modelled versus measured CO_2 differences (Tx - d) and the optimized posterior versus prior flux differences (x - x_0). Each data and flux point is weighted by their uncertainty defined through the data and prior covariance matrix C_d and C_0. The main diagonal of the covariance matrices represents data and prior flux variance while off-diagonal elements contain information about the temporal and spatial correlations of the uncertainties. The first term in Eq. **??** also includes a Gaussian smoother focusing on week-to-week flux changes as described by Steinkamp et al. (2017). We used a reduced chi test (2J divided by the number of observations) (**?**) to assess the fit of the inverse model to the observations. The ideal chi-squared value equals 1, with values < 1 indicating that the uncertainties in C_d and/or C_0 are too large while values > 1 suggest that the uncertainties are underestimated (Nickless et al., 2017). Results from the reduced chi test were used as a scaling factor to weight the data uncertainties in the inversion.~~

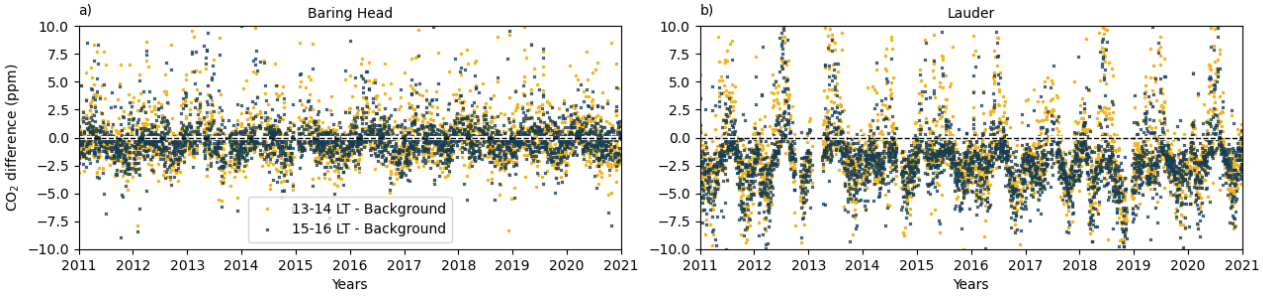

Figure S1. ~~S2~~ S1 Difference between the 13:00-14:00 (yellow) and 15:00-16:00 (blue) local time CO_2 measurements and the background values at Baring Head (a) and Lauder (b).

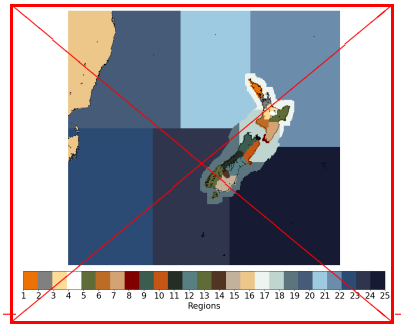

~~Domain boundaries for the 25 inversion regions, New Zealand South Island (regions 1-8), New Zealand North Island (regions 9-15), Australia (region 16), coastal ocean (regions 17-19), open ocean (regions 20-25).~~

S1 ~~S2~~ S1 Sites, measurements and background

We used hourly mean surface measurements from Baring Head and Lauder, averaged over 13:00 to 14:00 and 15:00 to 16:00 local time, when the air is well-mixed so that the CO_2 signal is representative of regional processes. We have used local time instead of standard local time to account for the shift in hours relative to daylight (i.e., shorter days during winter periods). We excluded data outside of 3 standard deviations of the whole measurement period to remove the influence of local CO_2 processes. The final data for the inversion was constructed by subtracting background measurements from the afternoon measurements at the two sites Fig. S1 ~~S2~~ S1 .

We use a background-sector method to classify the CO_2 background values (Manning, 2011; Steinkamp et al., 2017; Uglietti et al., 2011). Southerly background conditions at Baring Head are present during periods with southerly winds, no land contact and low CO_2 variability (standard deviation < 0.1 ppm, over a minimum of 6 hours) (Stephens et al., 2013), hence can be classified as oceanic air (Brailsford et al., 2012). Data points from the TF5 background CO_2 values were selected when the air originated from directions away from coastal regions and typically for regions between 26 and 27°S. Both background data sets had gaps, hence we used the seasonal time series decomposition by the Loess (STL) algorithm to construct a continuous

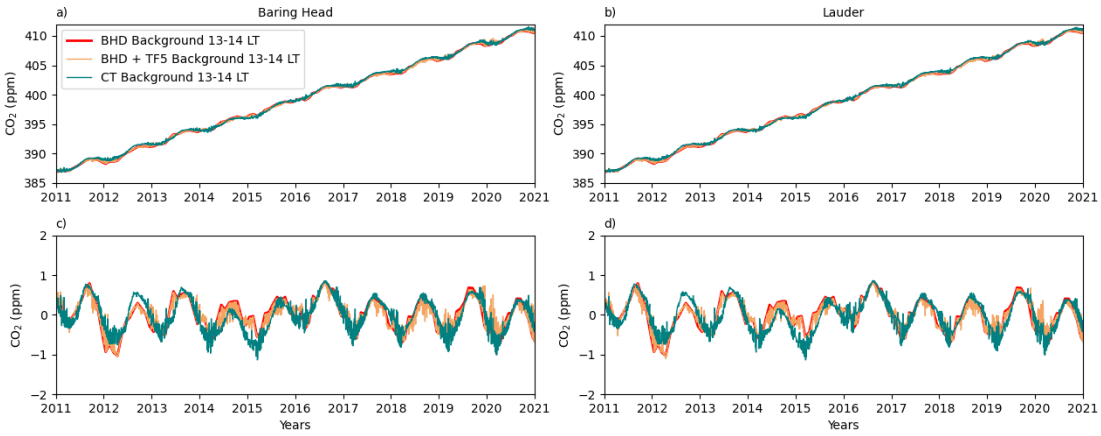

Figure S2. ~~S3~~ S2 Timeseries of the background values at Baring Head and Lauder at 13-14 local time, estimated from Baring Head baseline values, merged Baring Head and Trans Future 5 ship (TF5) measurements, as well as CarbonTracker CO_2 mole fractions. Plots c and d show the detrended values.

background time series (Cleveland et al., 1990). The two backgrounds were then combined based on modelled back trajectories for 13:00-14:00 and 15:00-16:00 local time at Baring Head and Lauder (Steinkamp et al., 2017). A time series of the detrended background values can be found in Fig. S2 ~~S3~~ S2 . The background CO_2 values were generally higher than measurements collected at 13:00-14:00 and 15:00-16:00 local time (Fig. ~~2a~~ 3a and Fig. ~~2b~~3b), especially at Lauder, suggesting that overall, New Zealand acted as a CO_2 sink. However, during winter periods we also observed elevated CO_2 values, at both sites, pointing to CO_2 release.

Measurements at Baring Head are from the non-dispersive infrared (NDIR) analyser (Ultramat 3, Siemens, Brailsford et al. (2012)) for the years 2011-2016. In 2016, the instrument was changed to a three-species greenhouse gas cavity ring down spectroscopy analyzer (G2301, Picarro Inc.), and in 2018, the instrument was updated to a four-species analyzer (G2401, Picarro Inc.). The control and calibration procedures described in Brailsford et al. (2012) remained unchanged and were applied for the calibration of each new analyser. The Lauder CO_2 were collected using a dual cell NDIR *in situ* analyser (LI-7000, LI-COR Inc.) with a similar control system as at Baring Head but using nafion drying instead of cryo drying. Baring Head uses a suite of transfer gases provided by the World Meteorological Organization Central Calibration Lab (WMO CCL) at the National Oceanic and Atmospheric Administration (NOAA), while Lauder uses a suite of gases defined at Baring Head against the same transfer suite. Hence the observations are made based on reference gases with the same lineage. To verify the *in situ* observations a suite of four gases from the CCL known as the Aniwaniwa suite are measured as unknowns at each site to assess site specific biases. Sample air at both sites were collected from a 10 m air inlet height. The analysers were calibrated against a suite of standard reference gases with assigned mole fractions on the relevant World Meteorological Organization – Global Atmosphere Watch (WMO-GAW) scales - the WMO X2019. The Lauder measurements were not directly calibrated to

the WMO X2019 scale. We have used the conversion from Equation 6 in Hall et al. (2021) to convert the X2007 to the X2019 scale.

S2 ~~S3~~ S2 Atmospheric transport model

In our inversion, we used the NAME III vn6.5 dispersion model for the years 2014-2020 while for the period 2011-2013, we retained the original NAME III vn6.1 simulations previously described in Steinkamp et al. (2017) (Fig. S3, ~~S4~~ S3). We used NIWA's operational NZLAM fields for the years 2011-2013 and NZCSM data for the period from mid-2016 to 2020. NAME III required input data that was not routinely generated by NZCSM for the period 2014 to mid-2016. For this period, we therefore configured a NZCSM-like model workflow that was run in hindcast mode, creating NAME III input fields for the 2014 to mid-2016 period.

Both NZLAM and NZCSM are New Zealand specific configurations of the UK Met Office Unified Model (UM) (Davies et al., 2005) and use the same semi-implicit semi-Lagrangian dynamical core, called "ENDGame" (Wood et al., 2014), but they differ in their domain size, horizontal (Fig. S4, ~~S5~~ S4) and vertical resolutions, as well their scientific configurations. NZLAM provides meteorological outputs on a 324x324 grid point ≈12 km horizontal resolution with hourly forecast output resolution, while NZCSM operates at a finer 1200x1350 grid point, ≈1.5 km spatial resolution, generating 30-minute temporal resolution output. Both models utilise 70 vertical levels, with NZLAM extending to 80 km above the surface and NZCSM to 40 km. NZCSM thereby achieves a higher resolution through the boundary layer and lower troposphere. We note that the NZCSM model from the mid 2016 to mid 2017 period was based on the "pre-ENDGAME" version of the model.

To ~~creata~~ create the NZCSM-like meteorological input, UK Met Office Global model analyses were retrieved for 00Z for each day in the re-run period. A N768 horizontal resolution (approximately 17km at mid-latitudes) UM Global model forecast, running the GA6.1 science configuration (Walters et al., 2017) was run for 30 hours, outputting at hourly intervals lateral boundary condition data for a one-way nested ≈12 km resolution NZLAM-like regional model. This model also used the GA6.1 science configuration, which was very similar to the operational NZLAM model of the time and was also run for 30 hours, with lateral boundary condition data generated to drive a one-way nested NZCSM-like ≈1.5 km horizontal resolution regional model. The science configuration used in this ≈1.5 km resolution model was the mid-latitude Regional Atmosphere 2 (RAL2-M) set-up favoured by convection-resolving regional UM configurations, featuring minor changes to the RA1-M configuration described in Bush et al. (2020). This nesting set-up mirrored the operational nesting of the NZLAM and NZCSM model of the time. Both regional models were configured to output all necessary data to force a NAME III simulation. To allow for model spin-up, the first 6 hours of each forecast were ignored when constructing a continuous time series of data from which the NAME III simulations were run.

S2.1 ~~S3.1~~ S2.1 Atmospheric transport model comparison

In addition to the wind speed and direction (Fig. S6 ~~S7~~ S6) we also compare the height of measured Planetary Boundary Layer (PBL) at Lauder with modelled values (Fig. S5 ~~S6~~ S5). The PBL dataset is based on radiosonde measurements as described

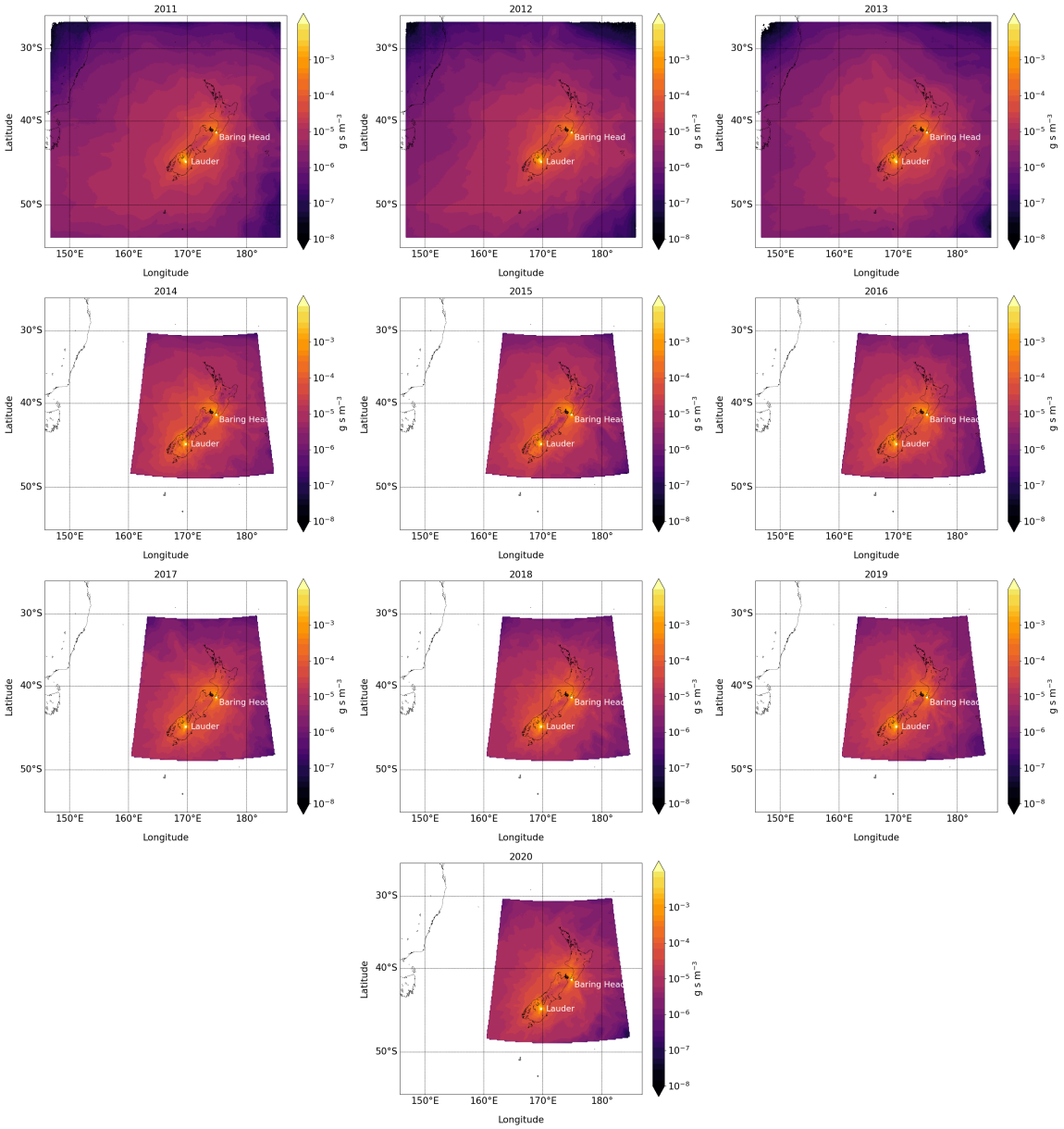

Figure S3. ~~S4~~ S3 Combined NAME III footprints based on Baring Head and Lauder for each year in 2011-2020 at 13-14 and 15-16 local release time. 2011-2013 footprints are based on NZLAM while 2014-2020 is based on NZCSM meteorology input.

in (Steinkamp et al., 2017). Over or underestimated PBL in the model could lead to further biases in the estimated fluxes. The modelled PBL heights are lower than the measurements during the whole inversion period, resulting in a shallower PBL. A shallower PBL and limited vertical mixing could lead to amplified modelled CO_2 mole fractions which could reduce the estimated CO_2 uptake. We have found that all models underestimated the measured PBL.

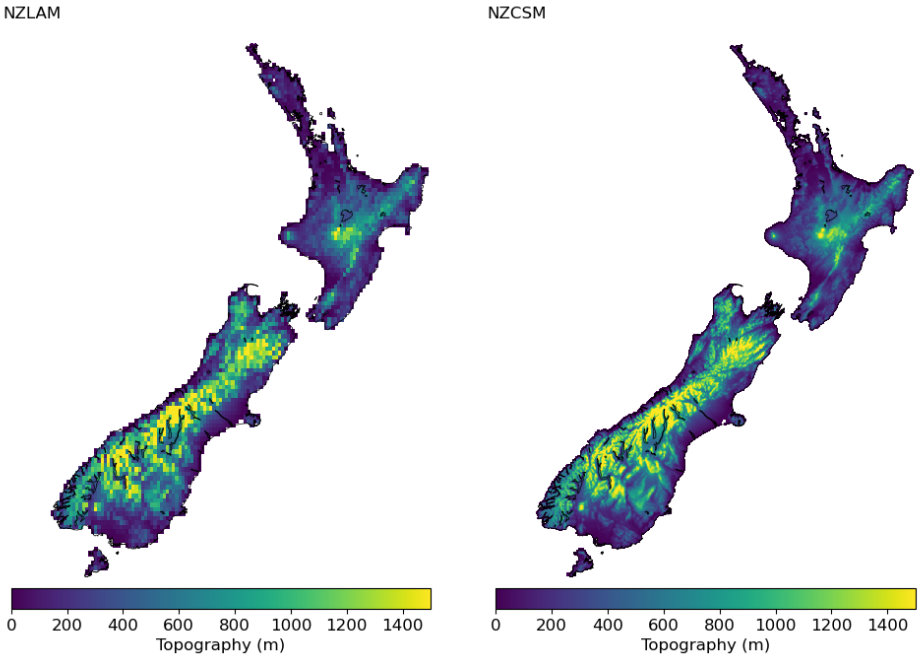

Figure S4. ~~S5~~ S4 New Zealand's Topography in the NZLAM and NZCSM model.

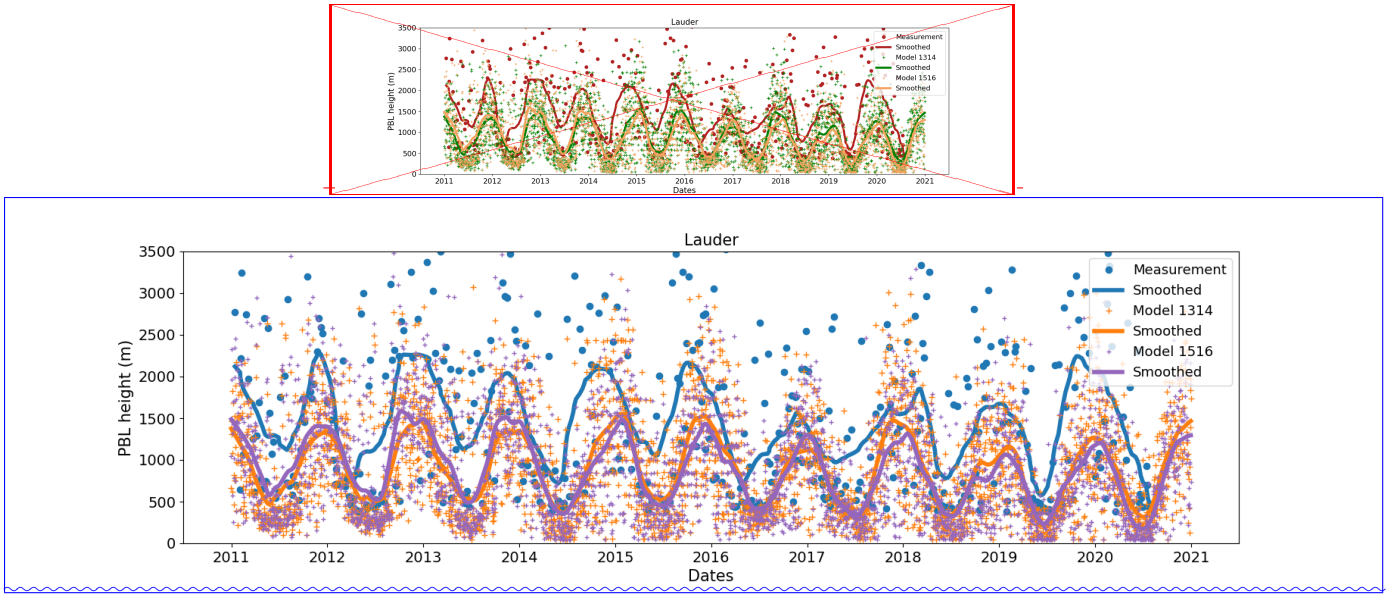

Figure S5. ~~S6~~ S5 Measured (~~red~~blue) and modelled (orange and ~~green~~purple) Planetary Boundary Layer (PBL) height at Lauder. Modelled values are based on 13:00-14 :00 and 15:00-16:00 local time. The measurements are from radiosonde observations and are shown for all available data throughout the day. Lines represent the smoothed estimates of the measured and modelled data.

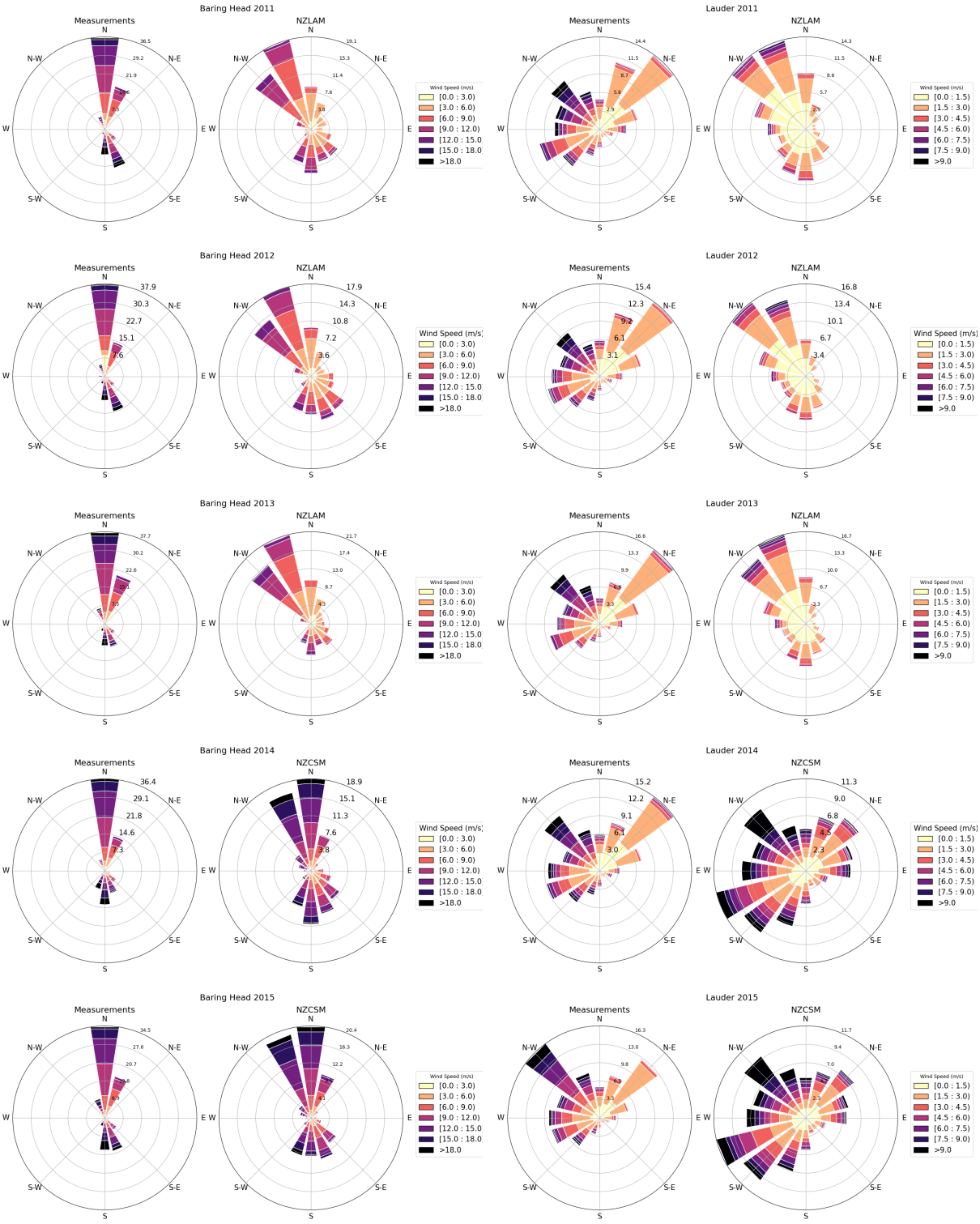

Figure S6. ~~S7~~ S6 Annual modelled and measured wind roses at Baring Head and Lauder.

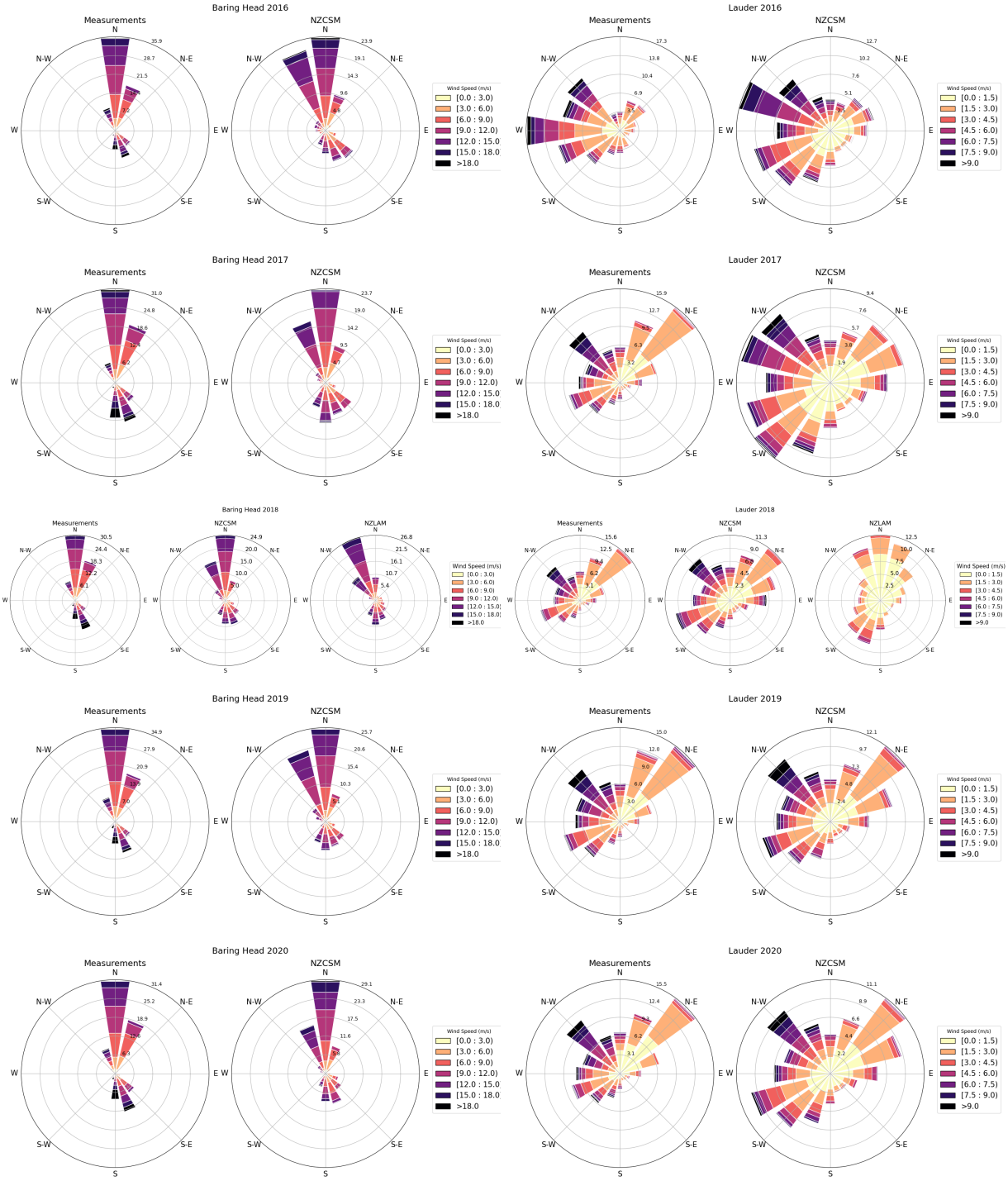

Figure S6. ~~S7~~ S6 Continued. Annual modelled and measured wind roses at Baring Head and Lauder.

S3 ~~S4~~ S3 Prior ocean fluxes

The prior oceanic fluxes in our inversion domain were extracted from monthly global open-ocean ~~air-sea~~ sea-to-air CO_2 fluxes (Landschützer et al., 2016, 2020a). The product from Landschützer et al. (2020a) does not provide fluxes for coastal areas. We therefore merged the open-ocean fluxes with coastal fluxes calculated from the climatology of ocean surface coastal pCO_2 (Landschützer et al., 2020b).

We used year-specific monthly open-ocean CO_2 fluxes up to 2019 (Landschützer et al., 2020a) while for year 2020 we calculated the CO_2 fluxes from 2019 pCO_2 data following the method from Landschützer et al. (2016):

$$F_{CO_2} = k_w \cdot S_{CO_2} \cdot (1 - f_{ice}) \cdot (pCO_2 - pCO_2^{atm}) \tag{1}$$

where F_{CO_2} represent the resulting monthly ~~air-sea~~ sea-to-air flux of CO_2 in mol C m^{-2} yr^{-1}, k_w refers to the gas transfer velocity of CO_2 calculated based on (Sweeney et al., 2007):

$$k_w = 0.27 \cdot (\frac{S_c}{660})^{-\frac{1}{2}} \cdot u^2 \tag{2}$$

where S_c represents the dimensionless Schmidt number (Wanninkhof, 1992), estimated from year-specific (2011-2020) ERA5 monthly sea surface temperature (Hersbach et al., 2019) and u is the monthly mean wind speed from year specific hourly ERA5 wind fields at a height of 10 m above the sea surface (Hersbach et al., 2018). In Eq. 1 S_{CO_2} is the solubility of CO_2 in seawater calculated according to Weiss (1974) using the same ERA5 temperature fields as for the S_c calculation and annual climatology salinity fields from CARS (CSIRO Atlas of Regional Seas, (CARS, 2009)), f_{ice} is the ice cover. However, since the flux calculation was only performed for our inversion domain that is ice-free we assume f_{ice} = 0, pCO_2 is the sea surface partial pressure taken from Landschützer et al. (2020a) for the coastal fluxes and Landschützer et al. (2016) for the 2020 open-ocean fluxes while pCO_2^{atm} represents the partial pressure of atmospheric CO_2 estimated from the baseline dry air mixing ratio xCO_2 at Baring Head and taking into account the water vapor correction according to Dickson et al. (2007):

$$pCO_2^{atm} = xCO_2 \cdot (P_{atm,surf} - P_{H_2O}) \tag{3}$$

where $P_{atm,surf}$ is the mean sea level pressure from monthly ERA5 fields (Hersbach et al., 2019) and P_{H_2O} describes the water vapour pressure (Weiss and Price, 1980).

The 2019 pCO_2 values used for the calculation of the 2020 CO_2 fluxes were additionally extrapolated to the year 2020 based on the 2011-2019 trend of pCO_2. The trend was estimated from monthly average pCO_2 values inside of the inversion domain. We used the same method for the calculation of the coastal CO_2 fluxes. Since the coastal pCO_2 values were based on climatological data, we also scaled the monthly climatology values based on the open-ocean pCO_2 trend.

S4 ~~S5~~ S4 Biome-BGCMuSo, calibration for New Zealand pasture systems

We calibrated 18 ecophysiological model parameters for New Zealand pasture systems ("dairy" and "sheep and beef" biomes) using eddy covariance (EC) data from five sites across New Zealand, with an additional five sites available for validation. All sites had at least one full year of data available, and many had three years or more. The parameters were optimized to produce the best match between observed and modelled weekly mean net ecosystem production (NEP), gross primary production (GPP), Ecosystem Respiration (ER), evapotranspiration (ET), and 10 cm soil moisture content (SMC) using the PEST software package: https://dev-sspa-pest.pantheonsite.io/ (Doherty, 2015). Overall, the model achieved a correlation coefficient R^2 of 0.34 and root mean square error (RMSE) of 1.89 g C m^{-2} day^{-1} at the calibration sites, and 0.37 and 2.01 at the validation sites for modelled NEP against observations. However, these metrics varied significantly among sites, and R^2 for components of NEP (GPP and ER) is higher (0.48 and 0.37, respectively). A full description of the calibration methodology and results are the subject of a forthcoming paper (Keller et al. in prep). Note, in the inversion we are using net ecosystem exchange (NEE) fluxes which are obtained from NEP fluxes (same as NEE but with opposite sign depending on disciplinary convention).

The main difference between the "dairy" and "sheep/beef" systems is the intensity of grazing and the use of fertiliser and irrigation. Dairy farm systems in New Zealand are generally intensely grazed (mean stocking rate of 2.86 cows per hectare in 2020-21; Livestock Improvement Corporation and Dairy NZ (2021)) and fertilised and/or irrigated as needed. The model simulated a stocking rate of 3.0 livestock units (LSU) per hectare for dairy at a weight of 420 kg per LSU and 6.0 LSU per hectare for sheep/beef with weight of 55 kg per LSU. Grazing was simulated by designating one week of grazing and leaving the following three weeks idle during spring, summer, and autumn. No grazing occurred during the winter months (June, July and August). Four different grazing rotations were simulated for each pixel, each offset by one week. Fluxes from each rotation were then averaged to produce a mean value for the pixel. Nitrogen fertiliser was applied twice per year in September and March in dairy systems. Irrigation was simulated for dairy systems in areas where data indicates irrigation is in use (MfE, 2017) . Sheep/beef systems received no fertiliser or irrigation in our simulations. The other Biome-BGCMuSo biomes (ungrazed grassland, shrub, and evergreen broadleaf forest, evergreen needleleaf forest) were not parameterized for New Zealand due to lack of suitable data. Model default parameters were used. Parameter files can be downloaded from the Biome-BGCMuSo website (https://nimbus.elte.hu/bbgc/). The final monthly contribution of the fluxes are shown in Fig. S7 ~~S8~~ S7 .

S4.1 ~~S5.1~~ S4.1 Land cover

The dataset that was used to determine the land cover type for the prior was derived from the New Zealand Land Cover Database (LCDB) v5.0 (Landcare Research, 2020). Each of the LCDB categories was first mapped into five broad categories to construct the prior (Table S1). The grassland category was further disaggregated into dairy, sheep/beef, or ungrazed subcategories based on the LUCAS Land Use Map (MfE, 2016) and further analysis (Manderson et al., 2019) that used a fuzzy logic framework to improve the classification of low- and high-producing grassland and to assign a general farm class (dairy, other livestock, and ungrazed/not otherwise used for agriculture). The area of each category within each VCSN grid cell was translated into a

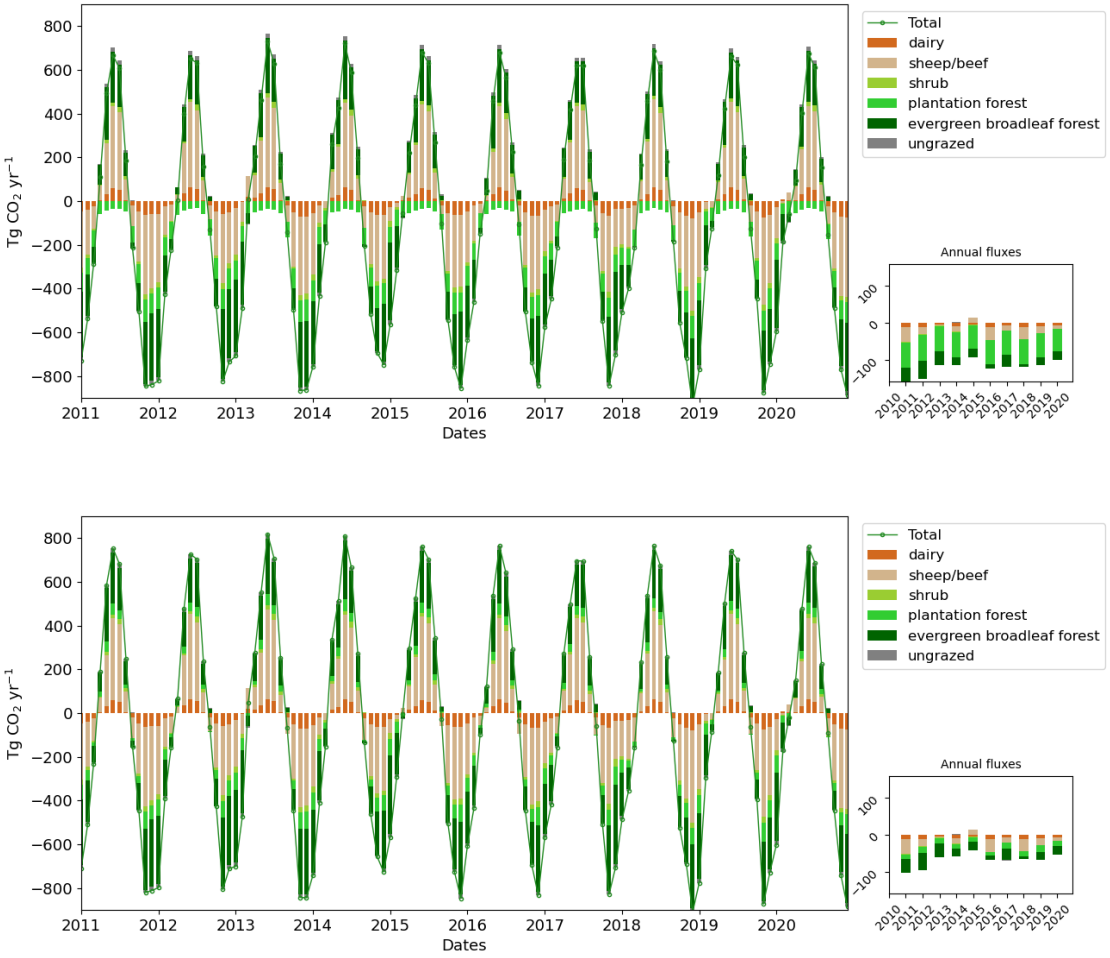

Figure S7. ~~S8~~ S7 Monthly and annual contribution of the fluxes based on the Biome-BGCMuSo biomes and CenW (top plot) and Biome-BGCMuSo (bottom plot).

percentage coverage. The land type with the largest percentage was considered the dominant land type and the whole grid cell was set to that category. This resulted in 12 categories (Table S2) that were grouped into a final 10 category map following the categories in Steinkamp et al. (2017) and matched with the Biome-BGCMuSo biomes (dairy pasture, sheep/beef pasture, ungrazed grassland, shrub, evergreen broadleaf forest (EBF), and evergreen needleleaf forest (ENF)). In our base inversion, the exotic forest category (i.e., ENF) was modelled using *Pinus radiata* fluxes from the CenW mode; however, we also performed inversion sensitivity tests to quantify the impact of Biome-BGCMuSo ENF on our results.

Table S1. Land cover category merging and mapping in Biome-BGCMuSo.

LCDB v5.0 category	Prior category
MANUKA AND / OR KANUKA SUB-ALPINE SHRUBLAND MATAGOURI OR GREY SCRUB MIXED EXOTIC SHRUBLAND GORSE AND / OR BROOM FLAXLAND FERNLAND	Shrub
LOW-PRODUCING GRASSLAND DEPLETED GRASSLAND HIGH-PRODUCING EXOTIC GRASSLAND TALL TUSSOCK GRASSLAND ALPINE GRASS HERBFIELD GRASS OTHER	Grassland (subcategories: dairy, sheep/beef, ungrazed)
EXOTIC FOREST FOREST HARVESTED	Exotic forest (*Pinus radiata* or ENF)
BROADLEAVED INDIGENOUS HARDWOODS DECIDUOUS HARDWOODS INDIGENOUS FOREST	Indigenous forest (EBF)
OTHERS NOT LISTED	Other (zero or non-existing prior flux)

Table S2. Final land cover category merging and mapping.

Prior category	Final Category	Assigned flux
Shrub	Scrub and Shrubland	Biome-BGCMuSo v6.1 dairy pasture
Dairy grassland	Grassland: Dairy pasture	Biome-BGCMuSo v6.1 sheep and beef pasture
Sheep/Beef grassland	Grassland: Sheep/Beef pasture	Biome-BGCMuSo v6.1 shrub
Ungrazed grass	Grassland: Other	Biome-BGCMuSo v6.1 ungrazed grassland
Exotic forest	Forest: Plantation	CenW *Pinus radiata*
Indigenous forest	Forest: Other	Biome-BGCMuSo v6.1 evergreen broadleaf forest (EBF)
Cropland	Cropland	Set to non-existing*
Freshwater vegetation	Bare or Lightly-vegetated Surfaces	Set to zero*
Saline vegetation	Bare or Lightly-vegetated Surfaces	Set to zero*
No vegetation	Bare or Lightly-vegetated Surfaces	Set to zero*
Urban	Artificial Surfaces	Set to zero*
Water	Water Bodies	Set to zero*

*Note these categories at not modelled in Biome-BGCMuSo hence we assign a zero flux or set it as non-existing (NaN)

Table S3. Total area of each region and land type proportion in %

Region	Artificial Surfaces	Bare or Lightly vegetated Surfaces	Water Bodies	Cropland	Grassland: Dairy pasture	Grassland: Sheep/Beef pasture	Grassland: Other	Scrub and Shrubland	Forest Plantation	Forest Other	Area (m2)	Area (ha)
1	0.12	0.37	0.0	0.0	7.27	34.61	0.12	3.45	7.64	11.21	2052907261~~1.63~~20529072611	205290~~7.26~~2052
2	3.51	0.15	0.15	0.15	11.11	28.95	0.44	2.63	3.51	11.4	167~~8088735~~6.7716780887356	167~~8088.74~~1678
3	0.38	0.26	3.33	0.51	24.87	38.08	0.0	0.13	4.62	17.95	190~~7230020~~2.8719072300202	190~~7230.02~~1907
4	0.48	0.0	3.85	0.0	20.19	21.63	0.0	0.48	42.79	10.58	504~~9118787~~.615049118787	504~~911.88~~5049
5	0.24	0.49	0.57	0.49	1.38	27.12	1.79	4.07	15.72	34.36	297~~8444837~~.3729778444837	297~~7844.48~~2977
6	0.25	0.0	0.0	0.0	14.32	26.76	0.75	0.5	2.64	34.42	190~~7014479~~4.5619070144794	190~~7014.48~~1907
7	0.52	0.0	0.26	1.03	4.48	63.45	1.12	3.79	3.53	11.64	272~~9652360~~0.7927296523600	272~~9652.36~~2729
8	4.63	0.0	0.46	0.0	0.46	12.5	0.46	8.33	0.46	15.74	507~~5744524~~.945075744524	507~~574.45~~5075
9	0.16	1.18	0.08	0.39	2.51	5.25	3.84	0.94	5.56	63.32	2950~~5096893~~.6329505096893	2950~~509.69~~2950
10	0.87	2.51	0.29	2.22	1.74	47.68	14.86	5.79	2.22	7.14	2355~~4739296~~.9623554739296	2355~~473.93~~2355
11	0.0	20.02	0.43	0.0	2.6	6.82	13.96	1.62	0.65	41.88	208~~9552802~~8.2920895528028	208~~9552.8~~2089
12	0.08	1.93	2.17	5.39	8.04	62.3	11.74	0.24	0.88	0.64	276~~2971790~~9.8327629717909	276~~2971.79~~2762
13	0.0	2.43	2.0	0.0	0.3	13.17	17.05	1.7	0.42	41.81	357~~8873344~~4.4335788733444	357~~8873.34~~3578
14	0.0	0.34	6.08	0.0	0.34	80.07	11.82	0.0	0.0	1.35	652~~3169736~~.956523169736	652~~316.97~~6523
15	0.14	0.42	0.07	0.0	6.57	68.86	4.87	0.42	4.31	4.31	305~~1083573~~6.2630510835736	305~~1083.57~~3051

S5 ~~S6~~ S5 Lateral transport and fjords

Lateral transport, erosion and deposition of organic material can be very important in montane regions and other steeplands when accompanied by rapid re-establishment of productive vegetation on the disturbed landscape (Stallard, 1998; Berhe et al., 2018). Episodic events associated with precipitation and tectonic activity induce landslides in the Fiordland/West Coast regions. Quantification of sediment flux from landslides(Hovius et al., 1997) has not been extended to carbon, but could be substantial (Bianchi et al., 2020). However, these processes would not account for similar sink sizes in flatter land with lower rainfall, e.g., Southland. Globally, fjords such as those found on the southwest coast of New Zealand are known to be hotspots for organic carbon buria (Smith et al., 2015). We observe that regions such as Fiordland and Westland (Southern Alps) provide ideal conditions for erosion and burial as net carbon sinks, expanding on other published work (Scott et al., 2006; Dymond, 2010). A critical pre-conditioning of the sink potential is provided by the rapid colonisation of disturbed landslides and debris by the prolific nitrogen-fixer Coriaria arborea. This species dominates for as long 20-30 years after disturbance, with nitrogen-fixation estimates ranking among the highest observed internationally (Silvester, 1976). Rapid nitrogen accumulation is expected to drive optimal photosynthetic rates in Fiordland's and Westland's cool, year-round maritime climate (Silvester, 1976), which are known to exceed those used historically in successional models of New Zealand forest (Hall, 2001). Models such as Biome-BGCMuSo can account for nitrogen fixation and elevated nitrogen levels but our simulations do not include land disturbance and the succession of nitrogen-fixing grasses to mature forest. This leads to a potential bias in carbon fluxes in disturbed landscapes, missing the rapid accumulation of carbon accompanied by burial. The erosion processes are highly non-linear, requiring special treatment. Nevertheless, hydrologic scaling models (Scott et al., 2006) or fractal landslide models for erosion rates (Hovius et al., 1997) could enable correction terms to be incorporated into priors used for Observing System Simulation Experiment (OSSE) or final estimation in future studies.

Lateral transport of carbon in rivers in the form of dissolved organic carbon (DOC), dissolved inorganic carbon (DIC), and particulate organic carbon (POC) can be substantial (Lauerwald et al., 2023). The flux of DOC from any land area can represent a localised carbon sink from the atmospheric perspective but may be neutralised if respired following hydrologic transfers to downstream environments. While a substantial amount of CO_2 is emitted to the atmosphere during transport (Lauerwald et al., 2023), some of this carbon is exported to coastal systems and the ocean. The recent Australasia regional carbon budget assessment Villalobos et al. (2023) estimated that rivers over the whole of New Zealand transport on average 5.5 ± 2.6 Tg CO_2 yr^{-1} of DOC, 4 ± 2.2 Tg CO_2 yr^{-1} POC and 5.1 ± 2.6 Tg CO_2 yr^{-1} DIC (including the flux from weathering) to estuaries and coastal wetlands. The same study estimated a net flux of 2.2 ± 1.1 Tg CO_2 yr^{-1} from New Zealand's rivers to the atmosphere. After further exchange with the atmosphere through coastal vegetation and estuaries, 8.8 ± 15.4 Tg CO_2 yr^{-1} eventually makes its way to the continental shelves in the ocean. This is not spread evenly over all regions, as some regions have more river surface area than others, and fluxes in individual catchments and different environments can vary widely. Other studies have estimated that riverine export of DOC and POC is significant at 4 ± 1.1 Tg CO_2 yr^{-1} and 9.9 ± 3.6 Tg CO_2 yr^{-1} (Scott et al., 2006), and the majority of this export is happening along the South Island's West Coast, Southern Alps and Fiordland (Scott et al., 2006; McGroddy et al., 2008; Dymond, 2010), including certain regions where our results indicate stronger CO_2

removal from the atmosphere (Fiordland region -39 $\pm$ 10 Tg CO_2 yr^{-1}, Fig. 910). These studies suggest topography, drainage, vegetation type, and lithology are important controls and agree adequately with intensive catchment scale studies (Moore, 1989).

Fjords and other coastal ecosystems are thought to be overall global carbon sinks. In particular, fjords are important sinks, absorbing much more carbon per unit area than other coastal and estuarine environments. Globally, fjords comprise about 0.1% of the ocean surface area and account for 11% of carbon sequestered into ocean sediment (Smith et al., 2015). The sparse data suggest that Fiordland's fjords have some of the highest carbon sequestration rates of any fjords globally (Bianchi et al., 2020). Using global median estimates (-0.12 kg CO_2 m^{-2} yr^{-1}, Rosentreter et al. (2023)) and an estimated total surface area of 779 km^2, New Zealand's fjords are a sink of -0.097 Tg CO_2 yr^{-1} (Rosentreter et al., 2023; Villalobos et al., 2023). This would only explain a very small portion of the sink that we infer from the inversion. However, the global average is partly derived from measurements taken at high latitudes in Europe and North America, where fjords are mostly or entirely glaciated. There is evidence that New Zealand fjords have high rates of organic carbon burial (Ramirez et al., 2016) relative to glaciated fjords in other parts of the world due to vegetation, temperate climate and frequent, heavy rainfall. We expect that CO_2 fluxes from New Zealand's fjords would be at the higher end of the range of that observed globally, but more local observations are needed to verify this, and the bottom-up CO_2 uptake (Rosentreter et al., 2023; Villalobos et al., 2023) would have to be an order of magnitude greater to make a 5% contribution to the observed sink in Fiordland.

Table S4. Annual prior and posterior regional flux estimates with uncertainties and 2011-2020 average values in units of Tg CO_2 yr^{-1}.

	Prior											Post										
Region	2011	2012	2013	2014	2015	2016	2017	2018	2019	2020	2011-2020	2011	2012	2013	2014	2015	2016	2017	2018	2019	2020	2011-2020
Fluxes																						
1	-13.71	-10.95	-4.85	-11.78	-9.01	-12.29	-7.04	-11.75	-8.74	-4.08	-9.42	-12.25	-9.86	-4.04	-11.89	-7.97	-9.4	-6.74	-12.58	-7.55	-4.09	-8.64
2	-8.05	-6.89	-2.83	-7.43	-4.53	-5.55	-3.06	-6.74	-6.17	-2.11	-5.34	-6.38	-5.45	-2.21	-7.14	-3.54	-2.99	-2.43	-6.33	-5.16	-1.97	-4.36
3	-11.78	-12.09	-5.61	-8.36	-7.01	-9.28	-7.5	-10.47	-10.45	-6.68	-8.92	-4.76	-7.75	-3.97	-8.49	1.05	-0.1	-6.88	-9.11	-12.16	-9.35	-6.15
4	-11.07	-11.48	-10.1	-10.92	-9.86	-10.47	-9.97	-10.69	-10.69	-9.35	-10.46	-10.5	-11.17	-9.87	-10.67	-9.63	-10.09	-9.96	-10.39	-10.97	-9.5	-10.28
5	-26.56	-32.51	-27.43	-31.02	-27.08	-26.8	-27.34	-27.82	-28.38	-27.46	-28.24	-22.94	-28.47	-26.51	-29.85	-21.11	-22.04	-25.77	-18.62	-28.87	-30.48	-25.47
6	-8.57	-9.48	-6.72	-4.45	-3.6	-4.01	-6.08	-4.95	-7.6	-5.24	-6.07	1.4	-2.02	-1.63	-1.58	10.74	4.03	-1.93	-4.67	-8.55	-1.58	-0.58
7	-9.0	-10.74	-5.96	-10.75	-1.17	-8.4	-9.6	-9.65	-12.14	-2.78	-8.02	0.92	-6.95	-3.72	-6.36	3.0	-2.43	-4.47	-6.4	-12.65	-6.43	-4.55
8	-0.62	-1.06	-0.41	-1.05	-0.27	-0.26	-0.75	-0.35	-0.57	-0.03	-0.54	0.06	0.05	-0.46	-1.29	-0.03	0.76	0.66	0.38	-0.18	-0.43	-0.05
9	-21.36	-20.1	-17.41	-12.83	-9.39	-10.81	-17.91	-12.59	-11.99	-15.19	-14.96	-32.34	-28.07	-19.83	-25.35	-24.61	-25.58	-31.68	-23.94	-23.39	-18.81	-25.36
10	-4.68	-3.92	-1.91	-1.56	4.49	-4.55	-2.92	-7.41	-2.3	-2.94	-2.77	4.29	2.98	3.17	1.22	5.24	-2.58	-1.95	0.63	8.49	-0.81	2.07
11	-8.69	-8.64	-7.34	-2.78	-6.13	-4.26	-6.93	-2.44	-0.81	-3.84	-5.19	-18.37	-11.15	-9.01	-4.08	-7.52	-13.9	-15.54	-8.39	-14.6	-12.0	-11.46
12	-11.4	-4.19	-1.79	-1.16	3.08	-10.81	-3.27	-7.46	-3.58	-6.12	-4.67	-12.01	-5.21	0.0	-4.54	3.75	-9.67	-11.52	-5.75	-2.02	-11.37	-5.83
13	-8.22	-9.46	-7.41	-0.41	-4.06	-2.47	-6.85	4.54	1.98	-3.95	-3.63	-53.38	-32.04	-22.73	-36.09	-36.92	-53.88	-52.13	-40.76	-32.56	-28.48	-38.9
14	-3.2	-0.44	-0.23	0.94	0.03	-1.49	-0.23	-0.26	-1.29	-0.86	-0.7	-9.75	-6.48	-4.71	-6.69	-4.43	-7.83	-6.73	-9.84	-8.79	-6.18	-7.14
15	-14.59	-8.42	-8.7	-9.22	-3.41	-10.38	-11.17	-7.44	-11.71	-10.39	-9.54	-23.9	-8.47	-15.69	-36.07	-26.89	-23.45	-28.48	-38.95	-17.73	-23.47	-24.31
Uncertainties																						
1	5.43	5.34	5.16	5.19	5.24	5.56	5.32	5.52	5.44	5.11	5.33	5.37	5.3	5.12	5.16	5.19	5.47	5.26	5.4	5.25	5.05	5.26
2	4.27	4.15	4.07	4.06	4.04	4.19	4.05	4.16	4.15	3.88	4.1	4.2	4.1	4.03	4.02	3.99	4.13	4.0	4.05	4.06	3.79	4.04
3	6.6	6.43	6.4	6.17	6.21	6.45	6.37	6.46	6.48	6.26	6.38	6.32	6.13	6.23	5.85	6.01	6.14	6.15	6.12	6.08	5.77	6.08
4	2.25	2.19	2.17	2.16	2.12	2.2	2.16	2.21	2.21	2.12	2.18	2.2	2.16	2.14	2.12	2.06	2.16	2.1	2.17	2.16	2.07	2.13
5	12.71	12.25	12.51	12.19	12.15	12.45	12.4	12.52	12.56	12.36	12.41	12.38	11.91	12.22	11.86	11.82	11.96	11.86	11.89	12.05	11.88	11.98
6	7.62	7.29	7.55	7.03	7.03	7.15	7.07	7.05	7.19	6.98	7.2	6.54	6.65	6.83	6.47	6.48	6.39	5.94	5.87	5.94	5.3	6.24
7	8.36	8.17	8.23	7.92	7.7	8.02	8.09	8.21	8.21	7.86	8.08	7.47	7.06	7.45	7.42	7.3	6.91	7.03	6.68	7.22	6.67	7.12
8	1.2	1.19	1.24	1.19	1.14	1.18	1.17	1.19	1.18	1.15	1.18	1.02	1.04	1.08	0.93	0.8	0.85	0.82	0.85	0.89	0.82	0.91
9	14.38	13.66	13.8	12.7	12.55	12.86	12.82	12.92	12.55	12.73	13.1	11.0	10.14	10.25	10.72	10.68	9.22	8.39	8.84	7.81	8.45	9.55
10	6.32	6.13	6.29	5.82	5.36	5.85	5.88	6.29	6.01	5.86	5.98	5.67	5.6	5.86	5.55	4.99	5.51	5.37	5.93	5.56	5.33	5.54
11	6.93	6.82	6.89	6.19	6.39	6.3	6.18	6.07	5.77	5.87	6.34	6.16	5.85	6.4	5.06	5.2	5.26	5.0	5.32	4.98	5.0	5.42
12	6.23	5.92	5.8	5.38	5.02	5.89	5.76	6.46	5.98	5.69	5.81	5.24	5.24	5.44	5.06	4.6	5.5	5.12	5.8	5.49	5.04	5.25
13	13.03	12.63	12.8	11.53	11.68	11.45	11.15	10.7	10.34	10.6	11.59	11.1	10.08	11.43	8.38	8.88	9.03	8.16	8.7	8.0	7.79	9.15
14	1.65	1.5	1.46	1.32	1.31	1.46	1.39	1.54	1.51	1.46	1.46	0.87	0.88	1.08	0.93	1.03	0.98	0.91	1.0	0.96	0.88	0.95
15	9.08	8.64	8.64	8.53	8.26	8.6	8.62	8.94	8.87	8.72	8.69	6.78	7.12	7.44	6.98	6.89	6.62	6.34	6.93	6.34	5.92	6.74

Table S5. Annual prior and posterior regional flux estimates with uncertainties and 2011-2020 average values in units of t C ha^{-1} yr^{-1}.

	Prior											Post										
Region	2011	2012	2013	2014	2015	2016	2017	2018	2019	2020	2011-2020	2011	2012	2013	2014	2015	2016	2017	2018	2019	2020	2011-2020
Fluxes																						
1	-1.82	-1.45	-0.64	-1.56	-1.2	-1.63	-0.94	-1.56	-1.16	-0.54	-1.25	-1.63	-1.31	-0.54	-1.58	-1.06	-1.25	-0.9	-1.67	-1.0	-0.54	-1.15
2	-1.31	-1.12	-0.46	-1.21	-0.74	-0.9	-0.5	-1.1	-1.0	-0.34	-0.87	-1.04	-0.89	-0.36	-1.16	-0.58	-0.49	-0.39	-1.03	-0.84	-0.32	-0.71
3	-1.68	-1.73	-0.8	-1.2	-1.0	-1.33	-1.07	-1.5	-1.49	-0.95	-1.28	-0.68	-1.11	-0.57	-1.21	0.15	-0.01	-0.98	-1.3	-1.74	-1.34	-0.88
4	-5.98	-6.2	-5.46	-5.9	-5.32	-5.65	-5.38	-5.77	-5.78	-5.05	-5.65	-5.67	-6.03	-5.33	-5.76	-5.2	-5.45	-5.38	-5.61	-5.92	-5.13	-5.55
5	-2.43	-2.98	-2.51	-2.84	-2.48	-2.45	-2.5	-2.55	-2.6	-2.51	-2.59	-2.1	-2.61	-2.43	-2.73	-1.93	-2.02	-2.36	-1.71	-2.64	-2.79	-2.33
6	-1.23	-1.36	-0.96	-0.64	-0.51	-0.57	-0.87	-0.71	-1.09	-0.75	-0.87	0.2	-0.29	-0.23	-0.23	1.54	0.58	-0.28	-0.67	-1.22	-0.23	-0.08
7	-0.9	-1.07	-0.6	-1.07	-0.12	-0.84	-0.96	-0.96	-1.21	-0.28	-0.8	0.09	-0.69	-0.37	-0.64	0.3	-0.24	-0.45	-0.64	-1.26	-0.64	-0.45
8	-0.34	-0.57	-0.22	-0.57	-0.15	-0.14	-0.4	-0.19	-0.31	-0.01	-0.29	0.03	0.03	-0.25	-0.7	-0.01	0.41	0.35	0.2	-0.1	-0.23	-0.03
9	-1.97	-1.86	-1.61	-1.19	-0.87	-1.0	-1.66	-1.16	-1.11	-1.4	-1.38	-2.99	-2.59	-1.83	-2.34	-2.27	-2.36	-2.93	-2.21	-2.16	-1.74	-2.34
10	-0.54	-0.45	-0.22	-0.18	0.52	-0.53	-0.34	-0.86	-0.27	-0.34	-0.32	0.5	0.35	0.37	0.14	0.61	-0.3	-0.23	0.07	0.98	-0.09	0.24
11	-1.13	-1.13	-0.96	-0.36	-0.8	-0.56	-0.9	-0.32	-0.11	-0.5	-0.68	-2.4	-1.45	-1.18	-0.53	-0.98	-1.81	-2.03	-1.1	-1.91	-1.57	-1.5
12	-1.12	-0.41	-0.18	-0.11	0.3	-1.07	-0.32	-0.74	-0.35	-0.6	-0.46	-1.19	-0.51	0.0	-0.45	0.37	-0.95	-1.14	-0.57	-0.2	-1.12	-0.58
13	-0.63	-0.72	-0.56	-0.03	-0.31	-0.19	-0.52	0.35	0.15	-0.3	-0.28	-4.07	-2.44	-1.73	-2.75	-2.81	-4.11	-3.97	-3.11	-2.48	-2.17	-2.96
14	-1.34	-0.18	-0.1	0.39	0.01	-0.62	-0.1	-0.11	-0.54	-0.36	-0.29	-4.08	-2.71	-1.97	-2.8	-1.85	-3.28	-2.81	-4.11	-3.68	-2.58	-2.99
15	-1.3	-0.75	-0.78	-0.82	-0.3	-0.93	-1.0	-0.66	-1.05	-0.93	-0.85	-2.14	-0.76	-1.4	-3.22	-2.4	-2.1	-2.55	-3.48	-1.59	-2.1	-2.17
Uncertainties																						
1	0.72	0.71	0.69	0.69	0.7	0.74	0.71	0.73	0.72	0.68	0.71	0.71	0.7	0.68	0.69	0.69	0.73	0.7	0.72	0.7	0.67	0.7
2	0.69	0.67	0.66	0.66	0.66	0.68	0.66	0.68	0.67	0.63	0.67	0.68	0.67	0.65	0.65	0.65	0.67	0.65	0.66	0.66	0.62	0.66
3	0.94	0.92	0.92	0.88	0.89	0.92	0.91	0.92	0.93	0.9	0.91	0.9	0.88	0.89	0.84	0.86	0.88	0.88	0.87	0.87	0.82	0.87
4	1.21	1.19	1.17	1.17	1.14	1.19	1.17	1.19	1.19	1.14	1.18	1.19	1.17	1.15	1.15	1.11	1.17	1.14	1.17	1.17	1.12	1.15
5	1.16	1.12	1.15	1.12	1.11	1.14	1.14	1.15	1.15	1.13	1.14	1.13	1.09	1.12	1.09	1.08	1.1	1.09	1.09	1.1	1.09	1.1
6	1.09	1.04	1.08	1.0	1.01	1.02	1.01	1.01	1.03	1.0	1.03	0.94	0.95	0.98	0.93	0.93	0.91	0.85	0.84	0.85	0.76	0.89
7	0.84	0.82	0.82	0.79	0.77	0.8	0.81	0.82	0.82	0.79	0.81	0.75	0.71	0.74	0.74	0.73	0.69	0.7	0.67	0.72	0.67	0.71
8	0.64	0.64	0.66	0.64	0.61	0.63	0.63	0.64	0.64	0.62	0.63	0.55	0.56	0.58	0.5	0.43	0.46	0.44	0.46	0.48	0.44	0.49
9	1.33	1.26	1.28	1.17	1.16	1.19	1.19	1.19	1.16	1.18	1.21	1.02	0.94	0.95	0.99	0.99	0.85	0.78	0.82	0.72	0.78	0.88
10	0.73	0.71	0.73	0.67	0.62	0.68	0.68	0.73	0.7	0.68	0.69	0.66	0.65	0.68	0.64	0.58	0.64	0.62	0.69	0.64	0.62	0.64
11	0.9	0.89	0.9	0.81	0.83	0.82	0.81	0.79	0.75	0.77	0.83	0.8	0.76	0.83	0.66	0.68	0.69	0.65	0.69	0.65	0.65	0.71
12	0.61	0.58	0.57	0.53	0.5	0.58	0.57	0.64	0.59	0.56	0.57	0.52	0.52	0.54	0.5	0.45	0.54	0.51	0.57	0.54	0.5	0.52
13	0.99	0.96	0.98	0.88	0.89	0.87	0.85	0.82	0.79	0.81	0.88	0.85	0.77	0.87	0.64	0.68	0.69	0.62	0.66	0.61	0.59	0.7
14	0.69	0.63	0.61	0.55	0.55	0.61	0.58	0.65	0.63	0.61	0.61	0.36	0.37	0.45	0.39	0.43	0.41	0.38	0.42	0.4	0.37	0.4
15	0.81	0.77	0.77	0.76	0.74	0.77	0.77	0.8	0.79	0.78	0.78	0.61	0.64	0.66	0.62	0.62	0.59	0.57	0.62	0.57	0.53	0.6

Table S6. Annual prior and posterior regional flux estimates with uncertainties and 2011-2020 average values in units of g C m^{-2} yr^{-1}.

	Prior											Post										
Region	2011	2012	2013	2014	2015	2016	2017	2018	2019	2020	2011-2020	2011	2012	2013	2014	2015	2016	2017	2018	2019	2020	2011-2020
Fluxes																						
1	-182.14	-145.41	-64.38	-156.47	-119.74	-163.24	-93.59	-156.13	-116.13	-54.24	-125.15	-162.71	-131.02	-53.62	-157.9	-105.85	-124.91	-89.59	-167.14	-100.28	-54.37	-114.74
2	-130.91	-111.96	-46.07	-120.74	-73.58	-90.19	-49.66	-109.5	-100.26	-34.29	-86.72	-103.68	-88.57	-35.93	-116.07	-57.5	-48.54	-39.49	-102.82	-83.84	-32.09	-70.85
3	-168.45	-172.81	-80.17	-119.58	-100.27	-132.71	-107.32	-149.71	-149.48	-95.49	-127.6	-68.13	-110.88	-56.81	-121.42	15.05	-1.38	-98.42	-130.3	-173.9	-133.73	-87.99
4	-597.98	-619.91	-545.69	-589.82	-532.47	-565.28	-538.49	-577.46	-577.59	-504.9	-564.96	-567.21	-603.2	-533.39	-576.24	-520.06	-544.93	-538.21	-561.32	-592.48	-513.06	-555.01
5	-243.22	-297.74	-251.26	-284.14	-248.02	-245.48	-250.35	-254.82	-259.88	-251.45	-258.64	-210.11	-260.7	-242.83	-273.39	-193.3	-201.88	-235.99	-170.55	-264.43	-279.19	-233.24
6	-122.52	-135.54	-96.05	-63.67	-51.49	-57.35	-86.94	-70.84	-108.73	-74.93	-86.81	20.08	-28.92	-23.31	-22.54	153.61	57.67	-27.61	-66.81	-122.2	-22.63	-8.27
7	-89.91	-107.33	-59.56	-107.46	-11.67	-83.95	-95.91	-96.38	-121.31	-27.77	-80.12	9.18	-69.44	-37.17	-63.57	29.99	-24.25	-44.68	-63.9	-126.38	-64.28	-45.45
8	-33.56	-57.16	-22.21	-56.6	-14.71	-13.87	-40.14	-18.81	-30.74	-1.48	-28.93	3.2	2.76	-24.56	-69.55	-1.37	40.87	35.33	20.19	-9.79	-23.33	-2.63
9	-197.47	-185.82	-160.95	-118.55	-86.8	-99.91	-165.54	-116.36	-110.81	-140.38	-138.26	-298.97	-259.5	-183.32	-234.31	-227.48	-236.48	-292.85	-221.28	-216.21	-173.84	-234.42
10	-54.15	-45.37	-22.07	-18.01	52.01	-52.63	-33.81	-85.83	-26.58	-34.01	-32.04	49.64	34.54	36.67	14.1	60.62	-29.84	-22.53	7.25	98.24	-9.33	23.94
11	-113.45	-112.81	-95.83	-36.24	-79.95	-55.56	-90.47	-31.8	-10.61	-50.08	-67.68	-239.73	-145.48	-117.61	-53.25	-98.1	-181.46	-202.87	-109.52	-190.6	-156.59	-149.52
12	-112.48	-41.39	-17.69	-11.44	30.38	-106.67	-32.26	-73.62	-35.35	-60.43	-46.1	-118.52	-51.44	0.04	-44.82	37.04	-95.45	-113.69	-56.76	-19.92	-112.23	-57.58
13	-62.66	-72.1	-56.45	-3.1	-30.94	-18.83	-52.19	34.63	15.06	-30.07	-27.66	-406.75	-244.13	-173.23	-275.01	-281.37	-410.58	-397.25	-310.58	-248.1	-217.0	-296.4
14	-133.83	-18.36	-9.52	39.31	1.42	-62.18	-9.57	-11.05	-54.02	-36.1	-29.39	-407.67	-270.99	-197.02	-279.63	-185.19	-327.57	-281.27	-411.42	-367.71	-258.2	-298.67
15	-130.41	-75.27	-77.77	-82.38	-30.49	-92.8	-99.83	-66.46	-104.66	-92.9	-85.3	-213.64	-75.67	-140.21	-322.45	-240.35	-209.64	-254.53	-348.19	-158.52	-209.79	-217.3
Uncertainties																						
1	72.18	70.98	68.6	69.01	69.67	73.82	70.67	73.37	72.32	67.94	70.86	71.35	70.36	68.05	68.51	68.93	72.72	69.94	71.7	69.74	67.12	69.84
2	69.45	67.49	66.14	66.04	65.6	68.09	65.87	67.54	67.47	63.11	66.68	68.22	66.69	65.46	65.38	64.8	67.12	65.03	65.81	66.05	61.57	65.61
3	94.44	91.88	91.53	88.18	88.79	92.29	91.06	92.44	92.73	89.5	91.28	90.38	87.62	89.02	83.69	85.93	87.83	87.94	87.49	86.9	82.48	86.93
4	121.29	118.55	117.45	116.69	114.37	119.03	116.91	119.47	119.29	114.3	117.74	118.71	116.66	115.47	114.68	111.43	116.87	113.52	117.21	116.71	111.54	115.28
5	116.42	112.16	114.57	111.63	111.32	114.02	113.6	114.66	115.02	113.23	113.66	113.41	109.09	111.89	108.62	108.26	109.51	108.59	108.86	110.39	108.81	109.74
6	108.97	104.27	107.94	100.49	100.58	102.25	101.07	100.87	102.86	99.89	102.92	93.6	95.03	97.72	92.53	92.73	91.45	84.88	83.92	85.01	75.76	89.26
7	83.56	81.58	82.21	79.09	76.91	80.12	80.81	82.05	82.06	78.51	80.69	74.59	70.57	74.39	74.11	72.98	68.99	70.21	66.75	72.18	66.6	71.14
8	64.27	63.9	66.41	63.94	61.11	63.17	62.69	63.92	63.65	61.54	63.46	54.78	56.15	58.29	49.81	42.79	45.83	44.13	45.72	47.66	44.04	48.92
9	132.94	126.27	127.53	117.38	116.02	118.87	118.52	119.43	115.96	117.63	121.06	101.68	93.7	94.79	99.11	98.75	85.24	77.58	81.73	72.2	78.12	88.29
10	73.15	70.92	72.87	67.38	62.09	67.72	68.05	72.87	69.58	67.79	69.24	65.68	64.83	67.91	64.3	57.73	63.79	62.15	68.62	64.36	61.72	64.11
11	90.4	89.0	89.99	80.75	83.42	82.26	80.71	79.21	75.32	76.59	82.77	80.45	76.31	83.48	66.0	67.84	68.62	65.23	69.47	65.05	65.3	70.77
12	61.5	58.46	57.28	53.15	49.52	58.16	56.84	63.81	59.04	56.15	57.39	51.76	51.76	53.66	49.98	45.43	54.28	50.55	57.25	54.19	49.76	51.86
13	99.31	96.26	97.56	87.83	89.04	87.25	84.93	81.51	78.77	80.8	88.33	84.58	76.81	87.1	63.83	67.7	68.85	62.2	66.3	60.94	59.33	69.76
14	68.87	62.84	60.88	55.13	54.74	60.91	57.95	64.57	63.23	61.0	61.01	36.44	36.99	45.34	38.7	43.17	40.84	38.19	41.64	40.32	36.79	39.84
15	81.18	77.25	77.26	76.25	73.85	76.88	77.02	79.9	79.28	77.91	77.68	60.64	63.69	66.49	62.37	61.57	59.18	56.63	61.98	56.65	52.88	60.21

Table S7. Annual prior and posterior regional flux estimates with uncertainties and 2011-2020 average values in units of kg CO_2 m^{-2} yr^{-1}.

	Prior											Post										
Region	2011	2012	2013	2014	2015	2016	2017	2018	2019	2020	2011-2020	2011	2012	2013	2014	2015	2016	2017	2018	2019	2020	2011-2020
Fluxes																						
1	-0.67	-0.53	-0.24	-0.57	-0.44	-0.6	-0.34	-0.57	-0.43	-0.2	-0.46	-0.6	-0.48	-0.2	-0.58	-0.39	-0.46	-0.33	-0.61	-0.37	-0.2	-0.42
2	-0.48	-0.41	-0.17	-0.44	-0.27	-0.33	-0.18	-0.4	-0.37	-0.13	-0.32	-0.38	-0.32	-0.13	-0.43	-0.21	-0.18	-0.14	-0.38	-0.31	-0.12	-0.26
3	-0.62	-0.63	-0.29	-0.44	-0.37	-0.49	-0.39	-0.55	-0.55	-0.35	-0.47	-0.25	-0.41	-0.21	-0.45	0.06	-0.01	-0.36	-0.48	-0.64	-0.49	-0.32
4	-2.19	-2.27	-2.0	-2.16	-1.95	-2.07	-1.97	-2.12	-2.12	-1.85	-2.07	-2.08	-2.21	-1.96	-2.11	-1.91	-2.0	-1.97	-2.06	-2.17	-1.88	-2.04
5	-0.89	-1.09	-0.92	-1.04	-0.91	-0.9	-0.92	-0.93	-0.95	-0.92	-0.95	-0.77	-0.96	-0.89	-1.0	-0.71	-0.74	-0.87	-0.63	-0.97	-1.02	-0.86
6	-0.45	-0.5	-0.35	-0.23	-0.19	-0.21	-0.32	-0.26	-0.4	-0.27	-0.32	0.07	-0.11	-0.09	-0.08	0.56	0.21	-0.1	-0.24	-0.45	-0.08	-0.03
7	-0.33	-0.39	-0.22	-0.39	-0.04	-0.31	-0.35	-0.35	-0.44	-0.1	-0.29	0.03	-0.25	-0.14	-0.23	0.11	-0.09	-0.16	-0.23	-0.46	-0.24	-0.17
8	-0.12	-0.21	-0.08	-0.21	-0.05	-0.05	-0.15	-0.07	-0.11	-0.01	-0.11	0.01	0.01	-0.09	-0.26	-0.01	0.15	0.13	0.07	-0.04	-0.09	-0.01
9	-0.72	-0.68	-0.59	-0.43	-0.32	-0.37	-0.61	-0.43	-0.41	-0.51	-0.51	-1.1	-0.95	-0.67	-0.86	-0.83	-0.87	-1.07	-0.81	-0.79	-0.64	-0.86
10	-0.2	-0.17	-0.08	-0.07	0.19	-0.19	-0.12	-0.31	-0.1	-0.12	-0.12	0.18	0.13	0.13	0.05	0.22	-0.11	-0.08	0.03	0.36	-0.03	0.09
11	-0.42	-0.41	-0.35	-0.13	-0.29	-0.2	-0.33	-0.12	-0.04	-0.18	-0.25	-0.88	-0.53	-0.43	-0.2	-0.36	-0.67	-0.74	-0.4	-0.7	-0.57	-0.55
12	-0.41	-0.15	-0.06	-0.04	0.11	-0.39	-0.12	-0.27	-0.13	-0.22	-0.17	-0.43	-0.19	0.0	-0.16	0.14	-0.35	-0.42	-0.21	-0.07	-0.41	-0.21
13	-0.23	-0.26	-0.21	-0.01	-0.11	-0.07	-0.19	0.13	0.06	-0.11	-0.1	-1.49	-0.9	-0.64	-1.01	-1.03	-1.51	-1.46	-1.14	-0.91	-0.8	-1.09
14	-0.49	-0.07	-0.03	0.14	0.01	-0.23	-0.04	-0.04	-0.2	-0.13	-0.11	-1.49	-0.99	-0.72	-1.03	-0.68	-1.2	-1.03	-1.51	-1.35	-0.95	-1.1
15	-0.48	-0.28	-0.29	-0.3	-0.11	-0.34	-0.37	-0.24	-0.38	-0.34	-0.31	-0.78	-0.28	-0.51	-1.18	-0.88	-0.77	-0.93	-1.28	-0.58	-0.77	-0.8
Uncertainties																						
1	0.26	0.26	0.25	0.25	0.26	0.27	0.26	0.27	0.27	0.25	0.26	0.26	0.26	0.25	0.25	0.25	0.27	0.26	0.26	0.26	0.25	0.26
2	0.25	0.25	0.24	0.24	0.24	0.25	0.24	0.25	0.25	0.23	0.24	0.25	0.24	0.24	0.24	0.24	0.25	0.24	0.24	0.24	0.23	0.24
3	0.35	0.34	0.34	0.32	0.33	0.34	0.33	0.34	0.34	0.33	0.33	0.33	0.32	0.33	0.31	0.32	0.32	0.32	0.32	0.32	0.3	0.32
4	0.44	0.43	0.43	0.43	0.42	0.44	0.43	0.44	0.44	0.42	0.43	0.44	0.43	0.42	0.42	0.41	0.43	0.42	0.43	0.43	0.41	0.42
5	0.43	0.41	0.42	0.41	0.41	0.42	0.42	0.42	0.42	0.42	0.42	0.42	0.4	0.41	0.4	0.4	0.4	0.4	0.4	0.4	0.4	0.4
6	0.4	0.38	0.4	0.37	0.37	0.37	0.37	0.37	0.38	0.37	0.38	0.34	0.35	0.36	0.34	0.34	0.34	0.31	0.31	0.31	0.28	0.33
7	0.31	0.3	0.3	0.29	0.28	0.29	0.3	0.3	0.3	0.29	0.3	0.27	0.26	0.27	0.27	0.27	0.25	0.26	0.24	0.26	0.24	0.26
8	0.24	0.23	0.24	0.23	0.22	0.23	0.23	0.23	0.23	0.23	0.23	0.2	0.21	0.21	0.18	0.16	0.17	0.16	0.17	0.17	0.16	0.18
9	0.49	0.46	0.47	0.43	0.43	0.44	0.43	0.44	0.43	0.43	0.44	0.37	0.34	0.35	0.36	0.36	0.31	0.28	0.3	0.26	0.29	0.32
10	0.27	0.26	0.27	0.25	0.23	0.25	0.25	0.27	0.26	0.25	0.25	0.24	0.24	0.25	0.24	0.21	0.23	0.23	0.25	0.24	0.23	0.24
11	0.33	0.33	0.33	0.3	0.31	0.3	0.3	0.29	0.28	0.28	0.3	0.29	0.28	0.31	0.24	0.25	0.25	0.24	0.25	0.24	0.24	0.26
12	0.23	0.21	0.21	0.19	0.18	0.21	0.21	0.23	0.22	0.21	0.21	0.19	0.19	0.2	0.18	0.17	0.2	0.19	0.21	0.2	0.18	0.19
13	0.36	0.35	0.36	0.32	0.33	0.32	0.31	0.3	0.29	0.3	0.32	0.31	0.28	0.32	0.23	0.25	0.25	0.23	0.24	0.22	0.22	0.26
14	0.25	0.23	0.22	0.2	0.2	0.22	0.21	0.24	0.23	0.22	0.22	0.13	0.14	0.17	0.14	0.16	0.15	0.14	0.15	0.15	0.13	0.15
15	0.3	0.28	0.28	0.28	0.27	0.28	0.28	0.29	0.29	0.29	0.28	0.22	0.23	0.24	0.23	0.23	0.22	0.21	0.23	0.21	0.19	0.22

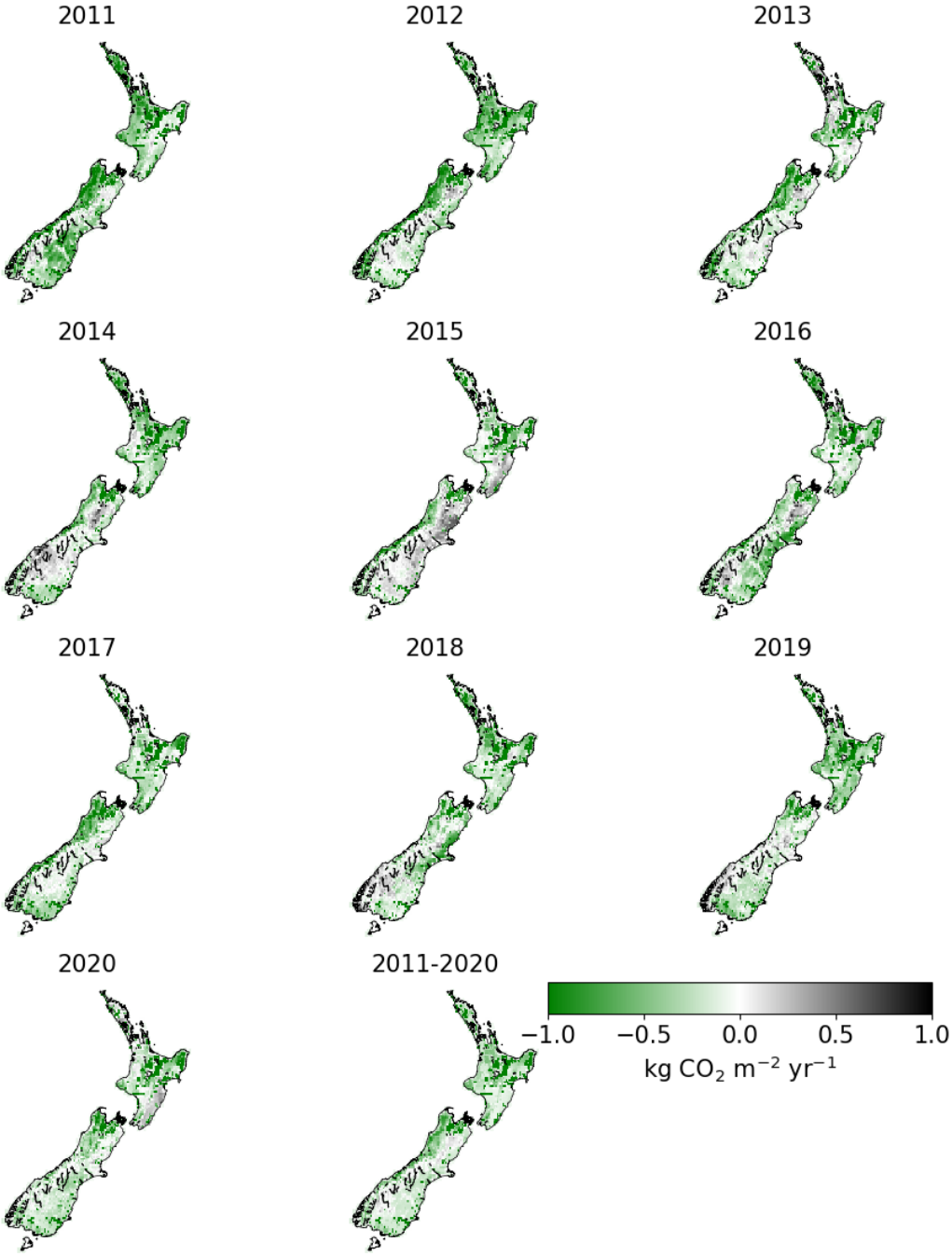

Figure S8. ~~S9~~ S8 Spatial distribution of the prior fluxes averaged for each year between 2011 and 2020.

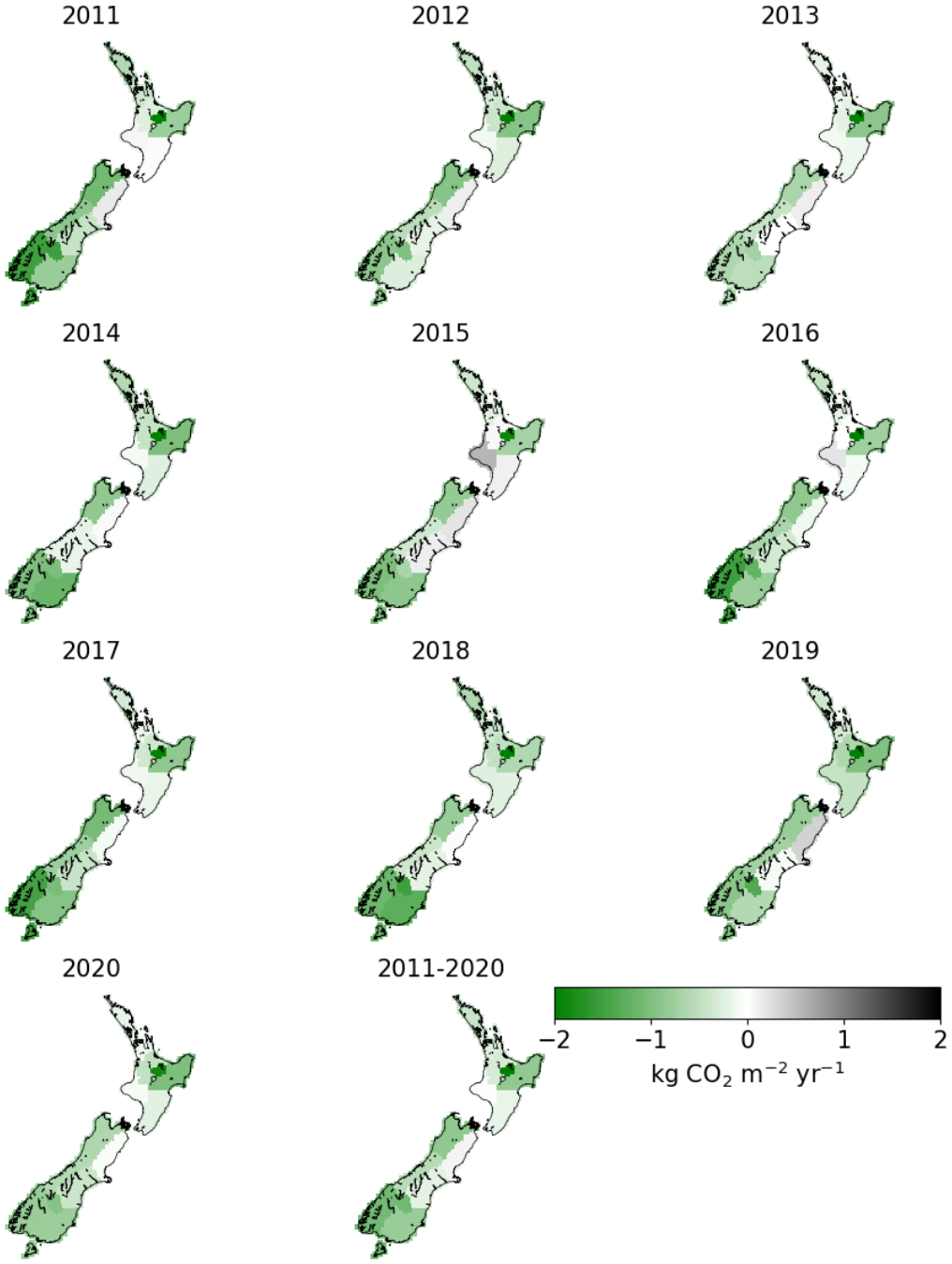

Figure S9. ~~S10~~ S9 Regional posterior fluxes averaged for each year between 2011 and 2020.

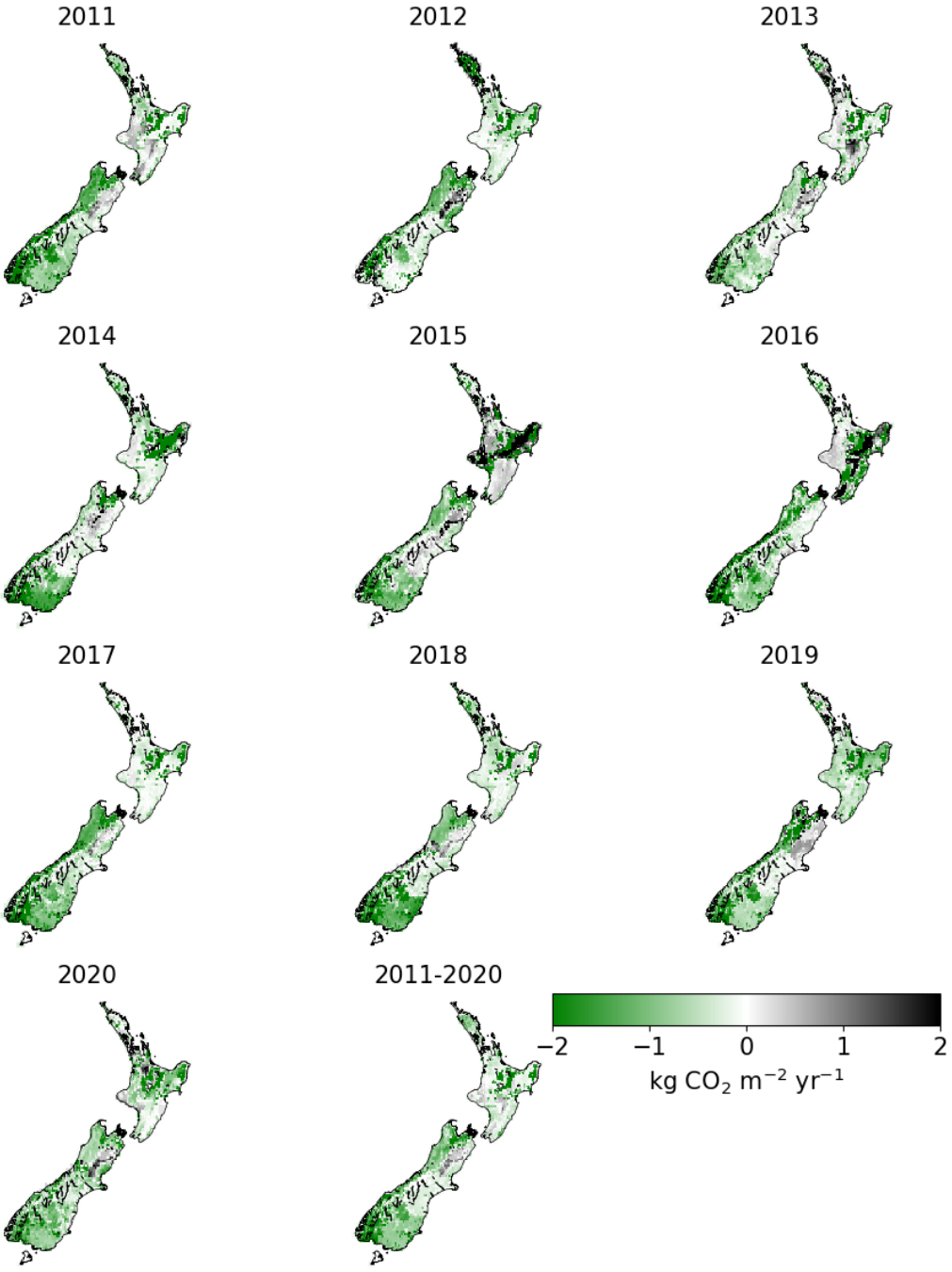

Figure S10. ~~S11~~ S10 Spatial distribution of the posterior fluxes by scaling the prior flux maps with the regional posterior estimates and averaged for each year between 2011 and 2020.

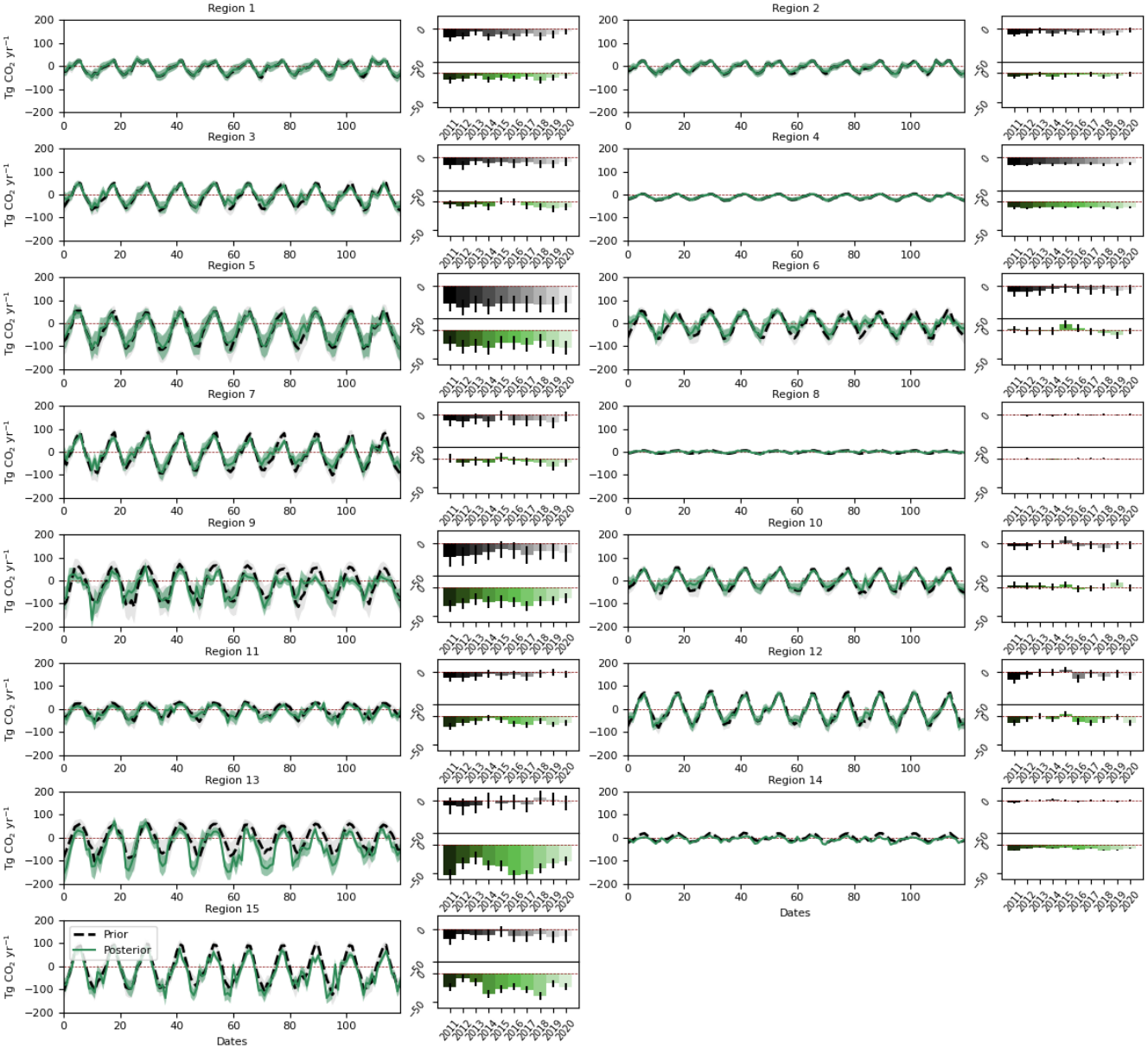

Figure S11. ~~S12~~ S11 Monthly (left) and annual (right) CO_2 prior (black) and posterior (green) net ~~air-land~~ land-to-air flux estimates for all land inversion regions.

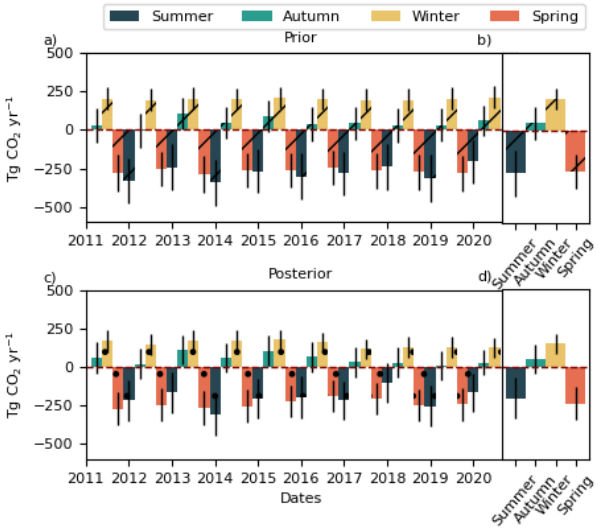

Figure S12. ~~S13~~ S12 Mean North-Island annual seasonal (summer – December to February, autumn – March to May, winter – June to August, spring – September to November) CO_2 prior (a) and posterior (c) net ~~air-land~~ land-to-air flux estimates. Subplots b) and d) show the 2011-2020 average values for each season. The first and last season is removed from the plot and calculation due to insufficient number of months to calculate the seasonal average.

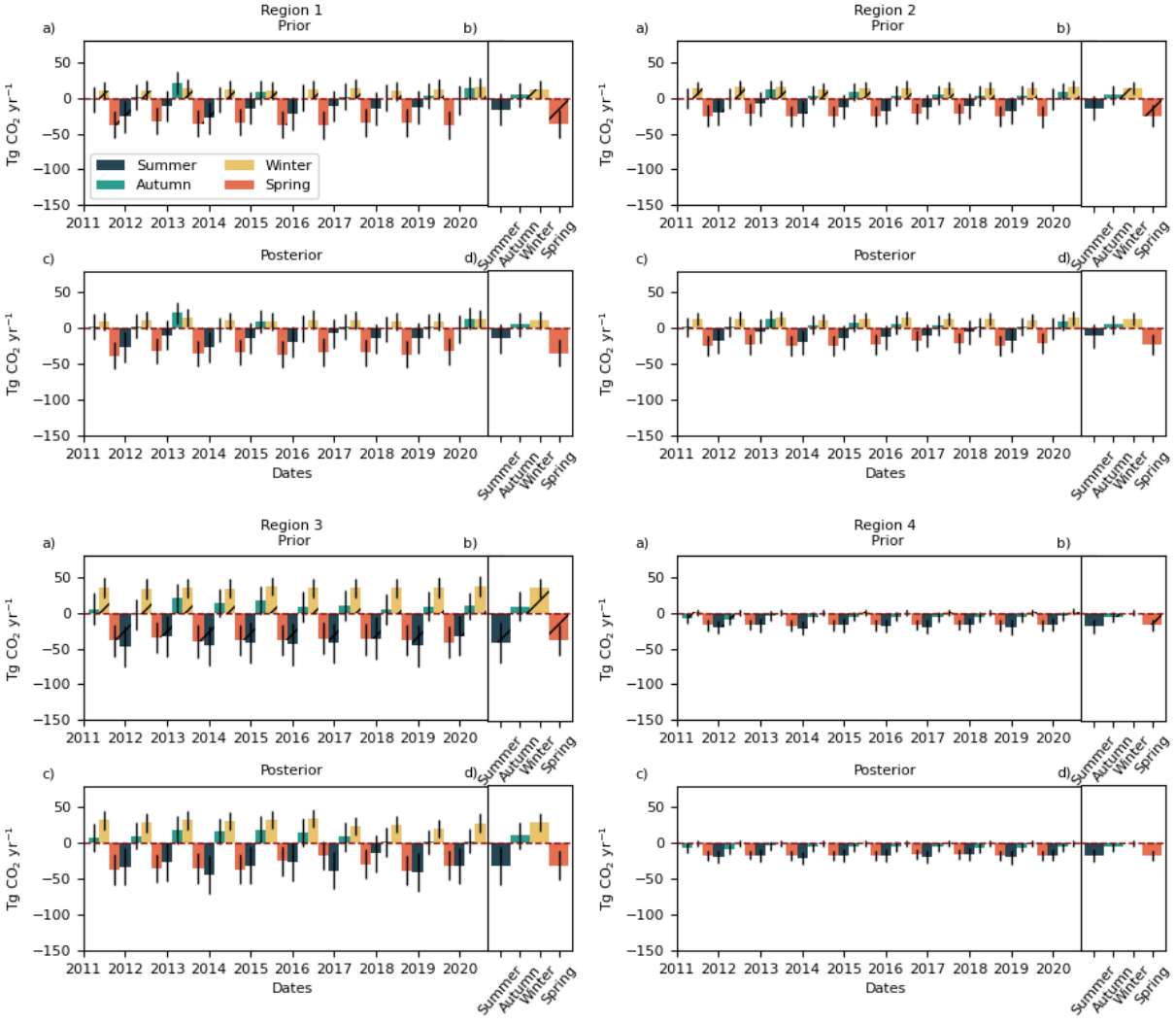

Figure S13. ~~S14~~ S13 Mean annual seasonal (summer – December to February, autumn – March to May, winter – June to August, spring – September to November) CO_2 prior (a) and posterior (c) net ~~air-land~~ land-to-air flux estimates for the land regions. Subplots b) and d) show the 2011-2020 average values for each season. The first and last season is removed from the plot and calculation due to insufficient number of months to calculate the seasonal average.

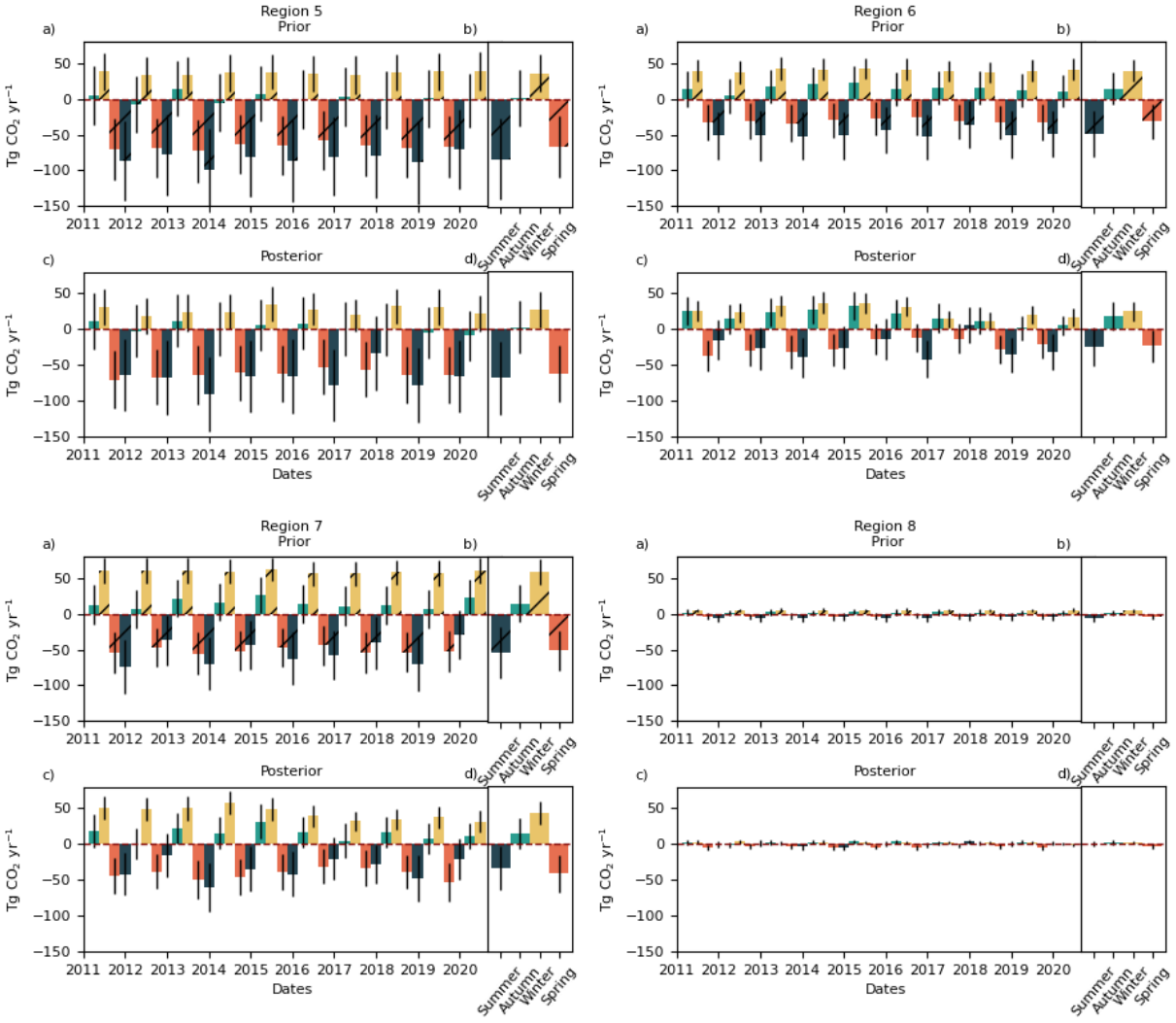

Figure S13. ~~S14~~ S13 Continued.

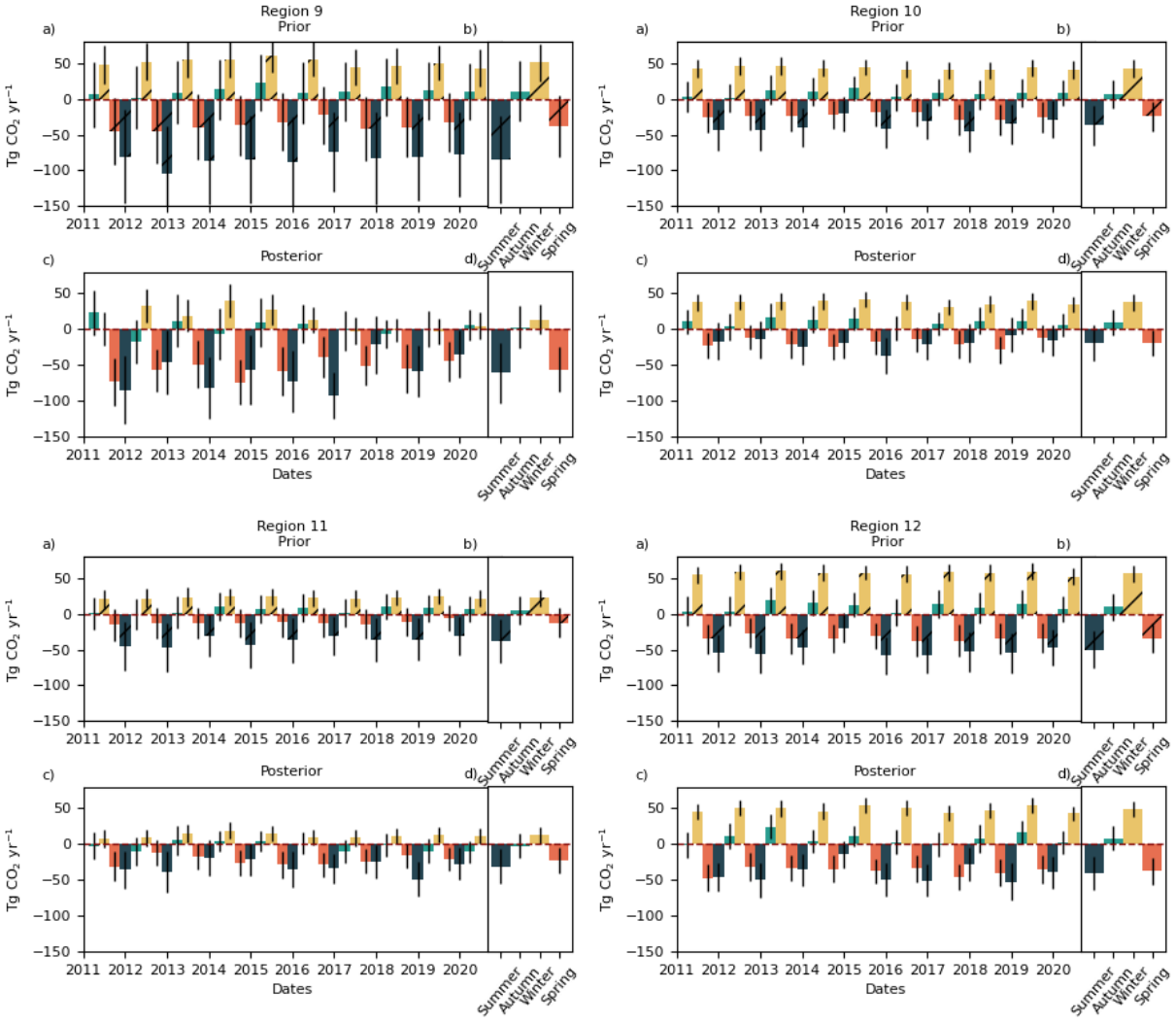

Figure S13. ~~S14~~ S13 Continued.

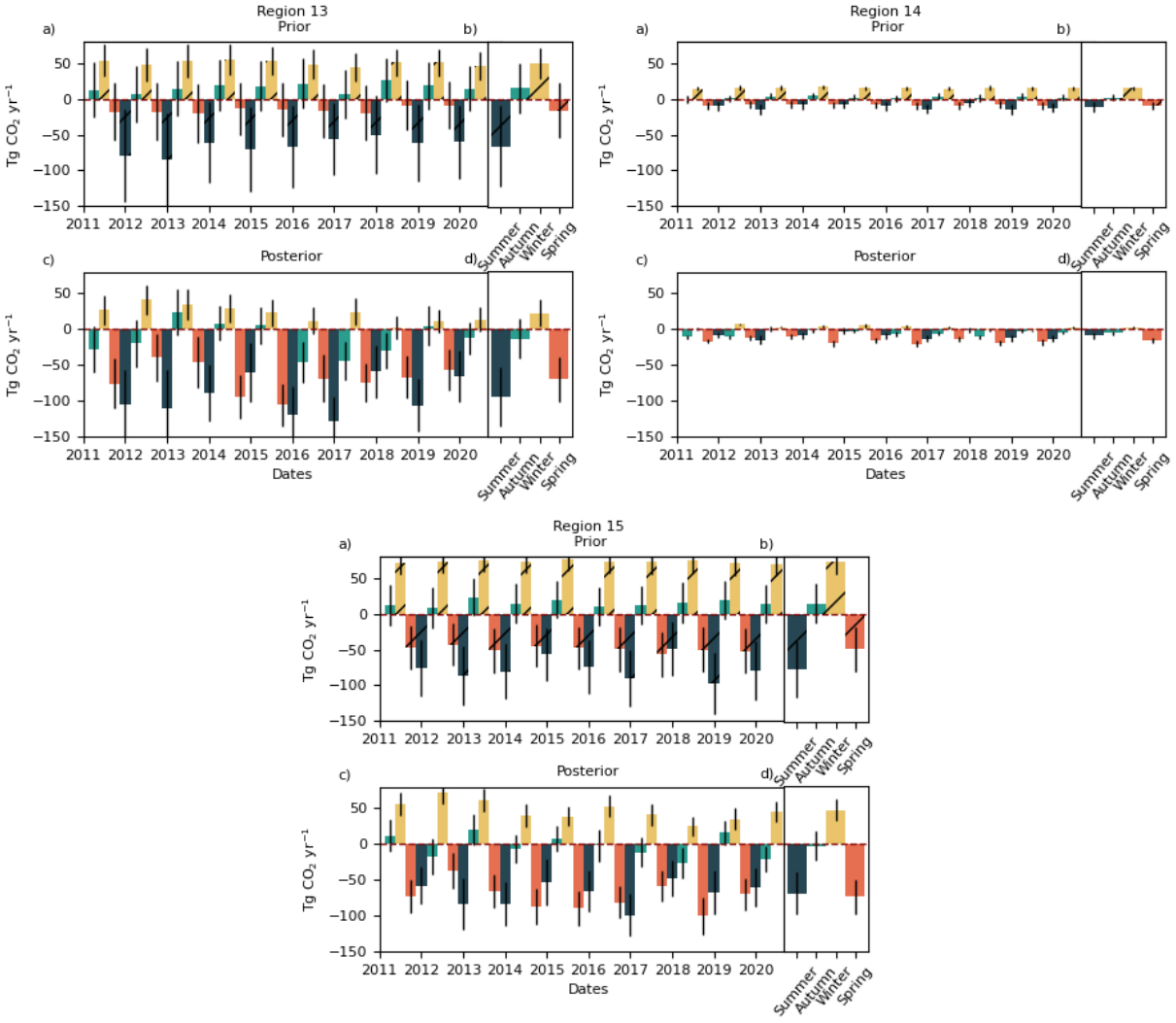

Figure S13. ~~S14~~ S13 Continued.

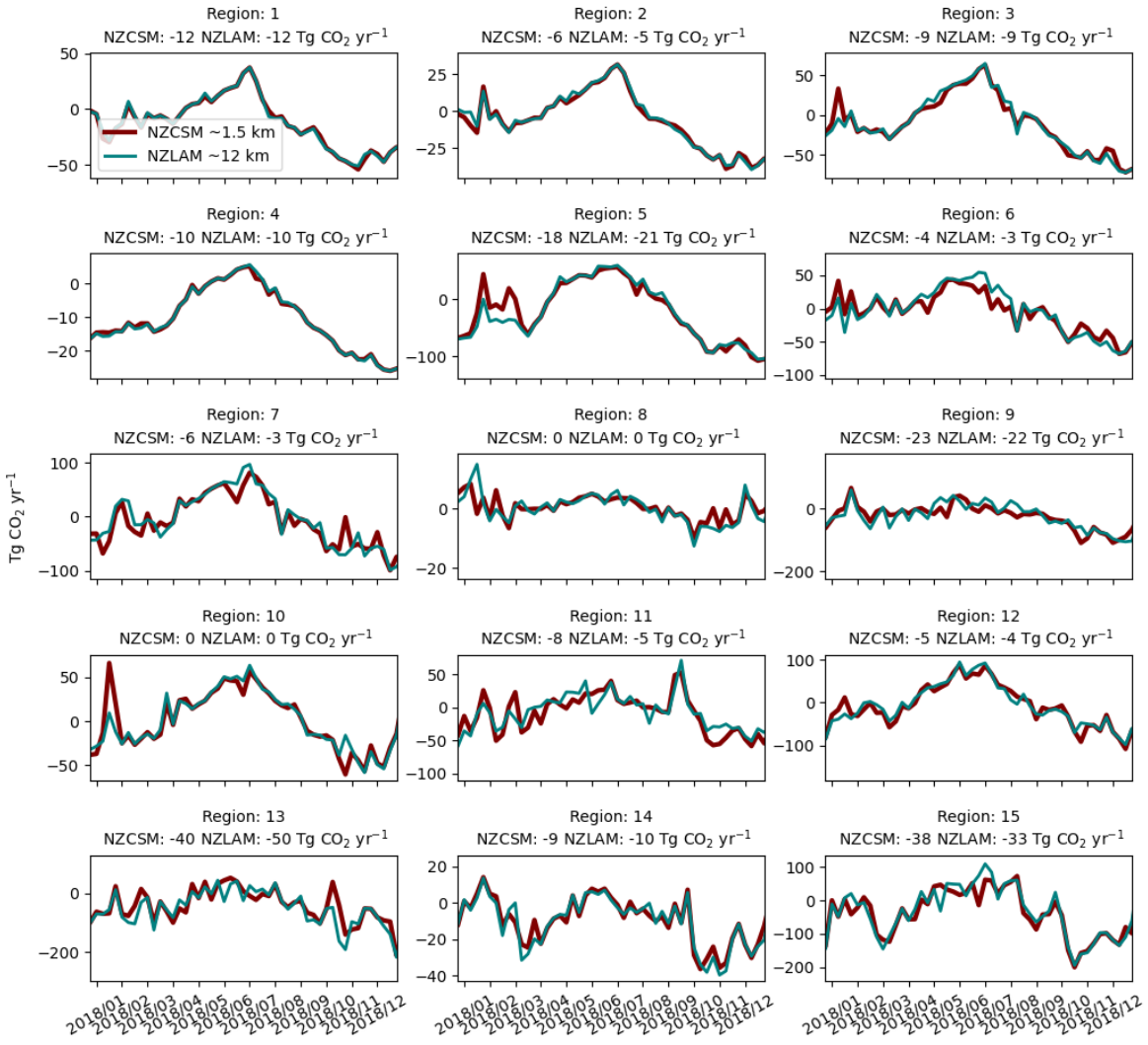

Figure S14. ~~S15~~ S14 Time-series of the transport model sensitivity test for each inversion region.

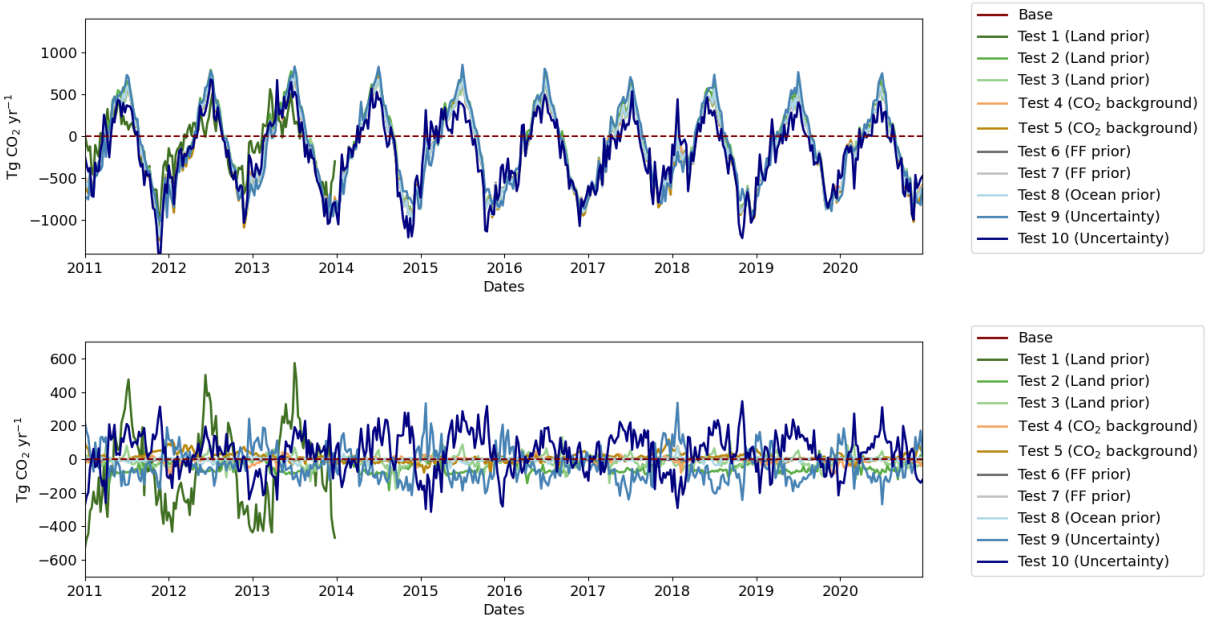

Figure S15. ~~S16~~ S15 Time-series of the sensitivity tests for New Zealand (top plot) and difference relative to the base inversion results (bottom plot). A detailed description of the setup in each test can be found in ~~Tabel~~ Table 3.

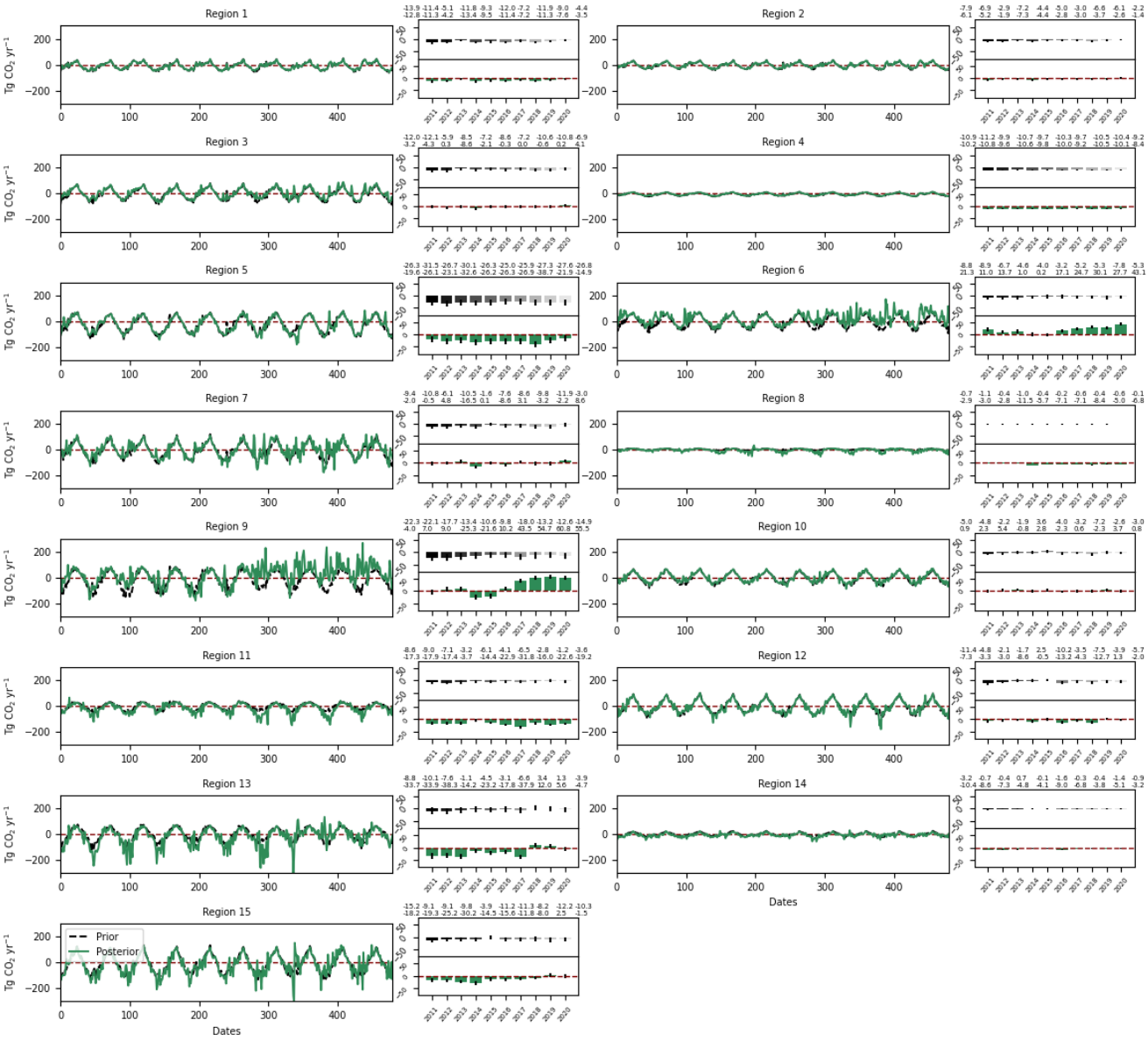

Figure S16. ~~S17~~ S16 Diurnal cycle test results (Section 4.3, main paper) for the land inversion regions. The figure shows the timeseries of prior (black) and posterior (green) fluxes for each land inversion region (i.e., region 1-15), along with corresponding annual values. The numbers above the annual plots represent the prior (top) and posterior (bottom) annual fluxes in units of Tg CO_2 yr^{-1}. Identical prior and posterior fluxes indicate no systematic bias in the inversion system, while any differences suggest a potential over- or underestimation of CO_2 sources or sinks.

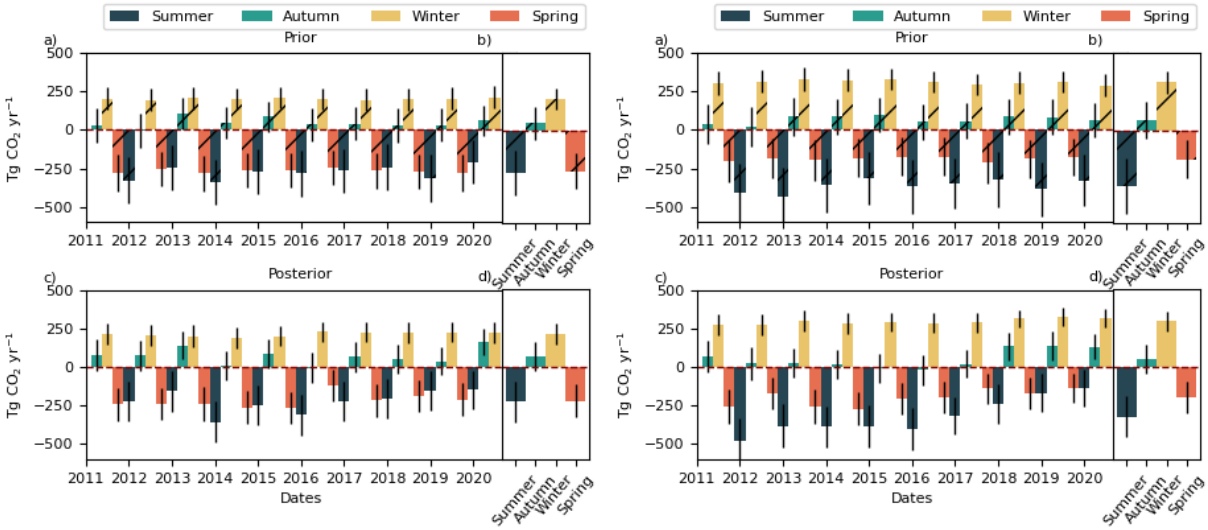

Figure S17. ~~S18~~ S17 Mean annual seasonal (summer – December to February, autumn – March to May, winter – June to August, spring – September to November) CO_2 prior (a) and posterior (c) net ~~air–land~~ land-to-air flux estimates for the North (left) and South Island (right) from the diurnal cycle test. Subplots b) and d) show the 2011-2020 average values for each season. The first and last season is removed from the plot and calculation due to insufficient number of months to calculate the seasonal average.

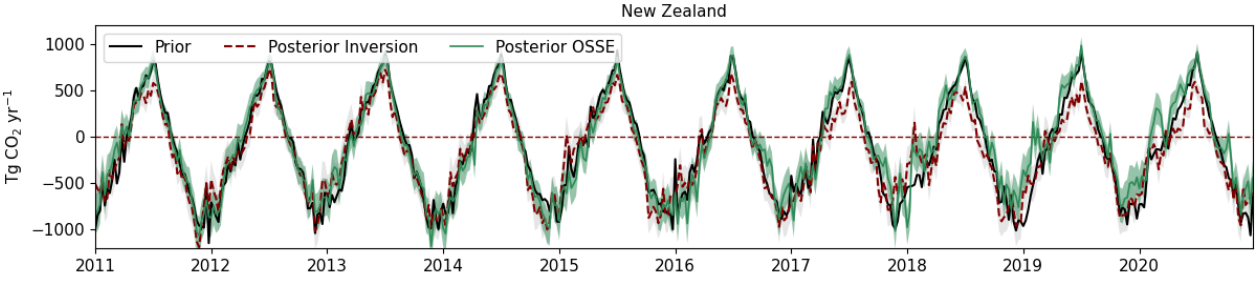

Figure S18. ~~S19~~ S18 ~~Timseries~~ Timeseries of the prior fluxes (black), diurnal cycle (green) and base inversion (red) posterior fluxes.

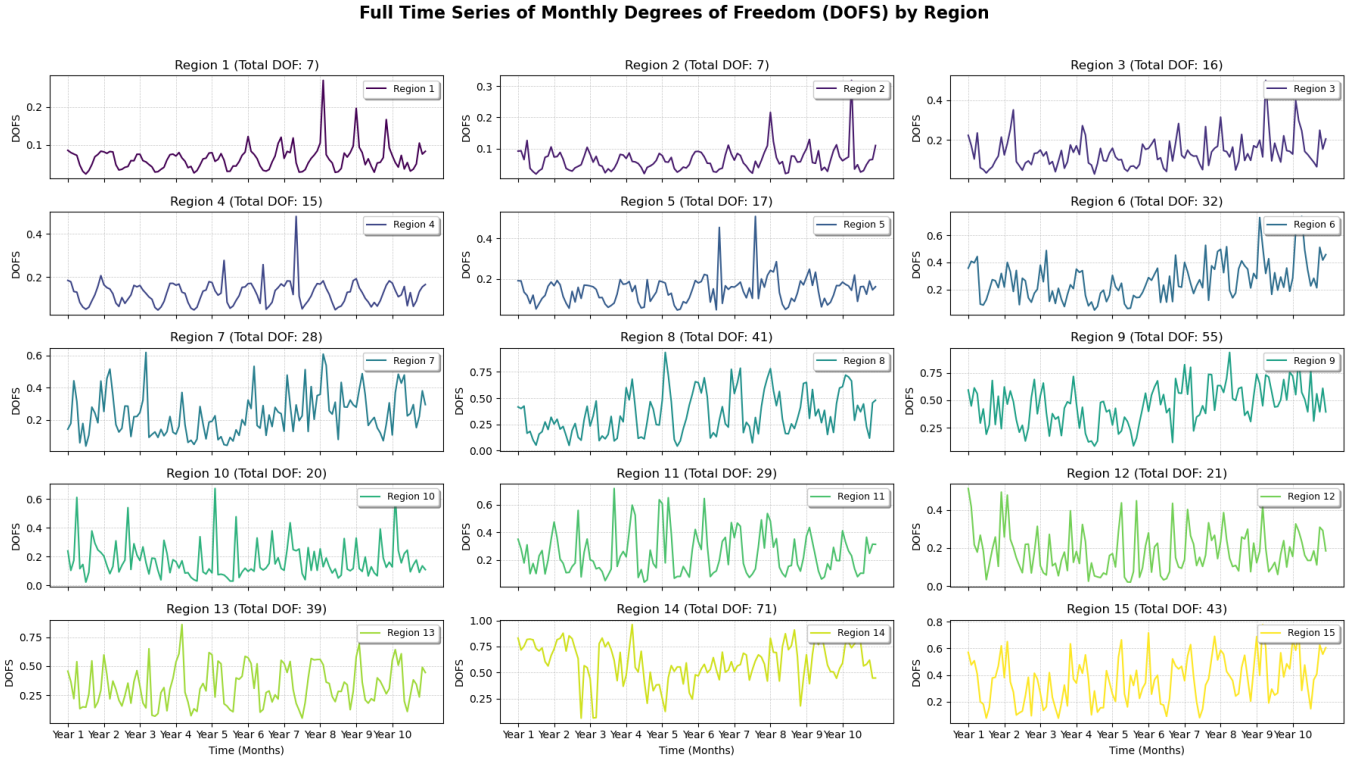

Figure S19. ~~S20~~ S19 Timeseries of Monthly mean Degrees of Freedom (DOFs) for each inversion region.

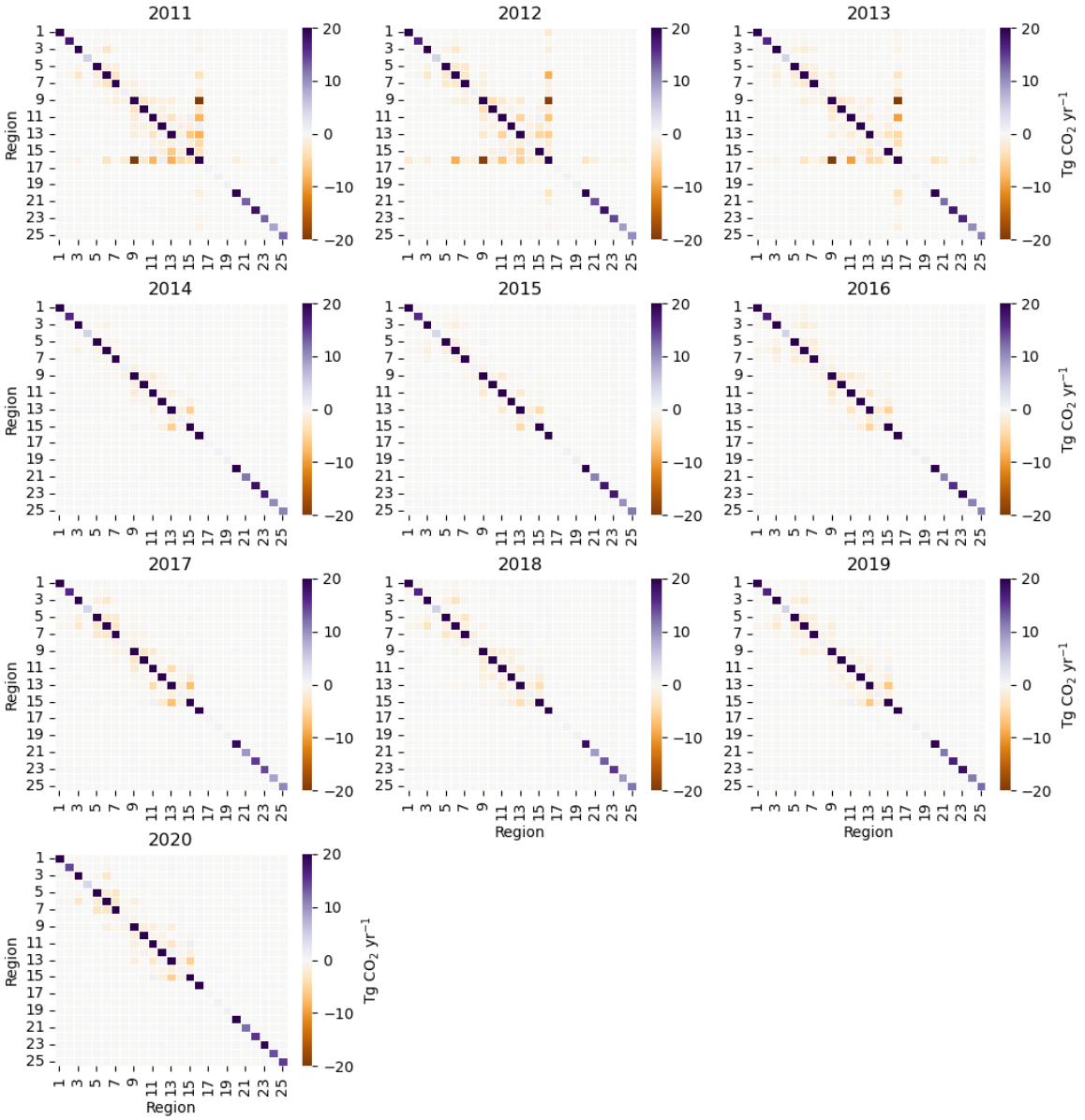

Figure S20. ~~S21~~ S20 Posterior annual covariance matrix for individual years in 2011-2020.

References

Berhe, A. A., Barnes, R. T., Six, J., and Marín-Spiotta, E.: Role of soil erosion in biogeochemical cycling of essential elements: carbon, nitrogen, and phosphorus, Annual Review of Earth and Planetary Sciences, 46, 521–548, 2018.

Bianchi, T. S., Arndt, S., Austin, W. E., Benn, D. I., Bertrand, S., Cui, X., Faust, J. C., Koziorowska-Makuch, K., Moy, C. M., Savage, C., et al.: Fjords as aquatic critical zones (ACZs), Earth-Science Reviews, 203, 103 145, 2020.

Brailsford, G. W., Stephens, B. B., Gomez, A. J., Riedel, K., Mikaloff Fletcher, S. E., Nichol, S. E., and Manning, M. R.: Long-term continuous atmospheric CO_2 measurements at Baring Head, New Zealand, Atmospheric Measurement Techniques, 5, 3109–3117, https://doi.org/10.5194/amt-5-3109-2012, 2012.

Bush, M., Allen, T., Bain, C., Boutle, I., Edwards, J., Finnenkoetter, A., Franklin, C., Hanley, K., Lean, H., Lock, A., Manners, J., Mittermaier, M., Morcrette, C., North, R., Petch, J., Short, C., Vosper, S., Walters, D., Webster, S., Weeks, M., Wilkinson, J., Wood, N., and Zerroukat, M.: The first Met Office Unified Model–JULES Regional Atmosphere and Land configuration, RAL1, Geoscientific Model Development, 13, 1999–2029, https://doi.org/10.5194/gmd-13-1999-2020, 2020.

CARS: CSIRO Atlas of Regional Seas, Salinity at standard depths, version: 2009.A.1.1, www.marine.csiro.au/atlas/, accessed on 19-07-2021, 2009.

Cleveland, R. B., Cleveland, W. S., McRae, J. E., and Terpenning, I.: STL: A seasonal-trend decomposition, Journal of Official Statistics, 6, 3–73, 1990.

Davies, T., Cullen, M. J., Malcolm, A. J., Mawson, M., Staniforth, A., White, A., and Wood, N.: A new dynamical core for the Met Office's global and regional modelling of the atmosphere, Quarterly Journal of the Royal Meteorological Society: A journal of the atmospheric sciences, applied meteorology and physical oceanography, 131, 1759–1782, 2005.

Dickson, A. G., Sabine, C. L., and Christian, J. R., eds.: Guide to Best Practices for Ocean CO_2 Measurements, PICES Special Publication 3, 191 pp, 2007.

Doherty, J.: Calibration and uncertainty analysis for complex environmental models, Watermark Numerical Computing Brisbane, Australia, 2015.

Dymond, J. R.: Soil erosion in New Zealand is a net sink of CO_2, Earth Surface Processes and Landforms, 35, 1763–1772, 2010.

Enting, I. G.: Inverse problems in atmospheric constituent transport, Cambridge University Press, 2002.

Gurney, K. R., Law, R. M., Denning, A. S., Rayner, P. J., Pak, B. C., Baker, D., Bousquet, P., Bruhwiler, L., Chen, Y.-H., Ciais, P., et al.: Transcom 3 inversion intercomparison: Model mean results for the estimation of seasonal carbon sources and sinks, Global Biogeochemical Cycles, 18, 2004.

Hall, B. D., Crotwell, A. M., Kitzis, D. R., Mefford, T., Miller, B. R., Schibig, M. F., and Tans, P. P.: Revision of the World Meteorological Organization Global Atmosphere Watch (WMO/GAW) CO_2 calibration scale, Atmospheric Measurement Techniques, 14, 3015–3032, https://doi.org/10.5194/amt-14-3015-2021, 2021.

Hall, G. M.: Mitigating an organization's future net carbon emissions by native forest restoration, Ecological Applications, 11, 1622–1633, 2001.

Hersbach, H., Bell, B., Berrisford, P., Biavati, G., Horányi, A., Muñoz Sabater, J., Nicolas, J., Peubey, C., Radu, R., Rozum, I., Schepers, D., Simmons, A., Soci, C., Dee, D., and Thépaut, J.-N.: ERA5 hourly data on single levels from 1979 to present, https://doi.org/10.24381/cds.adbb2d47, accessed on 14-07-2021, 2018.

Hersbach, H., Bell, B., Berrisford, P., Biavati, G., Horányi, A., Muñoz Sabater, J., Nicolas, J., Peubey, C., Radu, R., Rozum, I., Schepers, D., Simmons, A., Soci, C., Dee, D., and Thépaut, J.-N.: ERA5 monthly averaged data on single levels from 1979 to present, https://doi.org/10.24381/cds.f17050d7, accessed on 14-07-2021, 2019.

Hovius, N., Stark, C. P., and Allen, P. A.: Sediment flux from a mountain belt derived by landslide mapping, Geology, 25, 231–234, 1997.

Landcare Research: LCDB v5.0 - Land Cover Database version 5.0, Mainland, New Zealand (5.0) [dataset], https://doi.org/10.26060/W5B4-WK93, 2020.

Landschützer, P., Gruber, N., and Bakker, D. C. E.: Decadal variations and trends of the global ocean carbon sink, Global Biogeochemical Cycles, 30, 1396–1417, https://doi.org/https://doi.org/10.1002/2015GB005359, 2016.

Landschützer, P., Gruber, N., and Bakker, D. C. E.: An observation-based global monthly gridded sea surface pCO_2 product from 1982 onward and its monthly climatology (NCEI Accession 0160558). Version 5.5. NOAA National Centers for Environmental Information, https://doi.org/https://doi.org/10.7289/V5Z899N6, 2020a.

Landschützer, P., Laruelle, G. G., Roobaert, A., and Regnier, P.: A uniform pCO_2 climatology combining open and coastal oceans, Earth System Science Data, 12, 2537–2553, https://doi.org/10.5194/essd-12-2537-2020, 2020b.

Lauerwald, R., Allen, G. H., Deemer, B. R., Liu, S., Maavara, T., Raymond, P., Alcott, L., Bastviken, D., Hastie, A., Holgerson, M. A., et al.: Inland water greenhouse gas budgets for RECCAP2: 2. Regionalization and homogenization of estimates, Global Biogeochemical Cycles, 37, e2022GB007 658, 2023.

Livestock Improvement Corporation and Dairy NZ: New Zealand Dairy Statistics 2020-21, https://www.lic.co.nz/about/research-publications/dairy-statistics/, 2021.

Manderson, A., Hoogendoorn, C., and Newsome, P.: Grassland improvement mapping using Innovative Data Analysis (IDA) techniques, Manaaki Whenua – Landcare Research, Wellington, New Zealand Manaaki Whenua – Landcare Research Contract Report LC3373, 39, 2019.

Manning, A. J.: The challenge of estimating regional trace gas emissions from atmospheric observations, Philosophical Transactions of the Royal Society A: Mathematical, Physical and Engineering Sciences, 369, 1943–1954, 2011.

McGroddy, M., Baisden, W., and Hedin, L. O.: Stoichiometry of hydrological C, N, and P losses across climate and geology: An environmental matrix approach across New Zealand primary forests, Global Biogeochemical Cycles, 22, 2008.

MfE: LUCAS NZ Land Use Map (v008) [dataset], Ministry for the Environment, 2016.

MfE: Irrigated Land Area [dataset], https://data.mfe.govt.nz/layer/90838-irrigated-land-area-2017/, 2017.

Moore, T.: Dynamics of dissolved organic carbon in forested and disturbed catchments, Westland, New Zealand: 1. Maimai, Water Resources Research, 25, 1321–1330, 1989.

Nickless, A., Rayner, P. J., Engelbrecht, F., Brunke, E.-G., Erni, B., and Scholes, R. J.: Estimates of CO_2 fluxes over the city of Cape Town, South Africa, through Bayesian inverse modelling, Atmospheric Chemistry and Physics Discussions, 2017, 2017.

Ramirez, M. T., Allison, M. A., Bianchi, T. S., Cui, X., Savage, C., Schüller, S. E., Smith, R. W., and Vetter, L.: Modern deposition rates and patterns of organic carbon burial in Fiordland, New Zealand, Geophysical Research Letters, 43, 11–768, 2016.

Rosentreter, J. A., Laruelle, G. G., Bange, H. W., Bianchi, T. S., Busecke, J. J., Cai, W.-J., Eyre, B. D., Forbrich, I., Kwon, E. Y., Maavara, T., et al.: Coastal vegetation and estuaries are collectively a greenhouse gas sink, Nature climate change, pp. 1–9, 2023.

Scott, D. T., Baisden, W. T., Davies-Colley, R., Gomez, B., Hicks, D. M., Page, M. J., Preston, N. J., Trustrum, N. A., Tate, K. R., and Woods, R. A.: Localized erosion affects national carbon budget, Geophysical Research Letters, 33, 2006.

Silvester, W.: Ecological and economic significance of the non-legume symbioses, Proceedings of the 1st International Symposium on Nitrogen-fixation, pp. 489–507, 1976.

Smith, R. W., Bianchi, T. S., Allison, M., Savage, C., and Galy, V.: High rates of organic carbon burial in fjord sediments globally, Nature Geoscience, 8, 450–453, 2015.

Stallard, R. F.: Terrestrial sedimentation and the carbon cycle: Coupling weathering and erosion to carbon burial, Global biogeochemical cycles, 12, 231–257, 1998.

Steinkamp, K., Mikaloff Fletcher, S. E., Brailsford, G., Smale, D., Moore, S., Keller, E. D., Baisden, W. T., Mukai, H., and Stephens, B. B.: Atmospheric CO_2 observations and models suggest strong carbon uptake by forests in New Zealand., Atmospheric Chemistry and Physics, 17, 2017.

Stephens, B., Brailsford, G., Gomez, A., Riedel, K., Fletcher, S. M., Nichol, S., and Manning, M.: Analysis of a 39-year continuous atmospheric CO_2 record from Baring Head, New Zealand, Biogeosciences, 10, 2683, 2013.

Sweeney, C., Gloor, E., Jacobson, A. R., Key, R. M., McKinley, G., Sarmiento, J. L., and Wanninkhof, R.: Constraining global air-sea gas exchange for CO_2 with recent bomb 14C measurements, Global Biogeochemical Cycles, 21, https://doi.org/https://doi.org/10.1029/2006GB002784, 2007.

Tarantola, A.: Inverse problem theory and methods for model parameter estimation, SIAM, 2005.

Uglietti, C., Leuenberger, M. C., and Brunner, D.: European source and sink areas of CO_2 retrieved from Lagrangian transport model interpretation of combined O_2 and CO_2 measurements at the high alpine research station Jungfraujoch, Atmospheric Chemistry and Physics, 11, 8017–8036, 2011.

Villalobos, Y., Canadell, J. G., Keller, E. D., Briggs, P. R., Bukosa, B., Giltrap, D. L., Harman, I., Hilton, T. W., Kirschbaum, M. U. F., Lauerwald, R., Liang, L. L., Maavara, T., Mikaloff-Fletcher, S. E., Rayner, P. J., Resplandy, L., Rosentreter, J., Metz, E.-M., Serrano, O., and Smith, B.: A Comprehensive Assessment of Anthropogenic and Natural Sources and Sinks of Australasia's Carbon Budget, Global Biogeochemical Cycles, 37, e2023GB007 845, https://doi.org/https://doi.org/10.1029/2023GB007845, e2023GB007845 2023GB007845, 2023.

Walters, D., Boutle, I., Brooks, M., Melvin, T., Stratton, R., Vosper, S., Wells, H., Williams, K., Wood, N., Allen, T., Bushell, A., Copsey, D., Earnshaw, P., Edwards, J., Gross, M., Hardiman, S., Harris, C., Heming, J., Klingaman, N., Levine, R., Manners, J., Martin, G., Milton, S., Mittermaier, M., Morcrette, C., Riddick, T., Roberts, M., Sanchez, C., Selwood, P., Stirling, A., Smith, C., Suri, D., Tennant, W., Vidale, P. L., Wilkinson, J., Willett, M., Woolnough, S., and Xavier, P.: The Met Office Unified Model Global Atmosphere 6.0/6.1 and JULES Global Land 6.0/6.1 configurations, Geoscientific Model Development, 10, 1487–1520, https://doi.org/10.5194/gmd-10-1487-2017, 2017.

Wanninkhof, R.: Relationship between wind speed and gas exchange over the ocean, Journal of Geophysical Research: Oceans, 97, 7373–7382, 1992.

Weiss, R.: Carbon dioxide in water and seawater: the solubility of a non-ideal gas, Marine Chemistry, 2, 203–215, https://doi.org/https://doi.org/10.1016/0304-4203(74)90015-2, 1974.

Weiss, R. and Price, B.: Nitrous oxide solubility in water and seawater, Marine Chemistry, 8, 347–359, 1980.

Wood, N., Staniforth, A., White, A., Allen, T., Diamantakis, M., Gross, M., Melvin, T., Smith, C., Vosper, S., Zerroukat, M., and Thuburn, J.: An inherently mass-conserving semi-implicit semi-Lagrangian discretization of the deep-atmosphere global non-hydrostatic equations, Quarterly Journal of the Royal Meteorological Society, 140, 1505–1520, https://doi.org/https://doi.org/10.1002/qj.2235, 2014.